

1 SEARCH FOR PRODUCTION OF A HIGGS BOSON AND A SINGLE TOP
2 QUARK IN MULTILEPTON FINAL STATES IN pp COLLISIONS AT $\sqrt{s} = 13$
3 TeV.

4 by

5 Jose Andres Monroy MontaÑez

6 A DISSERTATION

7 Presented to the Faculty of

8 The Graduate College at the University of Nebraska

In Partial Fulfilment of Requirements

10 For the Degree of Doctor of Philosophy

11 Major: Physics and Astronomy

12 Under the Supervision of Kenneth Bloom and Aaron Dominguez

13 Lincoln, Nebraska

14 July, 2018

15 SEARCH FOR PRODUCTION OF A HIGGS BOSON AND A SINGLE TOP
16 QUARK IN MULTILEPTON FINAL STATES IN pp COLLISIONS AT $\sqrt{s} = 13$
17 TeV.

18 Jose Andres Monroy Montañez, Ph.D.

19 University of Nebraska, 2018

20 Adviser: Kenneth Bloom and Aaron Dominguez

²¹ Table of Contents

²² Table of Contents	iii
²³ List of Figures	vi
²⁴ List of Tables	viii
²⁵ 1 INTRODUCTION	1
²⁶ 2 Theoretical approach	2
27 2.1 Introduction	2
28 2.2 Standard model of particle physics	3
29 2.2.1 Fermions	5
30 2.2.1.1 Leptons	6
31 2.2.1.2 Quarks	8
32 2.2.2 Fundamental interactions	12
33 2.2.3 Gauge bosons	18
34 2.3 Electroweak unification and the Higgs mechanism	20
35 2.3.1 Spontaneous symmetry breaking (SSB)	28
36 2.3.2 Higgs mechanism	32
37 2.3.3 Masses of the gauge bosons	34

38	2.3.4	Masses of the fermions	35
39	2.3.5	The Higgs field	36
40	2.3.6	Production of Higgs bosons at LHC	37
41	2.3.7	Higgs boson decay channels	41
42	2.4	Associated production of a Higgs boson and a single Top quark.	42
43	2.5	The CP-mixing in tH processes	47
44	2.6	Experimantal status of the anomalous Higg-fermion coupling.	51
45	3	The CMS experiment at the LHC	53
46	3.1	Introduction	53
47	3.2	The LHC	54
48	3.3	The CMS experiment	63
49	3.3.1	Coordinate system	65
50	3.3.2	Pixels detector	67
51	3.3.3	Silicon strip tracker	69
52	3.3.4	Electromagnetic calorimeter	70
53	3.3.5	Hadronic calorimeter	72
54	3.3.6	Superconducting solenoid magnet	73
55	3.3.7	Muon system	75
56	3.3.8	CMS trigger system	76
57	3.3.9	CMS computing	78
58	4	Event generation, simulation and reconstruction	82
59	4.1	Event generation	83
60	4.2	underlying events and pileup	86
61	4.3	MC - MadEvent, MadGraph and madgraphNLO, powheg, pythia, tauola	86
62	4.4	detector simulation	86

63	4.5	event reconstruction- particle flow algorithm, vertexing , muon reco, electron reco, photon and hadron reco, jets reco, anti-kt algoritm, jet energy corrections, btagging, MET	87
64	4.6	MVA methods, NN, BDT, boosting, overtraining, variable ranking .	89
65	4.7	statistical inference, likelihood parametrization	89
66	4.8	nuisance paraeters	89
67	4.9	exclusion limits	89
68	4.10	asymptotic limits	89
70			
71	Bibliography		89
72	References		90

⁷³ List of Figures

74	2.1 Standard model of particle physics.	4
75	2.2 Transformations between quarks	12
76	2.3 Fundamental interactions in nature.	13
77	2.4 SM interactions diagrams	14
78	2.5 Neutral current processes	21
79	2.6 Spontaneous symmetry breaking mechanism	28
80	2.7 SSB Potential form	29
81	2.8 Potential for complex scalar field	30
82	2.9 SSB mechanism for complex scalar field	31
83	2.10 Proton-Proton collision	38
84	2.11 Higgs boson production mechanism Feynman diagrams	39
85	2.12 Higgs boson production cross section and decay branching ratios	40
86	2.13 Associated Higgs boson production mechanism Feynman diagrams	43
87	2.14 Cross section for tHq process as a function of κ_t	45
88	2.15 Cross section for tHW process as a function of κ_{Htt}	46
89	2.16 NLO cross section for tX_0 and $t\bar{t}X_0$	49
90	2.17 NLO cross section for tWX_0 , $t\bar{t}X_0$	50

91	2.18 Two dimentional κ_t - κ_V plot of the coupling modifiers. ATLAS and CMS 92 combination.	51
93	3.1 CERN accelerator complex	54
94	3.2 LHC protons source. First acceleration stage.	55
95	3.3 The LINAC2 accelerating system at CERN.	56
96	3.4 LHC layout and RF cavities module.	57
97	3.5 LHC dipole magnet.	59
98	3.6 Integrated luminosity delivered by LHC and recorded by CMS during 2016	61
99	3.7 LHC interaction points	62
100	3.8 Multiple pp collision bunch crossing at CMS.	64
101	3.9 Layout of the CMS detector	65
102	3.10 CMS detector coordinate system	66
103	3.11 CMS pixel detector schematic view.	68
104	3.12 SST Schematic view.	69
105	3.13 CMS ECAL schematic view	71
106	3.14 CMS HCAL schematic view	72
107	3.15 CMS solenoid magnet	74
108	3.16 CMS Muon system schematic view	75
109	3.17 CMS Level-1 trigger architecture	77
110	3.18 WLCG structure	78
111	3.19 Data flow from CMS detector through hardware Tiers	81

¹¹² List of Tables

113	2.1	Fermions of the SM.	5
114	2.2	Fermion masses.	6
115	2.3	Leptons properties.	9
116	2.4	Quarks properties.	9
117	2.5	Fermion weak isospin and weak hypercharge multiplets.	11
118	2.6	Fundamental interactions features.	15
119	2.7	SM gauge bosons.	19
120	2.8	Higgs boson properties.	37
121	2.9	Predicted branching ratios for a SM Higgs boson with $m_H = 125 \text{ GeV}/c^2$	42
122	2.10	Predicted SM cross sections for tH production at $\sqrt{s} = 13 \text{ TeV}$	44
123	2.11	Predicted enhancement of the tHq and tHW cross sections at LHC	47

¹²⁴ Chapter 1

¹²⁵ INTRODUCTION

¹²⁶ **Chapter 2**

¹²⁷ **Theoretical approach**

¹²⁸ **2.1 Introduction**

¹²⁹ The physical description of the universe is a challenge that physicists have faced by
¹³⁰ making theories that refine existing principles and proposing new ones in an attempt
¹³¹ to embrace emerging facts and phenomena.

¹³²

¹³³ At the end of 1940s Julian Schwinger [1] and Richard P. Feynman [2], based in the
¹³⁴ work of Sin-Itiro Tomonaga [3], developed an electromagnetic theory consistent with
¹³⁵ special relativity and quantum mechanics that describes how matter and light inter-
¹³⁶ act; the so-called “quantum eletrodynamics” (QED) had born.

¹³⁷

¹³⁸ QED has become the guide in the development of theories that describe the universe.
¹³⁹ It was the first example of a quantum field theory (QFT), which is the theoretical
¹⁴⁰ framework for building quantum mechanical models that describes particles and their
¹⁴¹ interactions. QFT is composed of a set of mathematical tools that combines classical
¹⁴² fields, special relativity and quantum mechanics, while keeping the quantum point

143 particles and locality ideas.

144 This chapter gives an overview of the standard model of particle physics, starting
 145 with a description of the particles and interactions that compose it, followed by a
 146 description of the electroweak interaction, the Higgs boson and the associated pro-
 147 duction of Higgs boson and a single top quark (tH). The description contained in
 148 this chapter is based on references [4–6].

149 2.2 Standard model of particle physics

150 Particle physics at the fundamental level is modeled in terms of a collection of in-
 151 teracting particles and fields in a theory known as the “standard model of particle
 152 physics (SM)”¹.

153

154 The full picture of the SM is composed of three fields², whose excitations are inter-
 155 preted as particles called mediators or force-carriers; a set of fields, whose excitations
 156 are interpreted as elementary particles, interacting through the exchange of those
 157 mediators and a field that gives the mass to elementary particles. Figure 2.1 shows
 158 an scheme of the SM particles organization. In addition to the particles in the scheme
 159 (but not listed in it), their corresponding anti-particles, with opposite quantum num-
 160 bers, are also part of the picture; some particles are their own anti-particles, like
 161 photon or Higgs, or anti-particle is already listed like in the W^+ and W^- case.

162

163 The mathematical formulation of the SM is based on group theory and the use of
 164 Noether’s theorem [8] which states that for a physical system modeled by a Lagrangian

¹ The formal and complete treatment of the SM is out of the scope of this document, however a plenty of textbooks describing it at several levels are available in the literature. The treatment in references [?] is quite comprehensive and detailed.

² Note that gravitational field is not included in the standard model formulation

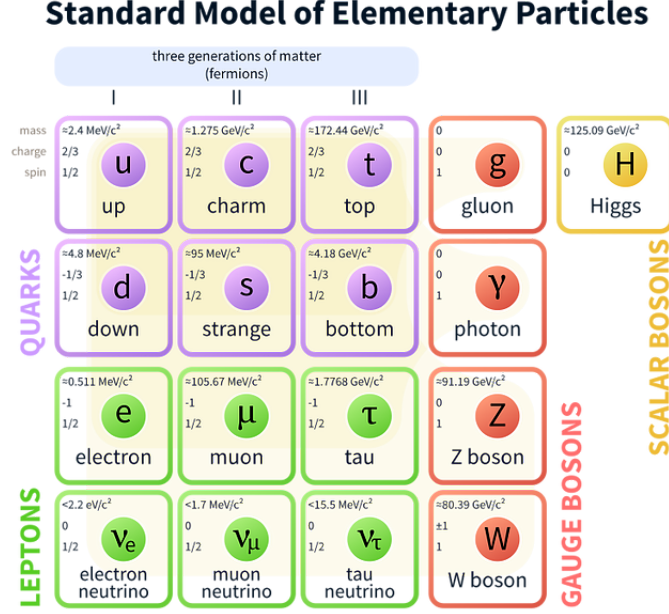


Figure 2.1: Schematic representation of the Standard model of particle physics. SM is a theoretical model intended to describe three of the four fundamental forces of the universe in terms of a set of particles and their interactions. [7].

165 that is invariant under a group of transformations a conservation law is expected. For
 166 instance, a system described by a time-independent Lagrangian is invariant (symmet-
 167 ric) under time changes (transformations) with the total energy conservation law as
 168 the expected conservation law. In QED, the charge operator (Q) is the generator of
 169 the $U(1)$ symmetry which according to the Noether's theorem means that there is a
 170 conserved quantity; this conserved quantity is the electric charge and thus the law
 171 conservation of electric charge is established.

172
 173 In the SM, the symmetry group $SU(3)_C \otimes SU(2)_L \otimes U(1)_Y$ describes three of the
 174 four fundamental interactions in nature(see section 2.2.2): strong interaction(SI),
 175 weak interaction(WI) and electromagnetic interactions (EI) in terms of symmetries
 176 associated to physical quantities:

- 177 • Strong: $SU(3)_C$ associated to color charge
- 178 • Weak: $SU(2)_L$ associated to weak isospin and chirality
- 179 • Electromagnetic: $U(1)_Y$ associated to weak hypercharge and electric charge
- 180 It will be shown that the electromagnetic and weak interactions are combined in
 181 the so-called electroweak interaction where chirality, hypercharge, weak isospin and
 182 electric charge are the central concepts.

183 **2.2.1 Fermions**

184 The basic constituents of the ordinary matter at the lowest level, which form the set
 185 of elementary particles in the SM formulation, are quarks and leptons. All of them
 186 have spin 1/2, therefore they are classified as fermions since they obey Fermi-Dirac
 187 statistics. There are six “flavors” of quarks and three of leptons organized in three
 188 generations, or families, as shown in table 2.1.

189

		Generation		
		1st	2nd	3rd
Leptons	Charged	Electron (e)	Moun(μ)	Tau (τ)
	Neutral	Electron neutrino (ν_e)	Muon neutrino (ν_μ)	Tau neutrino (ν_τ)
Quarks	Up-type	Up (u)	Charm (c)	Top (t)
	Down-type	Down (d)	Strange (s)	Bottom (b)

Table 2.1: Fermions of the SM. There are six flavors of quarks and three of leptons, organized in three generations, or families, composed of two pairs of closely related particles. The close relationship is motivated by the fact that WI between leptons is limited to the members of the same generation; WI between quarks is not limited but greatly favoured, to same generation members.

190

191 There is a mass hierarchy between generations (see table 2.2), where the higher gener-
 192 ation particles decays to the lower one, which can explain why the ordinary matter is

193 made of particles in the first generation. In the SM, neutrinos are modeled as massless
 194 particles so they are not subject to this mass hierarchy; however, today it is known
 195 that neutrinos are massive so the hierarchy could be restated. The reason behind this
 196 mass hierarchy is one of the most important open questions in particle physics, and
 197 it becomes more puzzling when noticing that the mass difference between first and
 198 second generation fermions is small compared to the mass difference with respect to
 199 the third generation.

Lepton	Mass (MeV/c ²)	Quark	Mass (MeV/c ²)
e	0.51	u	2.2
μ	105.65	c	1.28×10^3
τ	1776.86	t	173.1×10^3
ν_e	Unknown	d	4.7
ν_μ	Unknown	s	96
τ_μ	Unknown	b	4.18×10^3

Table 2.2: Fermion masses [9]. Generations differ by mass in a way that have been interpreted as a masss hierarchy. Approximate values with no uncertainties are used, for comparison purpose.

200

201 Usually, the second and third generation fermions are produced in high energy pro-
 202 cesses, like the ones recreated in particle accelerators.

203 2.2.1.1 Leptons

204 A lepton is an elementary particle that is not subject to the SI. As seen in table 2.1,
 205 there are two types of leptons, the charged ones (electron, muon and tau) and the
 206 neutral ones (the three neutrinos). The electric charge (Q) is the property that gives
 207 leptons the ability to participate in the EI. From the classical point of view, Q plays
 208 a central role determining, among others, the strength of the electric field through
 209 which the electromagnetic force is exerted. It is clear that neutrinos are not affected

210 by EI because they don't carry electric charge.

211

212 Another feature of the leptons that is fundamental in the mathematical description
213 of the SM is the chirality, which is closely related to spin and helicity. Helicity defines
214 the handedness of a particle by relating its spin and momentum such that if they
215 are parallel then the particle is right-handed; if spin and momentum are antiparallel
216 the particle is said to be left-handed. The study of parity conservation (or viola-
217 tion) in β -decay has shown that only left-handed electrons/neutrinos or right-handed
218 positrons/anti-neutrinos are created [10]; the inclusion of that feature in the theory
219 was achieved by using projection operators for helicity, however, helicity is frame de-
220 pendent for massive particles which makes it not Lorentz invariant and then another
221 related attribute has to be used: *chirality*.

222

223 Chirality is a purely quantum attribute which makes it not so easy to describe in
224 graphical terms but it defines how the wave function of a particle transforms under
225 certain rotations. As with helicity, there are two chiral states, left-handed chiral (L)
226 and right-handed chiral (R). In the highly relativistic limit where $E \approx p \gg m$ helicity
227 and chirality converge, becoming exactly the same for massless particles.

228

229 In the following, when referring to left-handed (right-handed) it will mean left-handed
230 chiral (right-handed chiral). The fundamental fact about chirality is that while EI
231 and SI are not sensitive to chirality, in WI left-handed and right-handed fermions are
232 treated asymmetrically, such that only left handed fermions and right-handed anti-
233 fermions are allowed to couple to WI mediators, which is a violation of parity. The
234 way to translate this statement in a formal mathematical formulation is based on the
235 isospin symmetry group $SU(2)_L$.

236

237 Each generation of leptons is seen as a weak isospin doublet.³ The left-handed charged
 238 lepton and its associated left-handed neutrino are arranged in doublets of weak isospin
 239 T=1/2 while their right-handed partners are singlets:

$$\begin{pmatrix} \nu_l \\ l \end{pmatrix}_L, l_R := \begin{pmatrix} \nu_e \\ e \end{pmatrix}_L, \begin{pmatrix} \nu_\mu \\ \mu \end{pmatrix}_L, \begin{pmatrix} \nu_\tau \\ \tau \end{pmatrix}_L, e_R, \mu_R, \tau_R, \nu_{eR}, \nu_{\mu R}, \nu_{\tau R} \quad (2.1)$$

240 The isospin third component refers to the eigenvalues of the weak isospin operator
 241 which for doublets is $T_3 = \pm 1/2$, while for singlets it is $T_3 = 0$. The physical meaning
 242 of this doublet-singlet arrangement falls in that the WI couples the two particles in
 243 the doublet by exchanging the interaction mediator while the singlet member is not
 244 involved in WI. The main properties of the leptons are summarized in table 2.3.

245

246 Altough all three flavor neutrinos have been observed, their masses remain unknown
 247 and only some estimations have been made [11]. The main reason is that the fla-
 248 vor eigenstates are not the same as the mass eigenstates which implies that when
 249 a neutrino is created its mass state is a linear combination of the three mass eigen-
 250 states and experiments can only probe the squared difference of the masses. The
 251 Pontecorvo-Maki-Nakagawa-Sakata (PMNS) mixing matrix encode the relationship
 252 between flavor and mass eigenstates.

253

254 2.2.1.2 Quarks

255 Quarks are the basic constituents of protons and neutrons. The way quarks join to
 256 form bound states, called “hadrons”, is through the SI. Quarks are affected by all the

³ The weak isospin is an analogy of the isospin symmetry in strong interaction where neutron and proton are affected equally by strong force but differ in their charge.

Lepton	Q(e)	T_3	L_e	L_μ	L_τ	Lifetime (s)
Electron (e)	-1	-1/2	1	0	0	Stable
Electron neutrino(ν_e)	0	1/2	1	0	0	Unknown
Muon (μ)	-1	-1/2	0	1	0	2.19×10^{-6}
Muon neutrino (ν_μ)	0	1/2	0	1	0	Unknown
Tau (τ)	-1	-1/2	0	0	1	290.3×10^{-15}
Tau neutrino (τ_μ)	0	1/2	0	0	1	Unknown

Table 2.3: Leptons properties [9]. Q: electric charge, T_3 : weak isospin. Only left-handed leptons and right-handed anti-leptons participate in the WI. Anti-particles with inverted T_3 , Q and lepton number complete the leptons set but are not listed. Right-handed leptons and left-handed anti-leptons, neither listed, form weak isospin singlets with $T_3 = 0$ and do not take part in the weak interaction.

257 fundamental interactions which means that they carry all the four types of charges:
258 color, electric charge, weak isospin and mass.

Flavor	Q(e)	I_3	T_3	B	C	S	T	B'	Y	Color
Up (u)	2/3	1/2	1/2	1/3	0	0	0	0	1/3	r,b,g
Charm (c)	2/3	0	1/2	1/3	1	0	0	0	4/3	r,b,g
Top(t)	2/3	0	1/2	1/3	0	0	1	0	4/3	r,b,g
Down(d)	-1/3	-1/2	-1/2	1/3	0	0	0	0	1/3	r,b,g
Strange(s)	-1/3	0	-1/2	1/3	0	-1	0	0	-2/3	r,b,g
Bottom(b)	-1/3	0	-1/2	1/3	0	0	0	-1	-2/3	r,b,g

Table 2.4: Quarks properties [9]. Q: electric charge, I_3 : isospin, T_3 : weak isospin, B: baryon number, C: charmness, S: strangeness, T: topness, B' : bottomness, Y: hypercharge. Anti-quarks posses the same mass and spin as quarks but all charges (color, flavor numbers) have opposite sign.

259

260 Table 2.4 summarizes the features of quarks, among which the most particular is
261 their fractional electric charge. Note that fractional charge is not a problem, given
262 that quarks are not found isolated, but serves to explain how composed particles are
263 formed out of two or more valence quarks⁴.

264

⁴ Hadrons can contain an indefinite number of virtual quarks and gluons, known as the quark and gluon sea, but only the valence quarks determine hadrons' quantum numbers.

265 Color charge is the responsible for the SI between quarks and is the symmetry
 266 ($SU(3)_C$) that defines the formalism to describe SI. There are three colors: red (r),
 267 blue(b) and green(g) and their corresponding three anti-colors; thus each quark carries
 268 one color unit while anti-quarks carries one anti-color unit. As said above, quarks are
 269 not allowed to be isolated due to the color confinement effect, therefore their features
 270 have been studied indirectly by observing their bound states created when:

- 271 • one quark with a color charge is attracted by an anti-quark with the correspond-
 272 ing anti-color charge forming a colorless particle called a “meson.”
- 273 • three quarks (anti-quarks) with different color (anti-color) charges are attracted
 274 among them forming a colorless particle called a “baryon(anti-baryon).”

275 In the first version of the quark model (1964), M. Gell-Mann [12] and G. Zweig
 276 [13, 14] developed a consistent way to classify hadrons according to their properties.
 277 Only three quarks (u, d, s) were involved in a scheme in which all baryons have
 278 baryon number $B=1$ and therefore quarks have $B=1/3$; non-baryons have $B=0$. The
 279 scheme organizes baryons in a two-dimensional space ($I_3 - Y$); Y (hypercharge) and I_3
 280 (isospin) are quantum numbers related by the Gell-Mann-Nishijima formula [15, 16]:

$$Q = I_3 + \frac{Y}{2} \quad (2.2)$$

281 where $Y = B + S + C + T + B'$ are the quantum numbers listed in table 2.4. Baryon
 282 number is conserved in SI and EI which means that single quarks cannot be created
 283 but in pairs $q - \bar{q}$.

284

285 There are six quark flavors organized in three generations (see table 2.1) following a
 286 mass hierarchy which, again, implies that higher generations decay to first generation

287 quarks.

	Quarks			T_3	Y_W	Leptons			T_3	Y_W
Doublets	$(\frac{u}{d'})_L$	$(\frac{c}{s'})_L$	$(\frac{t}{b'})_L$	$(\frac{1/2}{-1/2})$	1/3	$(\nu_e)_L$	$(\nu_\mu)_L$	$(\nu_\tau)_L$	$(\frac{1/2}{-1/2})$	-1
Singlets	u_R	c_R	t_R	0	4/3	ν_{eR}	$\nu_{\mu R}$	$\nu_{\tau R}$	0	-2

Table 2.5: Fermion weak isospin and weak hypercharge multiplets. Weak hypercharge is calculated through the Gell-Mann-Nishijima formula 2.2 but using the weak isospin and charge for quarks.

288

289 Isospin doublets of quarks are also defined (see table 2.5) and as for neutrinos, the
 290 mass eigenstates are not the same as the WI eigenstates which means that members of
 291 different quark generations are connected by the WI mediator; thus, up-type quarks
 292 are coupled not to down-type quarks directly but to a superposition of down-type
 293 quarks (q'_d) via WI according to:

$$q'_d = V_{CKM} q_d$$

294

$$\begin{pmatrix} d' \\ s' \\ b' \end{pmatrix} = \begin{pmatrix} V_{ud} & V_{us} & V_{ub} \\ V_{cd} & V_{cs} & V_{cb} \\ V_{td} & V_{ts} & V_{tb} \end{pmatrix} \begin{pmatrix} d \\ s \\ b \end{pmatrix} \quad (2.3)$$

295 where V_{CKM} is known as Cabibbo-Kobayashi-Maskawa (CKM) mixing matrix [17,18].
 296 The weak decays of quarks are represented in the diagram of figure 2.2; again the
 297 CKM matrix plays a central role since it contains the probabilities for the different
 298 quark decay channels, in particular, note that quark decays are greatly favored be-
 299 tween generation members.

300

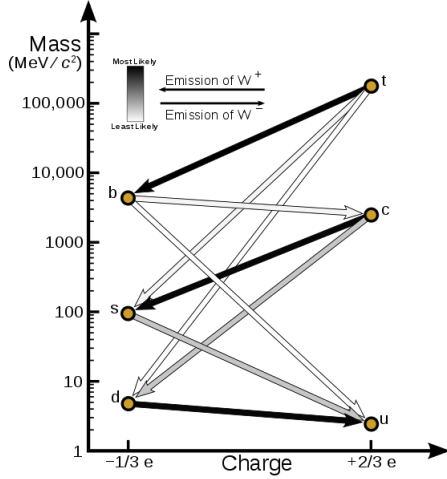


Figure 2.2: Transformations between quarks through the exchange of a WI. Higher generations quarks decay to first generation quarks by emitting a W boson. The arrow color indicates the likelihood of the transition according to the grey scale in the top left side which represent the CKM matrix parameters [19].

301 CKM matrix is a 3×3 unitary matrix parametrized by three mixing angles and
 302 the *CP-mixing phase*; the latter is the parameter responsible for the Charge-Parity
 303 symmetry violation (CP-violation) in the SM. The fact that the b quark decays almost
 304 all the times to a top quark is exploited in this thesis when making the selection of
 305 the signal events by requiring the presence of a jet tagged as a jet coming from a
 306 b quark in the final state. The effect of the *CP-mixing phase* on the cross section of
 307 associated production of Higgs boson and a single top process is also explored in this
 308 thesis.

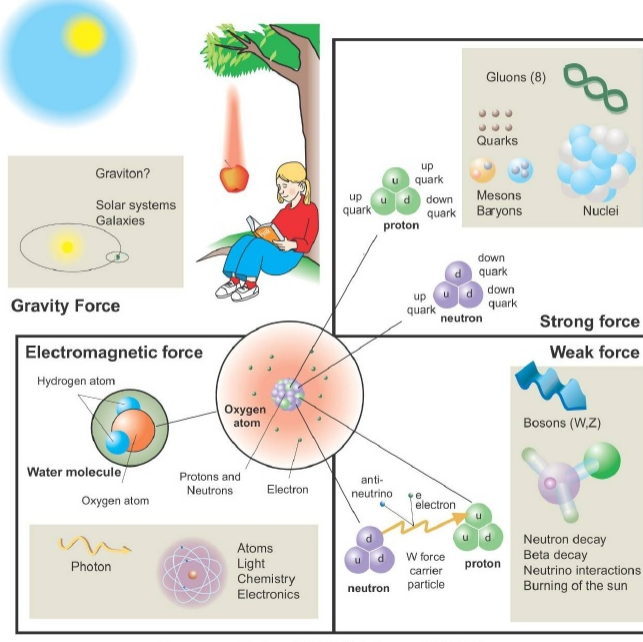
309 **2.2.2 Fundamental interactions**

310 Even though there are many manifestations of force in nature, like the ones repre-
 311 sented in figure 2.3, we can classify all of them into one of four fundamental interac-
 312 tions:

- 313 • *Electromagnetic interaction (EI)* affects particles that are “electrically charged,”

Fundamental interactions.

Illustration: Typoform



Summer School KPI 15 August 2009

Figure 2.3: Fundamental interactions in nature. Despite the many manifestations of forces in nature, we can track all of them back to one of the fundamental interactions. The most common forces are gravity and electromagnetic given that all of us are subject and experience them in everyday life.

314 like electrons and protons. It is described by QED combining quantum mechan-
 315 ics, special relativity and electromagnetism in order to explain how particles
 316 with electric charge interact through the exchange of photons, therefore, one
 317 says that “Electromagnetic Force” is mediated by “photons”. Figure 2.4a. shows
 318 a graphical representation, known as “feynman diagram”, of electron-electron
 319 scattering.

- 320 • *Strong interaction (SI)* described by Quantum Chromodynamics (QCD). Hadrons
 321 like proton and neutron have internal structure given that they are composed
 322 of two or more valence quarks⁵. Quarks have fractional electric charge which
 323 means that they are subject to electromagnetic interaction and in the case of the

⁵ particles made of four and five quarks are exotic states not so common.

324 proton they should break apart due to electrostatic repulsion; however, quarks
 325 are held together inside the hadrons against their electrostatic repulsion by the
 326 “Strong Force” through the exchange of “gluons.” The analog to the electric
 327 charge is the “color charge”. Electrons and photons are elementary particles
 328 as quarks but they don’t carry color charge, therefore they are not subject to
 329 SI. The feynman diagram for gluon exchange between quarks is shown in figure
 330 2.4b.

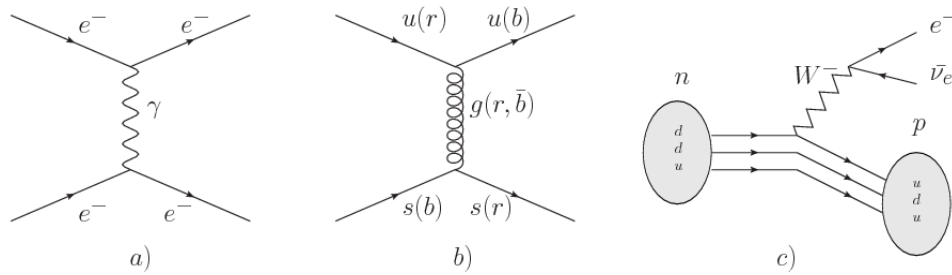


Figure 2.4: Feynman diagrams representing the interactions in SM; a) EI: e - e scattering; b) SI: gluon exchange between quarks ; c) WI: β -decay

331 • *Weak interaction (WI)* described by the weak theory (WT), is responsible, for
 332 instance, for the radioactive decay in atoms and proton-proton (pp) fusion
 333 within the sun. Quarks and leptons are the particles affected by the weak
 334 interaction; they possess a property called “flavor charge” (see 2.2.1) which can
 335 be changed by emitting or absorbing one weak force mediator. There are three
 336 mediators of the “weak force” known as “Z” boson in the case of electrically
 337 neutral changes and “ W^\pm ” bosons in the case of electrically charged changes.
 338 The “weak isospin” is the WI analog to electric charge in EI, and color charge
 339 in SI, and defines how quarks and leptons are affected by the weak force. Figure
 340 2.4c. shows the feynman diagram of β -decay where a newtron (n) is transformed
 341 in a proton (p) by emmiting a W^- particle. Since this thesis is in the frame
 342 of the electroweak interaction, a more detailed description of it will be given in

343 section 2.3

- 344 • *Gravitational interaction (GI)* described by General Theory of Relativity (GR).
 345 It is responsible for the structure of galaxies and black holes as well as the
 346 expansion of the universe. As a classical theory, in the sense that it can be for-
 347 mulated without even appeal to the concept of quantization, it implies that the
 348 spacetime is a continuum and predictions can be made without limitation to the
 349 precision of the measurement tools. The latter represent a direct contradic-
 350 tion of the quantum mechanics principles. Gravity is deterministic while quantum
 351 mechanics is probabilistic; despite that, efforts to develop a quantum theory of
 352 gravity have predicted the “graviton” as mediator of the Gravitational force⁶.

Interaction	Acts on	Relative strength	Range (m)	Mediators
Electromagnetic (QED)	Electrically charged particles	10^{-2}	Infinite	Photon
Strong (QCD)	Quarks and gluons	1	10^{-15}	Gluon
Weak (WI)	Leptons and quarks	10^{-6}	10^{-18}	W^\pm, Z
Gravitational (GI)	Massive particles	10^{-39}	Infinite	Graviton

Table 2.6: Fundamental interactions features [20].

353

354 Table 2.6 summarizes the main features of the fundamental interactions. The rela-
 355 tive strength of the fundamental forces reveals the meaning of strong and weak; in
 356 a context where the relative strength of the SI is 1, the EI is about hundred times
 357 weaker and WI is about million times weaker than the SI. A good description on
 358 how the relative strength and range of the fundamental interactions are calculated
 359 can be found in references [20, 21]. In the everyday life, only EI and GI are explicitly
 360 experienced due to the range of these interactions; i.e., at the human scale distances

⁶ Actually a wide variety of theories have been developed in an attempt to describe gravity; some famous examples are string theory and supergravity.

361 only EI and GI have appreciable effects, in contrast to SI which at distances greater
 362 than 10^{-15} m become negligible.

363

364 QED was built successfully on the basis of the classical electrodynamics theory (CED)
 365 of Maxwell and Lorentz, following theoretical and experimental requirements imposed
 366 by

- 367 • lorentz invariance: independence on the reference frame.
- 368 • locallity: interacting fields are evaluated at the same space-time point to avoid
 369 action at a distance.
- 370 • renormalizability: physical predictions are finite and well defined
- 371 • particle spectrum, symmetries and conservation laws already known must emerge
 372 from the theory.
- 373 • gauge invariance.

374 The gauge invariance requirement reflects the fact that the fundamental fields cannot
 375 be directly measured but associated fields which are the observables. Electric (“**E**”)
 376 and magnetic (“**B**”) fields in CED are associated with the electric scalar potential
 377 “**V**” and the vector potential “**A**”. In particular, **E** can be obtained by measuring
 378 the change in the space of the scalar potential (ΔV); however, two scalar potentials
 379 differing by a constant “f” correspond to the same electric field. The same happens in
 380 the case of the vector potential “**A**”; thus, different configurations of the associated
 381 fields result in the same set of values of the observables. The freedom in choosing
 382 one particular configuration is known as “gauge freedom”; the transformation law con-
 383 necting two configurations is known as “gauge transformation” and the fact that the

384 observables are not affected by a gauge transformation is called “gauge invariance”.

385

386 When the gauge transformation:

$$\begin{aligned} \mathbf{A} &\rightarrow \mathbf{A} - \Delta f \\ V &\rightarrow V - \frac{\partial f}{\partial t} \end{aligned} \tag{2.4}$$

387 is applied to Maxwell equations, they are still satisfied and the fields remain invariant.

388 Thus, CED is invariant under gauge transformations and is called a “gauge theory”.

389 The set of all gauge transformations form the “symmetry group” of the theory, which

390 according to the group theory, has a set of “group generators”. The number of group

391 generators determine the number of “gauge fields” of the theory.

392

393 As mentioned in the first lines of section 2.2, QED has one symmetry group ($U(1)$)

394 with one group generator (the Q operator) and one gauge field (the electromagnetic

395 field A^μ). In CED there is not a clear definition, beyond the historical convention, of

396 which fields are the fundamental and which are the associated, but in QED it is clear

397 that the fundamental field is A^μ . When a gauge theory is quantized, the gauge field

398 is quantized and its quanta is called “gauge boson”. The word boson characterizes

399 particles with integer spin which obvey Bose-einstein statistics.

400

401 As will be detailed in section 2.3, interactions between particles in a system can be

402 obtained by considering first the Lagrangian density of free particles in the system,

403 which of course is incomplete because the interaction terms have been left out, and

404 demanding global phase transformation invariance. Global phase transformation in-

405 variance means that a gauge transformation is performed identically to every point
 406 in the space⁷ and the Lagrangian remains invariant. Then, the global transformation
 407 is promoted to a local phase transformation (this time the gauge transformation de-
 408 pends on the position in space) and again invariance is required.

409

410 Due to the space dependence of the local tranformation, the Lagrangian density is
 411 not invariant anymore. In order to restate the gauge invariance, the gauge covariant
 412 derivative is introduced in the Lagrangian and with it the gauge field responsible for
 413 the interaction between particles in the system. The new Lagrangian density is gauge
 414 invariant, includes the interaction terms needed to account for the interactions and
 415 provides a way to explain the interaction between particles through the exchange of
 416 the gauge boson.

417 This recipe was used to build QED and the theories that aim to explain the funda-
 418 mental interactions.

419 **2.2.3 Gauge bosons**

420 The importance of the gauge bosons comes from the fact that they are the force
 421 mediators or force carriers. The features of the gauge bosons reflect those of the
 422 fields they represent and they are extracted from the Lagrangian density used to
 423 describe the interactions. In section 2.3, it will be shown how the gauge bosons of the
 424 EI and WI emerge from the electroweak Lagrangian. The SI gauge bosons features
 425 are also extracted from the SI Lagrangian but it is not detailed in this document. The
 426 main features of the SM gauge bosons will be briefly presented below and summarized
 427 in table 2.7.

⁷ Here space corresponds to the 4-dimensional space i.e. space-time.

- 428 • **Photon.** EI occurs when the photon couples to (is exchanged between) particles
 429 carrying electric charge; however, the photon itself does not carry electric charge,
 430 therefore, there is no coupling between photons. Given that the photon is
 431 massless the EI is of infinite range, i.e., electrically charged particles interact
 432 even if they are located far away one from each other; this also implies that
 433 photons always move with the speed of light.
- 434 • **Gluon.** SI is mediated by gluons which, same as photons, are massless. They
 435 carry one unit of color charge and one unit of anticolor charge which means that
 436 gluons couple to other gluons. As a result, the range of the SI is not infinite
 437 but very short due to the attraction between gluons, giving rise to the “color
 438 confinement” which explains why color charged particles cannot be isolated but
 439 live within composited particles, like quarks inside protons.
- 440 • **W, Z.** The WI mediators, W^\pm and Z, are massive which explains their short-
 441 range. Given that the WI is the only interaction that can change the flavor
 442 of the interacting particles, the W boson is the responsible for the nuclear
 443 transmutation where a neutron is converted in a proton or vice versa with the
 444 involvement of an electron and a neutrino (see figure 2.4c). The Z boson is the
 445 responsible of the neutral weak processes like neutrino elastic scattering where
 446 no electric charge but momentum transference is involved. WI gauge bosons
 447 carry isospin charge which makes possible the interaction between them.

Interaction	Mediator	Electric charge (e)	Color charge	Weak Isospin	mass (GeV/c ²)
Electromagnetic	Photon (γ)	0	No	0	0
Strong	Gluon (g)	0	Yes -octet	No	0
Weak	W^\pm	± 1	No	± 1	80.385 ± 0.015
	Z	0	No	0	91.188 ± 0.002

Table 2.7: SM gauge bosons main features [9].

449 2.3 Electroweak unification and the Higgs

450 mechanism

451 Physicists dream of building a theory that contains all the interactions in one single
 452 interaction, i.e., showing that at some scale in energy all the four fundamental in-
 453 teractions are unified and only one interaction emerges in a “Theory of everything”.
 454 The first sign of the feasibility of such unification comes from success in the con-
 455 struction of the CED. Einstein spent years trying to reach that dream, which by
 456 1920 only involved electromagnetism and gravity, with no success; however, a new
 457 partial unification was achieved in the 1960’s, when S.Glashow [22], A.Salam [23] and
 458 S.Weinberg [24] independently proposed that electromagnetic and weak interactions
 459 are two manifestations of a more general interaction called “electroweak interaction
 460 (EWT)”. Both, QCD and EWT, were developed in parallel and following the useful
 461 prescription provided by QED and the gauge invariance principles.

462

463 The theory of weak interactions was capable of explaining the β -decay and in general
 464 the processes mediated by W^\pm bosons. However, there were some processes like the
 465 “ $\nu_\mu - e$ scattering” which would require the exchange of two W bosons (see figure 2.5
 466 top diagrams) giving rise to divergent loop integrals and then non finite predictions.
 467 By including neutral currents involving fermions via the exchange of neutral bosons
 468 Z, those divergences are compensated and the predictions become realistic.

469

470 Neutral weak interaction vertices conserve flavor in the same way as the electromag-
 471 netic vertices do, but additionally, the Z boson can couple to neutrinos which implies
 472 that processes involving charged fermions can proceed through EI or WI but processes
 473 involving neutrinos can proceed only through WI.

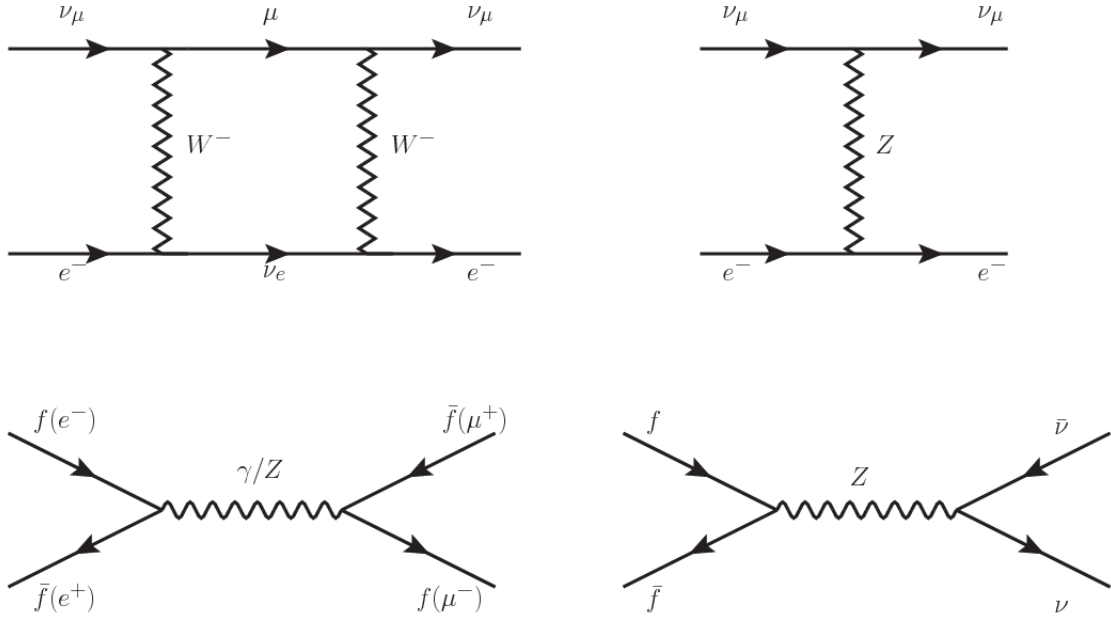


Figure 2.5: Top: $\nu_\mu - e^-$ scattering going through charged currents (left) and neutral currents (right). Bottom: neutral current processes for charged fermions (left) and involving neutrinos (right). While neutral current processes involving only charged fermions can proceed through EI or WI, those involving neutrinos can only proceed via WI.

474

475 The prescription to build a gauge theory of the WI consists of proposing a free field
476 Lagrangian density that includes the particles involved; next, by requesting invari-
477 ance under global phase transformations first and generalizing to local phase trans-
478 formations invariance later, the conserved currents are identified and interactions are
479 generated by introducing gauge fields. Given that the goal is to include the EI and
480 WI in a single theory, the group symmetry considered should be a combination of
481 $SU(2)_L$ and $U(1)_{em}$, however the latter cannot be used directly because the EI treats
482 left and right-handed particles indistinctly in contrast to the former. Fortunately, the
483 weak hypercharge, which is a combination of the weak isospin and the electric charge
484 (eqn 2.2) is suitable to be used since it is conserved by the EI and WI. Thus, the
485 symmetry group to be considered is

$$G \equiv SU(2)_L \otimes U(1)_Y \quad (2.5)$$

486 The following treatment applies to any of the fermion generations, but for simplicity
 487 the first generation of leptons will be considered [5, 6, 25, 26].

488

489 Given the first generation of leptons

$$\psi_1 = \begin{pmatrix} \nu_e \\ e^- \end{pmatrix}_L, \quad \psi_2 = \nu_{eR}, \quad \psi_3 = e_R^- \quad (2.6)$$

490 the charged fermionic currents are given by

$$J_\mu \equiv J_\mu^+ = \bar{\nu}_{eL} \gamma_\mu e_L, \quad J_\mu^\dagger \equiv J_\mu^- = \bar{e}_L \gamma_\mu \nu_{eL} \quad (2.7)$$

491 and the free Lagrangian is given by

$$\mathcal{L}_0 = \sum_{j=1}^3 i\bar{\psi}_j(x) \gamma^\mu \partial_\mu \psi_j(x). \quad (2.8)$$

492 Mass terms are included directly in the QED and QCD free Lagrangians since they
 493 preserve the invariance under the symmetry transformations involved which treat
 494 left-handed and right-handed similarly, however mass terms of the form

$$m_W^2 W_\mu^\dagger(x) W^\mu(x) + \frac{1}{2} m_Z^2 Z_\mu(x) Z^\mu(x) - m_e \bar{\psi}_e(x) \psi_e(x) \quad (2.9)$$

495 which represent the mass of W^\pm , Z and electrons, are not invariant under G trans-
 496 formations, therefore the gauge fields described by the EWI are in principle massless.

497

498 Experiments have shown that the gauge fields are not massless; however, they have

499 to acquire mass through a mechanism compatible with the gauge invariance; that
 500 mechanism is known as the “Higgs mechanism” and will be considered later in this
 501 section. The global transformations in the combined symmetry group G can be
 502 written as

$$\begin{aligned}\psi_1(x) &\xrightarrow{G} \psi'_1(x) \equiv U_Y U_L \psi_1(x), \\ \psi_2(x) &\xrightarrow{G} \psi'_2(x) \equiv U_Y \psi_2(x), \\ \psi_3(x) &\xrightarrow{G} \psi'_3(x) \equiv U_Y \psi_3(x)\end{aligned}\tag{2.10}$$

503 where U_L represent the $SU(2)_L$ transformation acting only on the weak isospin dou-
 504 blet and U_Y represent the $U(1)_Y$ transformation acting on all the weak isospin mul-
 505 tiplets. Explicitly

$$U_L \equiv \exp\left(i \frac{\sigma_i}{2} \alpha^i\right), \quad U_Y \equiv \exp(i y_i \beta) \quad (i = 1, 2, 3) \tag{2.11}$$

506 with σ_i the Pauli matrices and y_i the weak hypercharges. In order to promote the
 507 transformations from global to local while keeping the invariance, it is required that
 508 $\alpha^i = \alpha^i(x)$, $\beta = \beta(x)$ and the replacement of the ordinary derivatives by the covariant
 509 derivatives

$$\begin{aligned}D_\mu \psi_1(x) &\equiv [\partial_\mu + ig\sigma_i W_\mu^i(x)/2 + ig'y_1 B_\mu(x)] \psi_1(x) \\ D_\mu \psi_2(x) &\equiv [\partial_\mu + ig'y_2 B_\mu(x)] \psi_2(x) \\ D_\mu \psi_3(x) &\equiv [\partial_\mu + ig'y_3 B_\mu(x)] \psi_3(x)\end{aligned}\tag{2.12}$$

510 introducing in this way four gauge fields, $W_\mu^i(x)$ and $B_\mu(x)$, in the process. The
 511 covariant derivatives (eqn 2.12) are required to transform in the same way as fermion
 512 fields $\psi_i(x)$ themselves, therefore, the gauge fields transform as:

$$\begin{aligned} B_\mu(x) &\xrightarrow{G} B'_\mu(x) \equiv B_\mu(x) - \frac{1}{g'} \partial_\mu \beta(x) \\ W_\mu^i(x) &\xrightarrow{G} W_\mu^{i\prime}(x) \equiv W_\mu^i(x) - \frac{i}{g} \partial_\mu \alpha_i(x) - \varepsilon_{ijk} \alpha_i(x) W_\mu^j(x). \end{aligned} \quad (2.13)$$

513 The G invariant version of the Lagrangian density 2.8 can be written as

$$\mathcal{L}_0 = \sum_{j=1}^3 i \bar{\psi}_j(x) \gamma^\mu D_\mu \psi_j(x) \quad (2.14)$$

514 where free massless fermion and gauge fields and fermion-gauge boson interactions
 515 are included. The EWI Lagrangian density must additionally include kinetic terms
 516 for the gauge fields (\mathcal{L}_G) which are built from the field strengths, according to

$$B_{\mu\nu}(x) \equiv \partial_\mu B_\nu - \partial_\nu B_\mu \quad (2.15)$$

$$W_{\mu\nu}^i(x) \equiv \partial_\mu W_\nu^i(x) - \partial_\nu W_\mu^i(x) - g \varepsilon^{ijk} W_\mu^j W_\nu^k \quad (2.16)$$

517 the last term in eqn. 2.16 is added in order to hold the gauge invariance; therefore,

$$\mathcal{L}_G = -\frac{1}{4} B_{\mu\nu}(x) B^{\mu\nu}(x) - \frac{1}{4} W_{\mu\nu}^i(x) W_i^{\mu\nu}(x) \quad (2.17)$$

518 which contains not only the free gauge fields contributions, but also the gauge fields
 519 self-interactions and interactions among them.

521 The three weak isospin conserved currents resulting from the $SU(2)_L$ symmetry are
 522 given by

$$J_\mu^i(x) = \frac{1}{2} \bar{\psi}_1(x) \gamma_\mu \sigma^i \psi_1(x) \quad (2.18)$$

523 while the weak hypercharge conserved current resulting from the $U(1)_Y$ symmetry is
 524 given by

$$J_\mu^Y = \sum_{j=1}^3 \bar{\psi}_j(x) \gamma_\mu y_j \psi_j(x) \quad (2.19)$$

525 In order to evaluate the electroweak interactions modeled by an isovector field W_μ^i
 526 which couples to isospin currents J_μ^i with strength g and additionally the singlet
 527 field B_μ which couples to the weak hypercharge current J_μ^Y with strength $g'/2$. The
 528 interaction Lagrangian density to be considered is

$$\mathcal{L}_I = -g J^{i\mu}(x) W_\mu^i(x) - \frac{g'}{2} J^{Y\mu}(x) B_\mu(x) \quad (2.20)$$

529 Note that the weak isospin currents are not the same as the charged fermionic currents
 530 that were used to describe the WI (eqn 2.7), since the weak isospin eigenstates are
 531 not the same as the mass eigenstates, but they are closely related

$$J_\mu = \frac{1}{2} (J_\mu^1 + i J_\mu^2), \quad J_\mu^\dagger = \frac{1}{2} (J_\mu^1 - i J_\mu^2). \quad (2.21)$$

532 The same happens with the gauge fields W_μ^i which are related to the mass eigenstates
 533 W^\pm by

$$W_\mu^+ = \frac{1}{\sqrt{2}} (W_\mu^1 - i W_\mu^2), \quad W_\mu^- = \frac{1}{\sqrt{2}} (W_\mu^1 + i W_\mu^2). \quad (2.22)$$

534 The fact that there are three weak isospin conserved currents is an indication that in
 535 addition to the charged fermionic currents, which couple charged to neutral leptons,
 536 there should be a neutral fermionic current that does not involve electric charge
 537 exchange; therefore, it couples neutral fermions or fermions of the same electric charge.
 538 The third weak isospin current contains a term that is similar to the electromagnetic
 539 current (j_μ^{em}), indicating that there is a relation between them and resembling the
 540 Gell-Mann-Nishijima formula 2.2 adapted to electroweak interactions

$$Q = T_3 + \frac{Y_W}{2}. \quad (2.23)$$

541 Just as Q generates the $U(1)_{em}$ symmetry, the weak hypercharge generates the $U(1)_Y$
 542 symmetry as said before. It is possible to write the relationship in terms of the currents
 543 as

$$j_\mu^{em} = J_\mu^3 + \frac{1}{2}J_\mu^Y. \quad (2.24)$$

544 The neutral gauge fields W_μ^3 and B_μ cannot be directly identified with the Z and the
 545 photon fields since the photon interacts similarly with left and right-handed fermions;
 546 however, they are related through a linear combination given by

$$\begin{aligned} A_\mu &= B_\mu \cos \theta_W + W_\mu^3 \sin \theta_W \\ Z_\mu &= -B_\mu \sin \theta_W + W_\mu^3 \cos \theta_W \end{aligned} \quad (2.25)$$

547 where θ_W is known as the “Weinberg angle.” The interaction Lagrangian is now given

548 by

$$\mathcal{L}_I = -\frac{g}{\sqrt{2}}(J^\mu W_\mu^+ + J^{\mu\dagger} W_\mu^-) - \left(g \sin \theta_W J_\mu^3 + g' \cos \theta_W \frac{J_\mu^Y}{2}\right) A^\mu - \left(g \cos \theta_W J_\mu^3 - g' \sin \theta_W \frac{J_\mu^Y}{2}\right) Z^\mu \quad (2.26)$$

549 the first term is the weak charged current interaction, while the second term is the
550 electromagnetic interaction under the condition

$$g \sin \theta_W = g' \cos \theta_W = e, \quad \frac{g'}{g} = \tan \theta_W \quad (2.27)$$

551 contained in the eqn.2.24; the third term is the neutral weak current.

552

553 Note that the neutral fields transformation given by the eqn. 2.25 can be written in
554 terms of the coupling constants g and g' as:

$$A_\mu = \frac{g' W_\mu^3 + g B_\mu}{\sqrt{g^2 + g'^2}}, \quad Z_\mu = \frac{g W_\mu^3 - g' B_\mu}{\sqrt{g^2 + g'^2}} \quad (2.28)$$

555 So far, the Lagrangian density describing the non-massive EWI is:

$$\mathcal{L}_{nmEWI} = \mathcal{L}_0 + \mathcal{L}_G \quad (2.29)$$

556 where fermion and gauge fields have been considered massless because their regular
557 mass terms are manifestly non invariant under G transformations; therefore, masses
558 have to be generated in a gauge invariant way. The mechanism by which this goal is
559 achieved is known as the “Higgs mechanism” and is closely connected to the concept
560 of “spontaneous symmetry breaking.”

561 2.3.1 Spontaneous symmetry breaking (SSB)

562 Figure 2.6 left shows a steel nail (top) which is subject to an external force; the form
 563 of the potential energy is also shown (bottom).

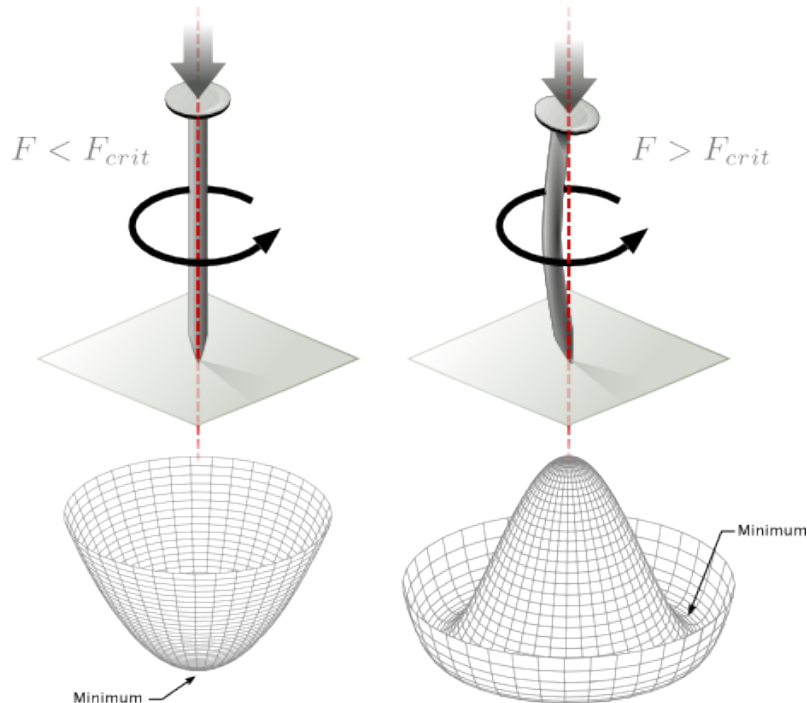


Figure 2.6: Spontaneous symmetry breaking mechanism. The steel nail, subject to an external force (top left), has rotational symmetry with respect to its axis. When the external force overcomes a critical value the nail buckles (top right) choosing a minimal energy state (ground state) and thus “*breaking spontaneously the rotational symmetry*”. The potential energy (bottom) changes but holds the rotational symmetry; however, an infinite number of asymmetric ground states are generated and circularly distributed in the bottom of the potential [27].

564

565 Before reaching the critical force value, the system has rotational symmetry with re-
 566 spect to the nail axis; however, after the critical force value is reached the nail buckles
 567 (top right). The form of the potential energy (bottom right) changes, preserving its
 568 rotational symmetry although its minima does not exhibit that rotational symmetry
 569 any longer. Right before the nail buckles there is no indication of the direction the

570 nail will bend because any of the directions are equivalent, but once the nail bends,
 571 choosing a direction, an arbitrary minimal energy state (ground state) is selected and
 572 it does not share the system's rotational symmetry. This mechanism for reaching an
 573 asymmetric ground state is known as "*spontaneous symmetry breaking*".

574 The lesson from this analysis is that the way to introduce the SSB mechanism into a
 575 system is by adding the appropriate potential to it.

576

577 Figure 2.7 shows a plot of the potential $V(\phi)$ in the case of a scalar field ϕ

$$V(\phi) = \mu^2 \phi^\dagger \phi + \lambda (\phi^\dagger \phi)^2 \quad (2.30)$$

578 If $\mu^2 > 0$ the potential has only one minimum at $\phi = 0$ and describes a scalar field
 579 with mass μ . If $\mu^2 < 0$ the potential has a local maximum at $\phi = 0$ and two minima
 580 at $\phi = \pm\sqrt{-\mu^2/\lambda}$ which enables the SSB mechanism to work.

581

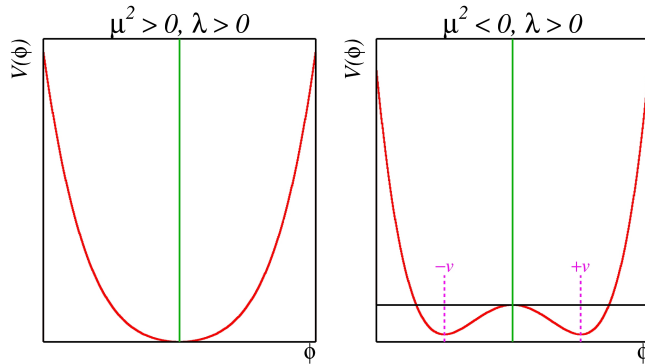


Figure 2.7: Shape of the potential $V(\phi)$ for $\lambda > 0$ and: $\mu^2 > 0$ (left) and $\mu^2 < 0$ (right). The case $\mu^2 < 0$ corresponds to the potential suitable for introducing the SSB mechanism by choosing one of the two ground states which are connected via reflection symmetry. [27].

582 In the case of a complex scalar field $\phi(x)$

$$\phi(x) = \frac{1}{\sqrt{2}}(\phi_1 + i\phi_2) \quad (2.31)$$

583 the Lagrangian (invariant under global $U(1)$ transformations) is given by

$$\mathcal{L} = (\partial_\mu \phi)^\dagger (\partial^\mu \phi) - V(\phi), \quad V(\phi) = \mu^2 \phi^\dagger \phi + \lambda (\phi^\dagger \phi)^2 \quad (2.32)$$

584 where an appropriate potential has been added in order to introduce the SSB.

585

586 As seen in figure 2.8, the potential has now an infinite number of minima circularly
 587 distributed along the ξ -direction which makes possible the occurrence of the SSB by
 588 choosing an arbitrary ground state; for instance, $\xi = 0$, i.e. $\phi_1 = v, \phi_2 = 0$

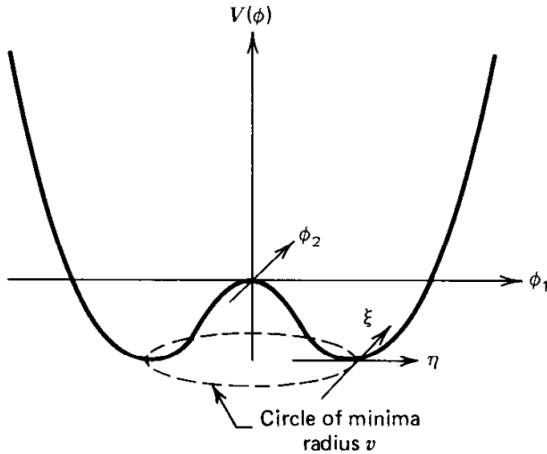


Figure 2.8: Potential for complex scalar field. There is a circle of minima of radius v along the ξ -direction [6].

$$\phi_0 = \frac{v}{\sqrt{2}} \exp(i\xi) \xrightarrow{SSB} \phi_0 = \frac{v}{\sqrt{2}} \quad (2.33)$$

589 As usual, excitations over the ground state are studied by making an expansion about

590 it; thus, the excitation can be parametrized as:

$$\phi(x) = \frac{1}{\sqrt{2}}(v + \eta(x) + i\xi(x)) \quad (2.34)$$

591 which when substituted into eqn. 2.32 produces a Lagrangian in terms of the new
 592 fields η and ξ

$$\mathcal{L}' = \frac{1}{2}(\partial_\mu\xi)^2 + \frac{1}{2}(\partial_\mu\eta)^2 + \mu^2\eta^2 - V(\phi_0) - \lambda v\eta(\eta^2 + \xi^2) - \frac{\lambda}{4}(\eta^2 + \xi^2)^2 \quad (2.35)$$

593 where the last two terms represent the interactions and self-interaction between the
 594 two fields η and ξ . The particular feature of the SSB mechanism is revealed when
 595 looking to the first three terms of \mathcal{L}' . Before the SSB, only the massless ϕ field is
 596 present in the system; after the SSB there are two fields of which the η -field has
 597 acquired mass $m_\eta = \sqrt{-2\mu^2}$ while the ξ -field is still massless (see figure 2.9).

598

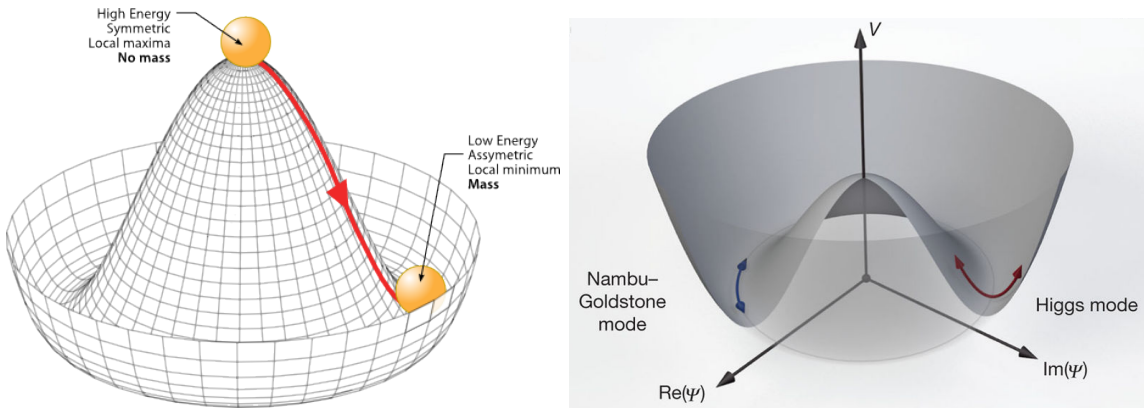


Figure 2.9: SSB mechanism for a complex scalar field [27, 28].

599 Thus, the SSB mechanism serves as a method to generate mass but as a side effect a
 600 massless field is introduced in the system. This fact is known as the Goldstone theorem

and states that a massless scalar field appears in the system for each continuous symmetry spontaneously broken. Another version of the Goldstone theorem states that “*if a Lagrangian is invariant under a continuous symmetry group G , but the vacuum is only invariant under a subgroup $H \subset G$, then there must exist as many massless spin-0 particles (Nambu-Goldstone bosons) as broken generators.*” [26] The Nambu-Goldstone boson can be understood considering that the potential in the ξ -direction is flat so excitations in that direction are not energy consuming and thus represent a massless state.

2.3.2 Higgs mechanism

When the SSB mechanism is introduced in the formulation of the EWI in an attempt to generate the mass of the so far massless gauge bosons and fermions, an interesting effect is revealed. In order to keep the G symmetry group invariance and generate the mass of the EW gauge bosons, a G invariant Lagrangian density (\mathcal{L}_S) has to be added to the non massive EWI Lagrangian (eqn. 2.29)

$$\mathcal{L}_S = (D_\mu \phi)^\dagger (D^\mu \phi) - \mu^2 \phi^\dagger \phi - \lambda (\phi^\dagger \phi)^2, \quad \lambda > 0, \mu^2 < 0 \quad (2.36)$$

$$D_\mu \phi = \left(i\partial_\mu - g \frac{\sigma_i}{2} W_\mu^i - g' \frac{Y}{2} B_\mu \right) \phi \quad (2.37)$$

ϕ has to be an isospin doublet of complex scalar fields so it preserves the G invariance; thus ϕ can be defined as:

$$\phi = \begin{pmatrix} \phi^+ \\ \phi^0 \end{pmatrix} \equiv \frac{1}{\sqrt{2}} \begin{pmatrix} \phi_1 + i\phi_2 \\ \phi_3 + i\phi_4 \end{pmatrix}. \quad (2.38)$$

The minima of the potential are defined by

$$\phi^\dagger \phi = \frac{1}{2}(\phi_1^2 + \phi_2^2 + \phi_3^2 + \phi_4^2) = -\frac{\mu^2}{2\lambda}. \quad (2.39)$$

618 The choice of the ground state is critical. By choosing a ground state, invariant under
 619 $U(1)_{em}$ gauge symmetry, the photon will remain massless and the W^\pm and Z bosons
 620 masses will be generated which is exactly what is needed. In that sense, the best
 621 choice corresponds to a weak isospin doublet with $T_3 = -1/2$, $Y_W = 1$ and $Q = 0$
 622 which defines a ground state with $\phi_1 = \phi_2 = \phi_4$ and $\phi_3 = v$:

$$\phi_0 \equiv \frac{1}{\sqrt{2}} \begin{pmatrix} 0 \\ v \end{pmatrix}, \quad v^2 \equiv -\frac{\mu^2}{\lambda}. \quad (2.40)$$

623 where the vacuum expectation value v is fixed by the Fermi coupling G_F according
 624 to $v = (\sqrt{2}G_F)^{1/2} \approx 246$ GeV.

625

626 The G symmetry has been broken and three Nambu-Goldstone bosons will appear.
 627 The next step is to expand ϕ about the chosen ground state as:

$$\phi(x) = \frac{1}{\sqrt{2}} \exp\left(\frac{i}{v} \sigma_i \theta^i(x)\right) \begin{pmatrix} 0 \\ v + H(x) \end{pmatrix} \approx \frac{1}{\sqrt{2}} \begin{pmatrix} \theta_1(x) + i\theta_2(x) \\ v + H(x) - i\theta_3(x) \end{pmatrix} \quad (2.41)$$

628 to describe fluctuations from the ground state ϕ_0 . The fields $\theta_i(x)$ represent the
 629 Nambu-Goldstone bosons while $H(x)$ is known as “higgs field.” The fundamental
 630 feature of the parametrization used is that the dependence on the $\theta_i(x)$ fields is
 631 factored out in a global phase that can be eliminated by taking the physical “unitary
 632 gauge” $\theta_i(x) = 0$. Therefore the expansion about the ground state is given by:

$$\phi(x) \frac{1}{\sqrt{2}} \begin{pmatrix} 0 \\ v + H(x) \end{pmatrix} \quad (2.42)$$

633 which when substituted into \mathcal{L}_S (eqn. 2.36) results in a Lagrangian containing the now
 634 massive three gauge bosons W^\pm, Z , one massless gauge boson (photon) and the new
 635 Higgs field (H). The three degrees of freedom corresponding to the Nambu-Goldstone
 636 bosons are now integrated into the massive gauge bosons as their longitudinal po-
 637 larizations which were not available when they were massless particles. The effect
 638 by which vector boson fields acquire mass after an spontaneous symmetry breaking,
 639 but without an explicit gauge invariance breaking is known as the “*Higgs mechanism*”.

640

641 The mechanism was proposed by three independent groups: F.Englert and R.Brout
 642 in August 1964 [29], P.Higgs in October 1964 [30] and G.Guralnik, C.Hagen and
 643 T.Kibble in November 1964 [31]; however, its importance was not realized until
 644 S.Glashow [22], A.Salam [23] and S.Weinberg [24], independently, proposed that elec-
 645 tromagnetic and weak interactions are two manifestations of a more general interac-
 646 tion called “electroweak interaction” in 1967.

647 2.3.3 Masses of the gauge bosons

648 The mass of the gauge bosons is extracted by evaluating the kinetic part of Lagrangian
 649 \mathcal{L}_S in the ground state (known also as the vacuum expectation value), i.e.,

$$\left| \left(\partial_\mu - ig \frac{\sigma_i}{2} W_\mu^i - i \frac{g'}{2} B_\mu \right) \phi_0 \right|^2 = \left(\frac{1}{2} v g \right)^2 W_\mu^+ W^{-\mu} + \frac{1}{8} v^2 (W_\mu^3, B_\mu) \begin{pmatrix} g^2 & -gg' \\ -gg' & g'^2 \end{pmatrix} \begin{pmatrix} W^{3\mu} \\ B^\mu \end{pmatrix} \quad (2.43)$$

650 comparing with the typical mass term for a charged boson $M_W^2 W^+ W^-$

$$M_W = \frac{1}{2} v g. \quad (2.44)$$

The second term in the right side of the eqn.2.43 comprises the masses of the neutral

bosons, but it needs to be written in terms of the gauge fields Z_μ and A_μ in order to be compared to the typical mass terms for neutral bosons, therefore using eqn. 2.28

$$\begin{aligned} \frac{1}{8}v^2[g^2(W_\mu^3)^2 - 2gg'W_\mu^3B^\mu + g'^2B_\mu^2] &= \frac{1}{8}v^2[gW_\mu^3 - g'B_\mu]^2 + 0[g'W_\mu^3 + gB_\mu]^2 \\ &= \frac{1}{8}v^2[\sqrt{g^2 + g'^2}Z_\mu]^2 + 0[\sqrt{g^2 + g'^2}A_\mu]^2 \end{aligned} \quad (2.45)$$

651 and then

$$M_Z = \frac{1}{2}v\sqrt{g^2 + g'^2}, \quad M_A = 0 \quad (2.46)$$

652 2.3.4 Masses of the fermions

653 The lepton mass terms can be generated by introducing a gauge invariant Lagrangian
654 term describing the Yukawa coupling between the lepton field and the Higgs field

$$\mathcal{L}_{Yl} = -G_l \left[(\bar{\nu}_l, \bar{l})_L \begin{pmatrix} \phi^+ \\ \phi^0 \end{pmatrix} l_R + \bar{l}_R (\phi^-, \bar{\phi}^0) \begin{pmatrix} \nu_l \\ l \end{pmatrix}_L \right], \quad l = e, \mu, \tau. \quad (2.47)$$

655 After the SSB and replacing the usual field expansion about the ground state (eqn.2.40)
656 into \mathcal{L}_{Yl} , the mass term arises

$$\mathcal{L}_{Yl} = -m_l(\bar{l}_L l_R + \bar{l}_R l_L) - \frac{m_l}{v}(\bar{l}_L l_R + \bar{l}_R l_L)H = -m_l \bar{l} \left(1 + \frac{H}{v} \right) \quad (2.48)$$

657

$$m_l = \frac{G_l}{\sqrt{2}}v \quad (2.49)$$

658 where the additional term represents the lepton-Higgs interaction. The quark masses
659 are generated in a similar way as lepton masses but for the upper member of the

660 quark doublet a different Higgs doublet is needed:

$$\phi_c = -i\sigma_2\phi^* = \begin{pmatrix} -\bar{\phi}^0 \\ \phi^- \end{pmatrix}. \quad (2.50)$$

661 Additionally, given that the quark isospin doublets are not constructed in terms of
 662 the mass eigenstates but in terms of the flavor eigenstates, as shown in table 2.5, the
 663 coupling parameters will be related to the CKM matrix elements; thus the quark
 664 Lagrangian is given by:

$$\mathcal{L}_{Yq} = -G_d^{i,j}(\bar{u}_i, \bar{d}_i)_L \begin{pmatrix} \phi^+ \\ \phi^0 \end{pmatrix} d_{jR} - G_u^{i,j}(\bar{u}_i, \bar{d}_i)_L \begin{pmatrix} -\bar{\phi}^0 \\ \phi^- \end{pmatrix} u_{jR} + h.c. \quad (2.51)$$

665 with $i,j=1,2,3$. After SSB and expansion about the ground state, the diagonal form
 666 of \mathcal{L}_{Yq} is:

$$\mathcal{L}_{Yq} = -m_d^i \bar{d}_i d_i \left(1 + \frac{H}{v} \right) - m_u^i \bar{u}_i u_i \left(1 + \frac{H}{v} \right) \quad (2.52)$$

667 Fermion masses depend on arbitrary couplings G_l and $G_{u,d}$ and are not predicted by
 668 the theory.

669 2.3.5 The Higgs field

670 After the characterization of the fermions and gauge bosons as well as their interac-
 671 tions, it is necessary to characterize the Higgs field itself. The Lagrangian \mathcal{L}_S in eqn.
 672 2.36 written in terms of the gauge bosons is given by

$$\mathcal{L}_S = \frac{1}{4}\lambda v^4 + \mathcal{L}_H + \mathcal{L}_{HV} \quad (2.53)$$

673

$$\mathcal{L}_H = \frac{1}{2}\partial_\mu H \partial^\mu H - \frac{1}{2}m_H^2 H^2 - \frac{1}{2v}m_H^2 H^3 - \frac{1}{8v^2}m_H^2 H^4 \quad (2.54)$$

674

$$\mathcal{L}_{HV} = m_H^2 W_\mu^+ W^{\mu-} \left(1 + \frac{2}{v}H + \frac{2}{v^2}H^2 \right) + \frac{1}{2}m_Z^2 Z_\mu Z^\mu \left(1 + \frac{2}{v}H + \frac{2}{v^2}H^2 \right) \quad (2.55)$$

675 The mass of the Higgs boson is deduced as usual from the mass term in the Lagrangian
 676 resulting in:

$$m_H = \sqrt{-2\mu^2} = \sqrt{2\lambda}v \quad (2.56)$$

677 however, it is not predicted by the theory either. The experimental efforts to find
 678 the Higgs boson, carried out by the “Compact Muon Solenoid (CMS)” experiment
 679 and the “A Toroidal LHC AppartuS (ATLAS)” experiments at the “Large Hadron
 680 Collider(LHC)”, gave great results by July of 2012 when the discovery of a new
 681 particle compatible with the Higgs boson predicted by the electroweak theory [32, 33]
 682 was announced. Although at the announcement time there were some reservations
 683 about calling the new particle the “Higgs boson”, today this name is widely accepted.
 684 The Higgs mass measurement, reported by both experiments [34], is in table 2.8.

Property	Value
Electric charge	0
Colour charge	0
Spin	0
Weak isospin	-1/2
Weak hypercharge	1
Parity	1
Mass (GeV/c ²)	125.09±0.21 (stat.)±0.11 (syst.)

Table 2.8: Higgs boson properties. Higgs mass is not predicted by the theory and the value here corresponds to the experimental measurement.

685

686 2.3.6 Production of Higgs bosons at LHC

687 At LHC, Higgs boson is produced as a result of the collision of two counter-rotating
 688 protons beams. A detailed description of the LHC machine will be presented in
 689 chapter 3. “The total cross section” is a parameter that quantifies the number of pp
 690 collisions that happen when a number of protons are fired at each other. Different
 691 results can be obtained after a pp collision and for each one the “cross section” is

defined as the number of pp collisions that conclude in that particular result with respect to the number of protons fired at each other.

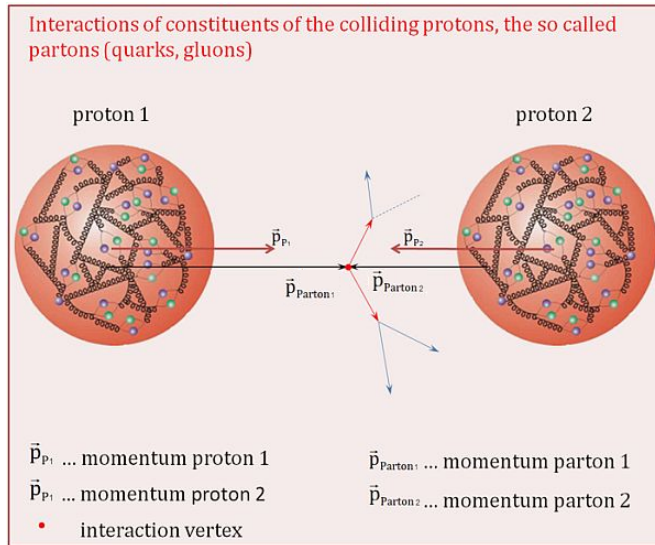


Figure 2.10: Proton-proton collision. Protons are composed of 3 valence quarks, a sea of quarks and gluons; therefore in a proton-proton collision, quarks and gluons are those who collide. [35].

693

694 Protons are composed of quarks and these quarks are bound by gluons; however,
695 what is commonly called the quark content of the proton makes reference to the
696 valence quarks. A sea of quarks and gluons is also present inside the proton as repre-
697 sented in figure 2.10. In a proton-proton (pp) collision, the constituents (quarks and
698 gluons) are those who collide. The pp cross section depends on the momentum of
699 the colliding particles, reason for which it is needed to know how the momentum is
700 distributed inside the proton. Quarks and gluons are known as partons and the func-
701 tions that describe how the proton momentum is distributed among partons inside it
702 are called “parton distribution functions (PDFs)”; PDFs are determined from experi-
703 mental data obtained in experiments where the internal structure of hadrons is tested.

704

⁷⁰⁵ In addition, in physics, a common approach to study complex systems consists in

706 starting with a simpler version of them, for which a well known description is avail-
 707 able, and add an additional “perturbation” which represents a small deviation from
 708 the known behavior. If the perturbation is small enough, the physical quantities as-
 709 sociated with the perturbed system are expressed as a series of corrections to those
 710 of the simpler system; therefore, the more terms are considered in the series (the
 711 higher order in the perturbation series), the more precise is the the description of the
 712 complex system.

713

714 This thesis explores the Higgs production at LHC; therefore the overview presented
 715 here will be oriented specifically to the production mechanisms after pp collisions at
 716 LHC.

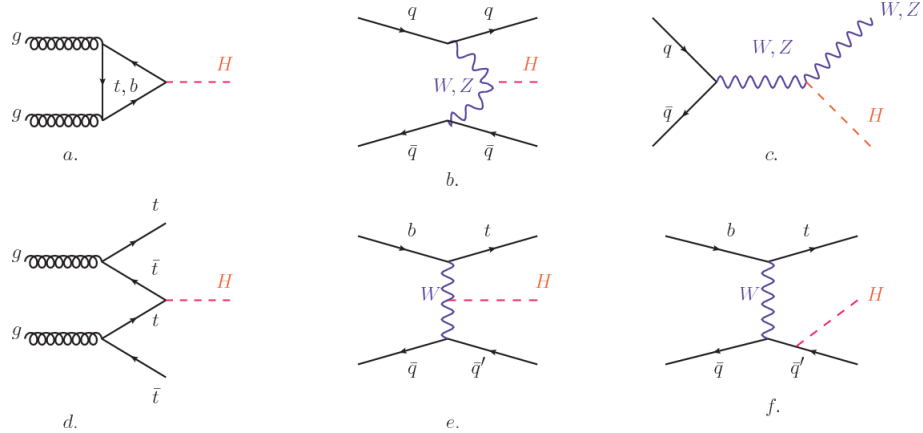


Figure 2.11: Main Higgs boson production mechanism Feynman diagrams. a. gluon-gluon fusion, b. vector boson fusion (VBF), c. Higgs-strahlung, d. Associated production with a top or bottom quark pair, e-f. associated production with a single top quark.

717 Figure 2.11 shows the Feynman diagrams for the leading order (first order) Higgs
 718 production processes at LHC, while the cross section for Higgs production as a func-
 719 tion of the center of mass-energy (\sqrt{s}) for pp collisions is showed in figure 2.12 left.
 720 The tags NLO (next to leading order), NNLO (next to next to leading order) and
 721 N3LO (next to next to next to leading order) make reference to the order at which

722 the perturbation series have been considered.

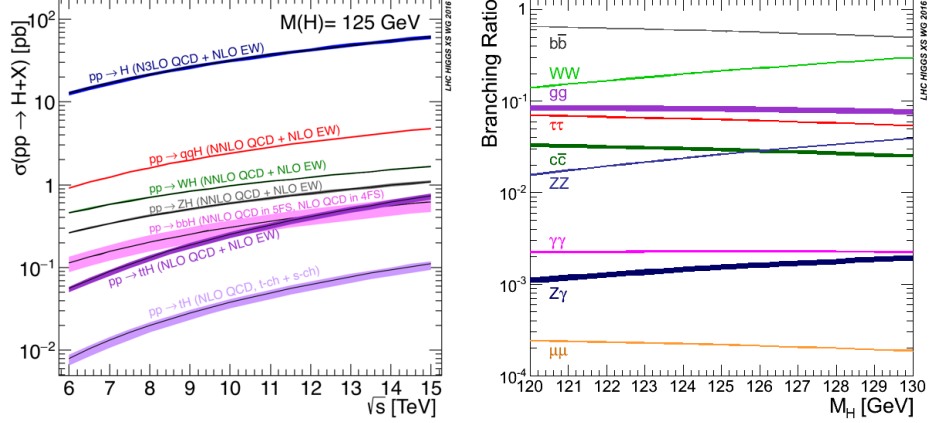


Figure 2.12: Higgs boson production cross sections (left) and decay branching ratios (right) for the main mechanisms. The VBF is indicated as $q\bar{q}H$ [36].

723 As shown in eqns 2.47, 2.51 and 2.55, the strength of the Higgs-fermion interaction
 724 is proportional to the fermion mass while the strength of the Higgs-gauge boson
 725 interaction is proportional to the square of the gauge boson mass, which implies
 726 that the Higgs production and decay mechanisms are dominated by couplings $H -$
 727 (W, Z, t, b, τ) .

728 The main production mechanism is the gluon fusion (figure 2.11a and $pp \rightarrow H$ in figure
 729 2.12) given that gluons carry the highest fraction of momentum of the protons in pp
 730 colliders. Since the Higgs boson does not couple to gluons, the mechanism proceeds
 731 through the exchange of a virtual top-quark loop given that for it the coupling is
 732 the biggest. Note that in this process, the Higgs boson is produced alone, which
 733 makes this mechanism experimentally clean when combined with the two-photon or
 734 the four-lepton decay channels (see section 2.3.7).

735 Vector boson fusion (figure 2.11b and $pp \rightarrow q\bar{q}H$ in figure 2.12) has the second largest
 736 production cross section. The scattering of two fermions is mediated by a weak
 737 gauge boson which later emits a Higgs boson. In the final state, the two fermions

738 tend to be located in a particular region of the detector which is used as a signature
 739 when analyzing the datasets provided by the experiments. More details about how
 740 to identify events of interest in an analysis will be given in chapter ??.

741 The next production mechanism is Higgs-strahlung (figure 2.11c and $pp \rightarrow WH, pp \rightarrow$
 742 ZH in figure 2.12) where two fermions annihilate to form a weak gauge boson. If the
 743 initial fermions have enough energy, the emergent boson eventually will emit a Higgs
 744 boson.

745 The associated production with a top or bottom quark pair and the associated pro-
 746 duction with a single top quark (figure 2.11d-f and $pp \rightarrow bbH, pp \rightarrow t\bar{t}H, pp \rightarrow tH$
 747 in figure 2.12) have a smaller cross section than the main three mechanisms above,
 748 but they provide a good opportunity to test the Higgs-top coupling. The analysis
 749 reported in this thesis is developed using these production mechanisms. A detailed
 750 description of the tH mechanism will be given in section 2.4.

751 2.3.7 Higgs boson decay channels

752 When a particle can decay through several modes, also known as channels, the
 753 probability of decaying through a given channel is quantified by the “branching ratio
 754 (BR)” of the decay channel; thus, the BR is defined as the ratio of number of decays
 755 going through that given channel to the total number of decays. In regard to the
 756 Higgs boson decay, the BR can be predicted with accuracy once the Higgs mass is
 757 known [37, 38]. In figure 2.12 right, a plot of the BR as a function of the Higgs mass
 758 is presented. The largest predicted BR corresponds to the $b\bar{b}$ pair decay channel (see
 759 table 2.9).

Decay channel	Branching ratio	Rel. uncertainty
$H \rightarrow b\bar{b}$	5.84×10^{-1}	$+3.2\% - 3.3\%$
$H \rightarrow W^+W^-$	2.14×10^{-1}	$+4.3\% - 4.2\%$
$H \rightarrow \tau^+\tau^-$	6.27×10^{-2}	$+5.7\% - 5.7\%$
$H \rightarrow ZZ$	2.62×10^{-2}	$+4.3\% - 4.1\%$
$H \rightarrow \gamma\gamma$	2.27×10^{-3}	$+5.0\% - 4.9\%$
$H \rightarrow Z\gamma$	1.53×10^{-3}	$+9.0\% - 8.9\%$
$H \rightarrow \mu^+\mu^-$	2.18×10^{-4}	$+6.0\% - 5.9\%$

Table 2.9: Predicted branching ratios and the relative uncertainty for a SM Higgs boson with $m_H = 125\text{GeV}/c^2$. [9]

⁷⁶¹ 2.4 Associated production of a Higgs boson and a
⁷⁶² single Top quark.

Associated production of Higgs boson has been extensively studied [39–43]. While measurements of the main Higgs production mechanisms rates are sensitive to the strength of the Higgs coupling to W boson or top quark, they are not sensitive to the relative sign between the two couplings. In this thesis, the Higgs boson production mechanism explored is the associated production with a single top quark ($t\bar{h}$) which offers sensitiveness to the relative sign of the Higgs couplings to W boson and to top quark. The description given here is based on the reference [41]

770
771 A process where two incoming particles interact and produce a final state with two
772 particles can proceed in three ways also called channels (see, for instance, figure 2.13
773 ommiting the red line). The t-channel represents processes where an intermediate
774 particle is emitted by one of the incoming particles and absorbed by the other. The
775 s-channel represents processes where the two incoming particles merge into an inter-
776 mediate particle which eventually will split into the particles in the final state. The
777 third channel, u-channel, is similar to the t-channel but the two outgoing particles

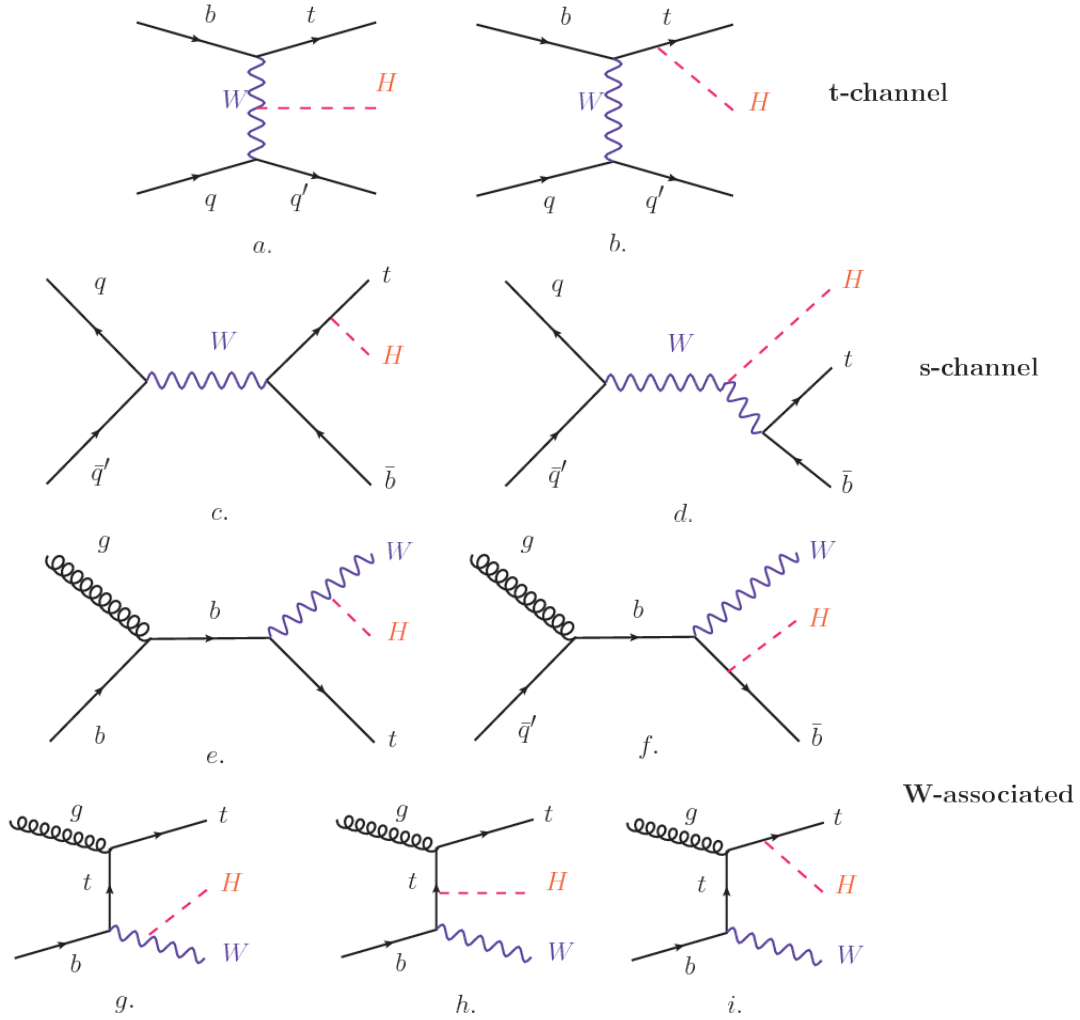


Figure 2.13: Associated Higgs boson production mechanism Feynman diagrams. a.,b. t-channel (tHq), c.,d. s-channel (tHb), e-i. W-associated.

778 interchange their roles.

779

780 The *th* production, where Higgs boson can be radiated either from the top quark or
 781 from the W boson, is represented by the leading order Feynman diagrams in figure
 782 2.13. The cross section for the *th* process is calculated, as usual, summing over
 783 the contributions from the different feynman diagrams; therefore it depends on the
 784 interference between the contributions. In the SM, the interference for t-channel (tHq

785 process) and W-associated (tHW process) production is destructive [39] resulting in
 786 the small cross sections presented in table 2.10.

tH production channel	Cross section (fb)
t-channel ($pp \rightarrow tHq$)	$70.79^{+2.99}_{-4.80}$
W-associated ($pp \rightarrow tHW$)	$15.61^{+0.83}_{-1.04}$
s-channel($pp \rightarrow tHb$)	$2.87^{+0.09}_{-0.08}$

Table 2.10: Predicted SM cross sections for tH production at $\sqrt{s} = 13$ TeV [44, 45].

787

788 While the s-channel contribution can be neglected, it will be shown that a deviation
 789 from the SM destructive interference would result in an enhancement of the th cross
 790 section compared to that in SM, which could be used to get information about the
 791 sign of the Higgs-top coupling [41, 42]. In order to describe th production processes,
 792 Feynman diagram 2.13b will be considered; there, the W boson is radiated by a
 793 quark in the proton and eventually it will interact with the b quark. In the high
 794 energy regime, the effective W approximation [46] allows to describe the process as
 795 the emmission of an approximately on-shell W and its hard scattering with the b
 796 quark; i.e. $Wb \rightarrow th$. The scattering amplitude for the process is given by

$$\mathcal{A} = \frac{g}{\sqrt{2}} \left[(\kappa_t - \kappa_V) \frac{m_t \sqrt{s}}{m_W v} A \left(\frac{t}{s}, \varphi; \xi_t, \xi_b \right) + \left(\kappa_V \frac{2m_W s}{v} \frac{1}{t} + (2\kappa_t - \kappa_V) \frac{m_t^2}{m_W v} \right) B \left(\frac{t}{s}, \varphi; \xi_t, \xi_b \right) \right], \quad (2.57)$$

797 where $\kappa_V \equiv g_{HVV}/g_{HVV}^{SM}$ and $\kappa_t \equiv g_{Ht}/g_{Ht}^{SM} = y_t/y_t^{SM}$ are scaling factors that quan-
 798 tify possible deviations of the couplings, Higgs-Vector boson (H-W) and Higgs-top
 799 (H-t) respectively, from the SM couplings; $s = (p_W + p_b)^2$, $t = (p_W - p_H)^2$, φ is the
 800 Higgs azimuthal angle around the z axis taken parallel to the direction of motion of
 801 the incoming W; A and B are funtions describing the weak interaction in terms of

802 the chiral states of the quarks b and t . Terms that vanish in the high energy limit
 803 have been neglected as well as the Higgs and b quark masses⁸.

804

805 The scattering amplitude grows with energy like \sqrt{s} for $\kappa_V \neq \kappa_t$, in contrast to
 806 the SM ($\kappa_t = \kappa_V = 1$), where the first term in 2.57 cancels out and the amplitude
 807 is constant for large s ; therefore, a deviation from the SM predictions represents an
 808 enhancement in the tHq cross section. In particular, for a SM H-W coupling and a H-t
 809 coupling of inverted sign with respect to the SM ($\kappa_V = -\kappa_t = 1$) the tHq cross section
 810 is enhanced by a factor greater 10 as seen in the figure 2.14 taken from reference [41];
 811 reference [47] has reported similar enhancement results.

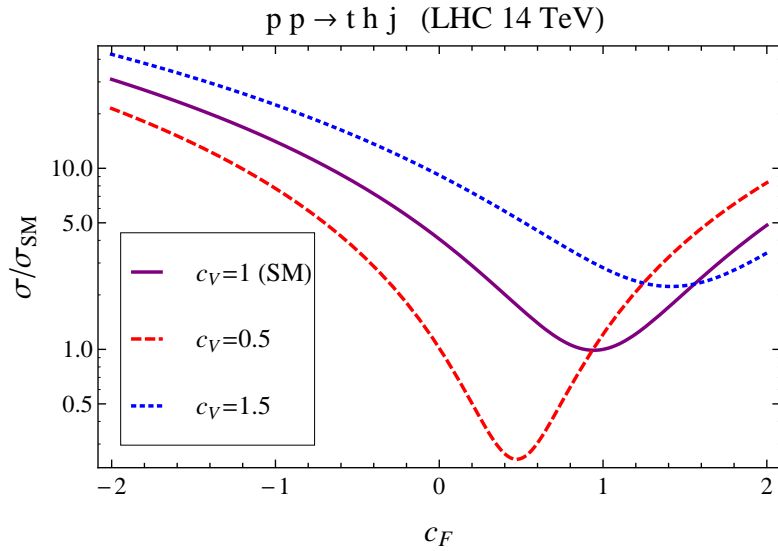


Figure 2.14: Cross section for tHq process as a function of κ_t , normalized to the SM, for three values of κ_V . In the plot c_f refers to the Higgs-fermion coupling which is dominated by the H-t coupling and represented here by κ_t . Solid, dashed and dotted lines correspond to $c_V \rightarrow \kappa_V = 1, 0.5, 1.5$ respectively. Note that for the SM ($\kappa_V = \kappa_t = 1$), the destructive effect of the interference is maximal.

812 A similar analysis is valid for the W-associated channel but, in that case, the inter-
 813 ference is more complicated since there are more than two contributions and an ad-

⁸ A detailed explanation of the structure and approximations used to derive \mathcal{A} can be found in reference [41]

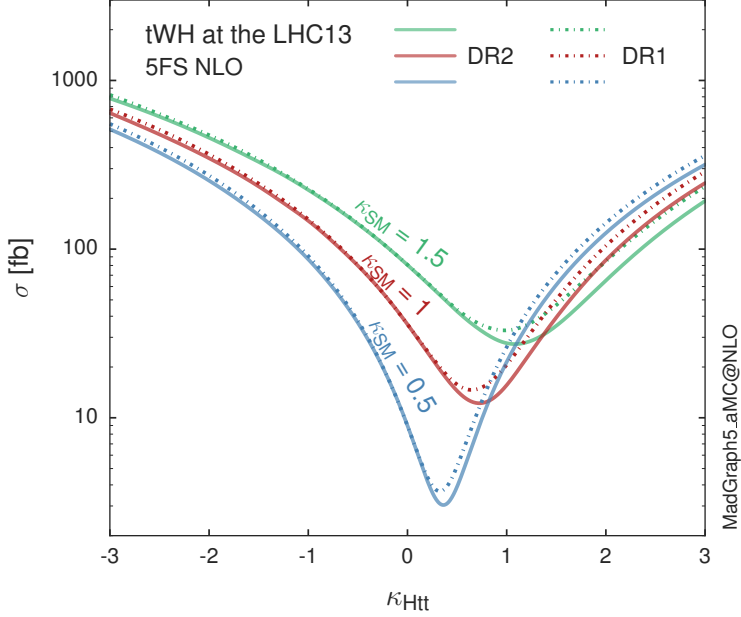


Figure 2.15: Cross section for tHW process as a function of κ_{Htt} , for three values of κ_{SM} at $\sqrt{s} = 13$ TeV. $\kappa_{Htt}^2 = \sigma_{Htt}/\sigma_{Htt}^{SM}$ is a simple rescaling of the SM Higgs interactions.

ditional interference with the production of Higgs boson and a top pair process($t\bar{t}H$).
The calculations are made using the so-called Diagram Removal (DR) technique where
interfering diagrams are removed (or added) from the calculations in order to evaluate
the impact of the removed contributions. DR1 was defined to neglect $t\bar{t}H$ interference
while DR2 was defined to take $t\bar{t}H$ interference into account [48]. As shown in figure
2.15, the tHW cross section is enhanced from about 15 fb (SM: $\kappa_{Htt} = 1$) to about
150 fb ($\kappa_{Htt} = -1$). Differences between curves for DR1 and DR2 help to gauge the
impact of the interference with $t\bar{t}H$.
Results of the calculations of the tHq and tHW cross sections at $\sqrt{s} = 13$ TeV can be
found in reference [49] and a summary of the results is presented in table 2.11.

	\sqrt{s} TeV	$\kappa_t = 1$	$\kappa_t = -1$
$\sigma^{LO}(tHq)(\text{fb})$ [41]	8	≈ 17.4	≈ 252.7
	14	≈ 80.4	≈ 1042
$\sigma^{NLO}(tHq)(\text{fb})$ [41]	8	$18.28^{+0.42}_{-0.38}$	$233.8^{+4.6}_{-0.0}$
	14	$88.2^{+1.7}_{-0.0}$	$982.8^{+28}_{-0.0}$
$\sigma^{LO}(tHq)(\text{fb})$ [47]	14	≈ 71.8	≈ 893
$\sigma^{LO}(tHW)(\text{fb})$ [47]	14	≈ 16.0	≈ 139
$\sigma^{NLO}(tHq)(\text{fb})$ [49]	8	$18.69^{+8.62\%}_{-17.13\%}$	-
	13	$74.25^{+7.48\%}_{-15.35\%}$	$848^{+7.37\%}_{-13.70\%}$
	14	$90.10^{+7.34\%}_{-15.13\%}$	$1011^{+7.24\%}_{-13.39\%}$
$\sigma^{LO}(tHW)(\text{fb})$ [48]	13	$15.77^{+15.91\%}_{-15.76\%}$	-
$\sigma^{NLO} DR1(tHW)(\text{fb})$ [48]	13	$21.72^{+6.52\%}_{-5.24\%}$	≈ 150
$\sigma^{NLO} DR2(tHW)(\text{fb})$ [48]	13	$16.28^{+7.34\%}_{-15.13\%}$	≈ 150

Table 2.11: Predicted enhancement of the tHq and tHW cross sections at LHC for $\kappa_V = 1$ and $\kappa_t = \pm 1$ at LO and NLO; the cross section enhancement of more than a factor of 10 is due to the flippling in the sign of the H-t coupling with respect to the SM one.

825 2.5 The CP-mixing in tH processes

826 In addition to the sensitivity to sign of the H-t coupling, tHq and tHW processes have
 827 been proposed as a tool to investigate the possibility of a H-t coupling that does not
 828 conserve CP [43, 48, 50]. Current experimental results are consistent with SM H-V
 829 and H-t couplings; however, negative H-t coupling is not excluded completely [52].

830

831 In this thesis, the sensitivity of th processes to CP-mixing is also studied in the
 832 effective field theory framework and based in references [43, 48]; a generic particle
 833 (X_0) of spin-0 and a general CP violating interaction with the top quark, can couple
 834 to scalar and pseudoscalar fermionic densities. The H-W interaction is assumed to
 835 be SM-like. The Lagrangian modeling the H-t interaction is given by

$$\mathcal{L}_0^t = -\bar{\psi}_t (c_\alpha \kappa_{Htt} g_{Htt} + i s_\alpha \kappa_{Att} g_{Att} \gamma_5) \psi_t X_0, \quad (2.58)$$

836 where α is the CP-mixing phase, $c_\alpha \equiv \cos \alpha$ and $s_\alpha \equiv \sin \alpha$, κ_{Htt} and κ_{Att} are real
 837 dimensionless rescaling parameters⁹, $g_{Htt} = g_{Att} = m_t/v = y_t/\sqrt{2}$ and $v \sim 246$ GeV is
 838 the Higgs vacuum expectation value. In this parametrization, it is easy to recover
 839 three special cases

- 840 • CP-even coupling $\rightarrow \alpha = 0^\circ$
 841 • CP-odd coupling $\rightarrow \alpha = 90^\circ$
 842 • SM coupling $\rightarrow \alpha = 0^\circ$ and $\kappa_{Htt} = 1$

843 The loop induced X_0 coupling to gluons can also be described in terms of the
 844 parametrization above, according to

$$\mathcal{L}_0^g = -\frac{1}{4} \left(c_\alpha \kappa_{Hgg} g_{Hgg} G_{\mu\nu}^a G^{a,\mu\nu} + s_\alpha \kappa_{Agg} g_{Agg} G_{\mu\nu}^a \tilde{G}^{a,\mu\nu} \right) X_0. \quad (2.59)$$

845 where $g_{Hgg} = -\alpha_s/3\pi v$ and $g_{Agg} = \alpha_s/2\pi v$. Under the assumption that the top quark
 846 dominates the gluon-fusion process at LHC energies, $\kappa_{Hgg} \rightarrow \kappa_{Htt}$ and $\kappa_{Agg} \rightarrow \kappa_{Att}$,
 847 so that the ratio between the gluon-gluon fusion cross section for X_0 and for the SM
 848 Higgs prediction can be written as

$$\frac{\sigma_{NLO}^{gg \rightarrow X_0}}{\sigma_{NLO,SM}^{gg \rightarrow H}} = c_\alpha^2 \kappa_{Htt}^2 + s_\alpha^2 \left(\kappa_{Att} \frac{g_{Agg}}{g_{Hgg}} \right)^2. \quad (2.60)$$

849 If the rescaling parameters are set to

$$\kappa_{Htt} = 1, \quad \kappa_{Att} = \left| \frac{g_{Hgg}}{g_{Agg}} \right| = \frac{2}{3}. \quad (2.61)$$

850 the gluon-fusion SM cross section is reproduced for every value of the CP-mixing
 851 angle α ; therefore, by imposing that condition to the Lagrangian density 2.58, the

⁹ analog to κ_t and κ_V

CP-mixing angle is not constrained by current data. Figure 2.16 shows the NLO cross sections for t-channel tX_0 (blue) and $t\bar{t}X_0$ (red) associated production processes as a function of the CP-mixing angle α . X_0 is a generic spin-0 particle with top quark CP-violating coupling. Rescaling factors κ_{Htt} and κ_{Att} have been set to reproduce the SM gluon-fusion cross sections.

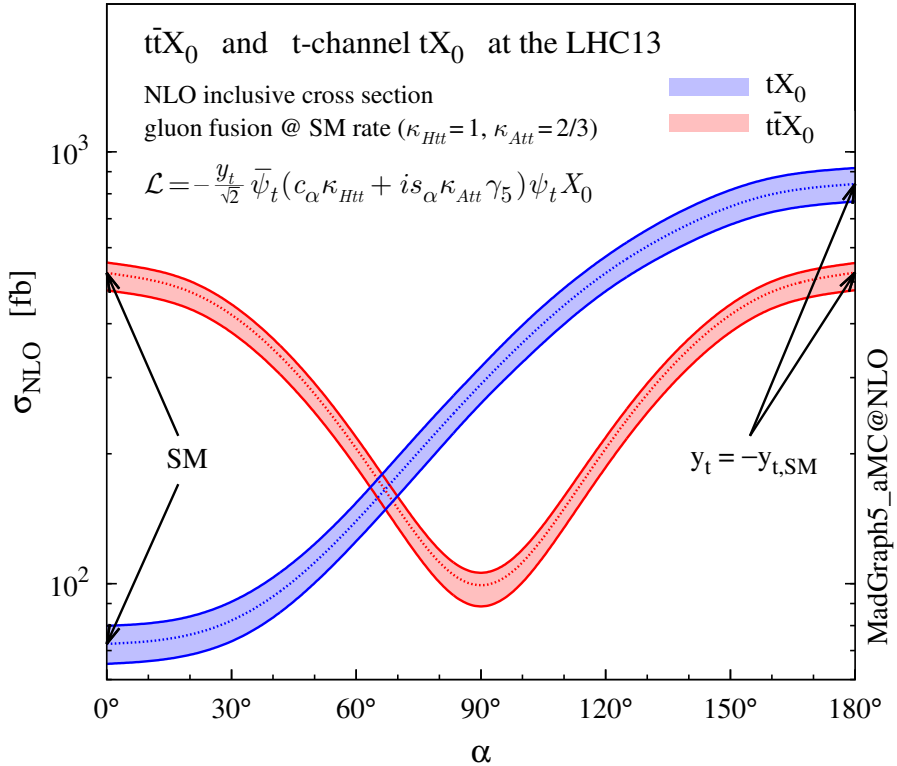


Figure 2.16: NLO cross sections for t-channel tX_0 (blue) and $t\bar{t}X_0$ (red) associated production processeses as a function of the CP-mixing angle α . X_0 is a generic spin-0 particle with top quark CP-violating coupling [43].

It is interesting to notice that the tX_0 croos section is enhanced, by a factor of about 10, when a continuous rotation in the scalar-pseudoscalar plane is applied; this enhancement is similar to the enhancement produced when the H-t coupling is flipped in sign with respect to the SM ($y_t = -y_{t,SM}$ in the plot), as showed in section 2.4. In contrast, the degeneracy in the $t\bar{t}X_0$ cross section is still present given that it depends

quadratically on the H-t coupling, but more interesting is to notice that $t\bar{t}X_0$ cross section is exceeded by tX_0 cross section after $\alpha \sim 60^\circ$.

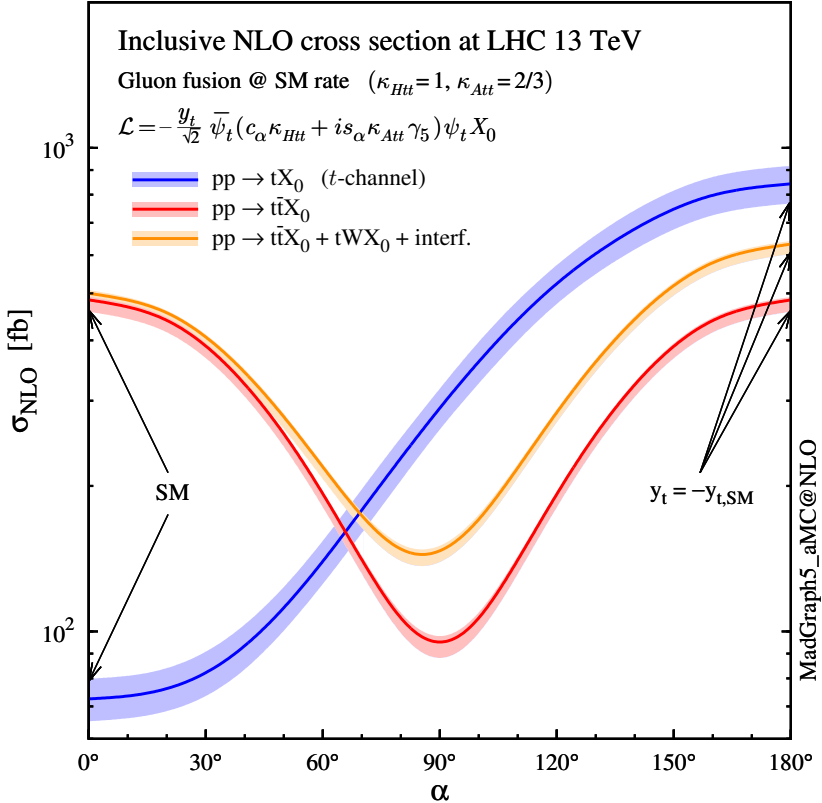


Figure 2.17: NLO cross sections for t-channel tX_0 (blue), $t\bar{t}X_0$ (red) associated production processes and combined $tWX_0 + t\bar{t}X_0$ (including interference) production as a function of the CP-mixing angle α [43].

863

864 A similar parametrization can be used to investigate the tHW process sensitivity to
 865 CP-violating H-t coupling. As said in 2.4, the interference in the W-associated chan-
 866 nel is more complicated because there are more than two contributions and also there
 867 is interference with the $t\bar{t}H$ production process.

868

869 Figure 2.17 shows the NLO cross sections for t-channel tX_0 (blue), $t\bar{t}X_0$ (red) asso-
 870 ciated production and for the combined $tWX_0 + t\bar{t}X_0 +$ interference (orange) as a
 871 function of the CP-mixing angle. It is clear that the effect of the interference in the

combined case is the lifting of the degeneracy present in the $t\bar{t}X_0$ production. The constructive interference enhances the cross section from about 500 fb at SM ($\alpha = 0$) to about 600 fb ($\alpha = 180^\circ \rightarrow y_t = -y_{t,SM}$).

An analysis combining tHq and tHW processes will be made in this thesis taking advantage of the sensitivity improvement.

2.6 Experimantal status of the anomalous Higg-fermion coupling.

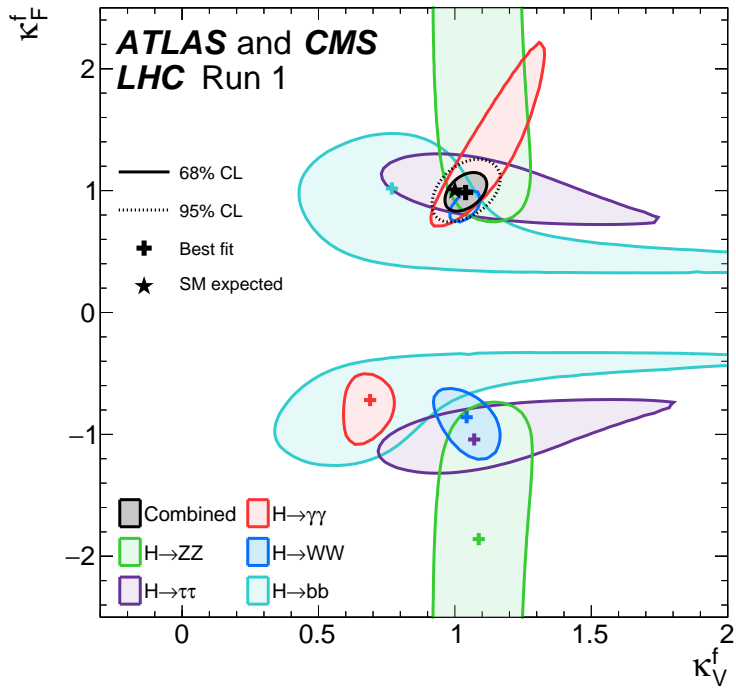


Figure 2.18: Combination of the ATLAS and CMS fits for coupling modifiers κ_t - κ_V ; also shown the individual decay channels combination and their global combination. No assumptions have been made on the sign of the coupling modifiers [52].

ATLAS and CMS have performed analysis of the anomalous H-f coupling by making likelihood scans for the two coupling modifiers, κ_t and κ_V , under the assumption that

881 $\kappa_Z = \kappa_W = \kappa_V$ and $\kappa_t = \kappa_\tau = \kappa_b = \kappa_f$. Figure 2.18 shows the result of the combination
882 of ATLAS and CMS fits; also the individual decay channels combination and the
883 global combination results are shown.

884 While all the channels are compatible for positive values of the modifiers, for negative
885 values of κ_t there is no compatibility. The best fit for individual channels is compatible
886 with negative values of κ_t except for the $H \rightarrow bb$ channel which is expected to be the
887 most sensitive channel; therefore, the best fit for the global fit yields $\kappa_t \geq 0$. Thus,
888 the anomalous H-t coupling cannot be excluded completely.

⁸⁸⁹ **Chapter 3**

⁸⁹⁰ **The CMS experiment at the LHC**

⁸⁹¹ **3.1 Introduction**

⁸⁹² Located on the Swiss-French border, the European Council for Nuclear Research
⁸⁹³ (CERN) is the largest scientific organization leading the particle physics research.
⁸⁹⁴ About 13000 people in a broad range of fields including users, students, scientists,
⁸⁹⁵ engineers among others, contribute to the data taking and analysis, with the goal
⁸⁹⁶ of unveiling the secrets of nature and revealing the fundamental structure of the
⁸⁹⁷ universe. CERN is also the home of the Large Hadron Collider (LHC), the largest
⁸⁹⁸ circular particle accelerator around the world, where protons (or heavy ions) traveling
⁸⁹⁹ close to the speed of light, are made to collide. These collisions open a window
⁹⁰⁰ to investigate how particles (and their constituents if they are composite) interact
⁹⁰¹ with each other, providing clues about the laws of nature. This chapter presents an
⁹⁰² overview of the LHC structure and operation. A detailed description of the CMS
⁹⁰³ detector is offered, given that the data used in this thesis have been taken with this
⁹⁰⁴ detector.

905 3.2 The LHC

906 With 27 km of circumference, the LHC is currently the largest and most powerful
 907 circular accelerator in the world. It is installed in the same tunnel where the Large
 908 Electron-Positron (LEP) collider was located, taking advantage of the existing infras-
 909 tructure. The LHC is also the larger accelerator in the CERN's accelerator complex
 910 and is assisted by several successive accelerating stages before the particles are in-
 911 jected into the LHC ring where they reach their maximum energy (see figure 3.1).

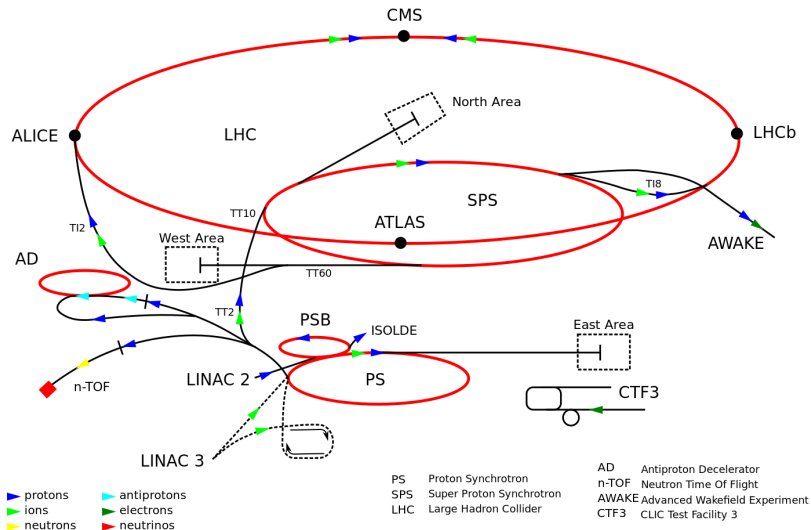


Figure 3.1: CERN accelerator complex. Blue arrows show the path followed by protons along the acceleration process [53].

912 LHC runs in three modes depending on the particles being accelerated

- 913 • Proton-Proton collisions ($p\bar{p}$) for multiple physics experiments.
 914 • Lead-Lead collisions ($Pb-Pb$) for heavy ion experiments.
 915 • Proton-Lead collisions ($p-Pb$) for quark-gluon plasma experiments.

916 In this thesis $p\bar{p}$ collisions will be considered.

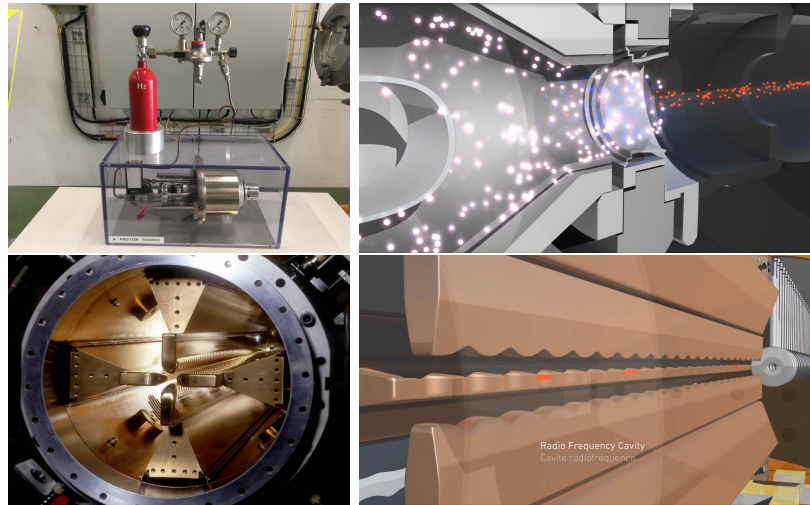


Figure 3.2: LHC protons source and the first acceleration stage. Top: the bottle contains hydrogen gas (white dots) which is injected into the metal cylinder to be broken down into electrons(blue dots) and protons(red dots); Bottom: the obtained protons are directed towards the radio frequency quadrupole which perform the first acceleration, focus the beam and create the bunches of protons. [57, 58]

918 Collection of protons starts with hydrogen atoms taken from a bottle, containing hy-
 919 drogen gas, and injecting them in a metal cylinder; hydrogen atoms are broken down
 920 into electrons and protons by an intense electric field (see figure3.2 top). The result-
 921 ing protons leave the metal cylinder towards a radio frequency quadrupole (RFQ)
 922 that focus the beam, accelerates the protons and creates the packets of protons called
 923 bunches. In the RFQ, an electric field is generated by a RF wave at a frequency that
 924 matches the resonance frequency of the cavity where the electrodes are contained.
 925 The beam of protons traveling on the RFQ axis experiences an alternating electric
 926 field gradient that generates the focusing forces.

927

928 In order to accelerate the protons, a longitudinal time-varying electric field component
 929 is added to the system; it is done by giving the electrodes a sinus-like profile as shown
 930 in figure 3.2 bottom. By matching the speed and phase of the protons with the
 931 longitudinal electric field the bunching is performed; protons synchronized with the

932 RFQ (synchronous proton) do not feel an accelerating force, but those protons in the
 933 beam that have more (or less) energy than the synchronous proton (asynchronous
 934 protons) will feel a decelerating (accelerating) force; therefore, asynchronous protons
 935 will oscillate around the synchronous ones forming bunches of protons [55]. From the
 936 RFQ protons emerge with energy 750 keV in bunches of about 1.15×10^{11} protons [56].

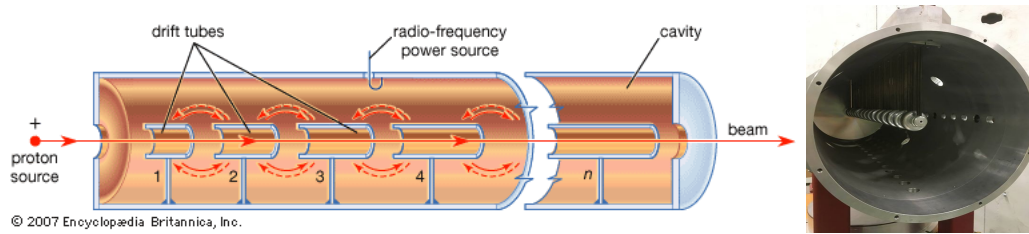


Figure 3.3: The LINAC2 accelerating system at CERN. Electric fields generated by radio frequency (RF) create acceleration and deceleration zones inside the cavity; deceleration zones are blocked by drift tubes where quadrupole magnets focus the proton beam. [59]

937 Proton bunches coming from the RFQ go to the linear accelerator 2 (LINAC2) where
 938 they are accelerated to reach 50 MeV energy. In the LINAC2 stage, acceleration
 939 is performed using electric fields generated by radio frequency which create zones
 940 of acceleration and deceleration as shown in figure 3.3. In the decelerations zones,
 941 the electric field is blocked using drift tubes where protons are free to drift while
 942 quadrupole magnets focus the beam.

943

944 The beam coming from LINAC2 is injected into the proton synchrotron booster
 945 (PSB) to reach 1.4 GeV in energy. The next acceleration is provided at the pro-
 946 ton synchrotron (PS) up to 26 GeV, followed by the injection into the super proton
 947 synchrotron (SPS) where protons are accelerated to 450 GeV. Finally, protons are
 948 injected into the LHC where they are accelerated to the target energy of 6.5 TeV.
 949 PSB, PS, SPS and LHC accelerate protons using the same RF acceleration technic
 950 described before.

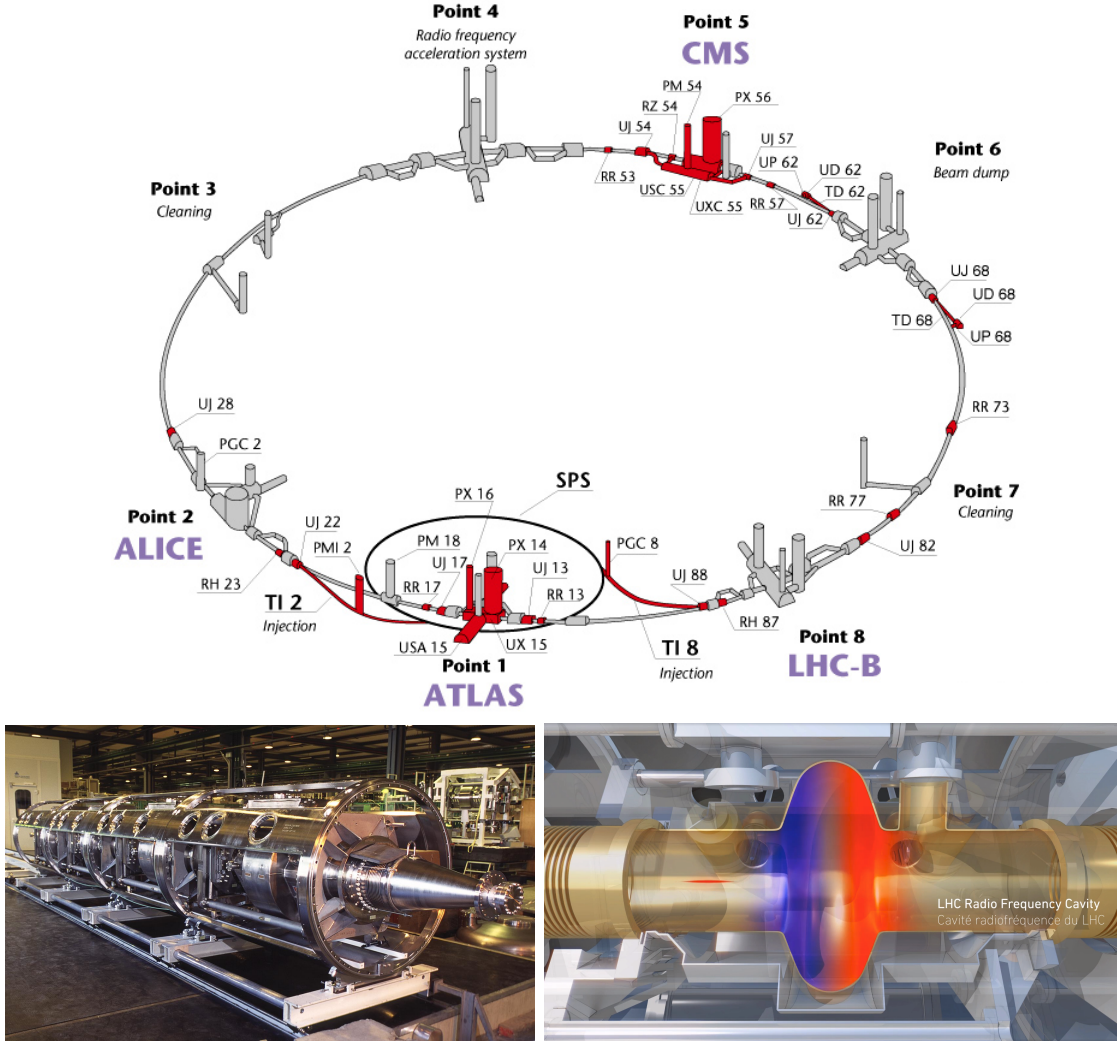


Figure 3.4: Top: LHC layout. The red zones indicate the infrastructure additions to the LEP installations, built to accomodate the ATLAS and CMS experiments which exceed the size of the former experiments located there [54]. Bottom: LHC RF cavities. A module accomodates 4 cavities that accelerate protons and preserve the bunch structure of the beam. [58, 60]

951 LHC has a system of 16 RF cavities located in the so-called point 4, as shown in
 952 figure 3.4 top, tunned at a frequency of 400 MHz and the protons are carefully timed
 953 so in addition to the acceleration effect the bunch structure of the beam is preserved.
 954 Bottom side of figure 3.4 shows a picture of a Rf module composed of 4 RF cavities
 955 working in a superconducting state at 4.5 K; also is showed a representation of the

956 accelerating electric field that accelerates the protons in the bunch.

957

958 While protons are accelerated in one section of the LHC ring, where the RF cavities
 959 are located, in the rest of their path they have to be kept in the curved trajectory
 960 defined by the LHC ring. Technically, LHC is not a perfect circle; RF, injection, beam
 961 dumping, beam cleaning and sections before and after the experimental points where
 962 protons collide are all straight sections. In total, there are 8 arcs 2.45 Km long each
 963 and 8 straight sections 545 m long each. In order to curve the proton's trajectory in
 964 the arc sections, superconducting dipole magnets are used.

965

966 Inside the LHC ring, there are two proton beams traveling in opposite directions in
 967 two separated beam pipes; the beam pipes are kept at ultra-high vacuum ($\sim 10^{-9}$
 968 Pa) to ensure that there are no particles that interact with the proton beams. The
 969 superconducting dipole magnets used in LHC are made of a NbTi alloy, capable of
 970 transporting currents of about 12000 A when cooled at a temperature below 2K using
 971 liquid helium (see figure 3.5).

972

973 Protons in the arc sections of LHC feel a centripetal force exerted by the dipole
 974 magnets which is perpendicular to the beam trajectory; The magnitude of magnetic
 975 field needed can be found assuming that protons travel at $v \approx c$, using the standard
 976 values for proton mass and charge and the LHC radius, as

$$F_m = \frac{mv^2}{r} = qBv \quad \rightarrow B = 8.33T \quad (3.1)$$

977 which is about 100000 times the Earth's magnetic field. A representation of the mag-
 978 netic field generated by the dipole magnets is shown on the bottom left side of figure

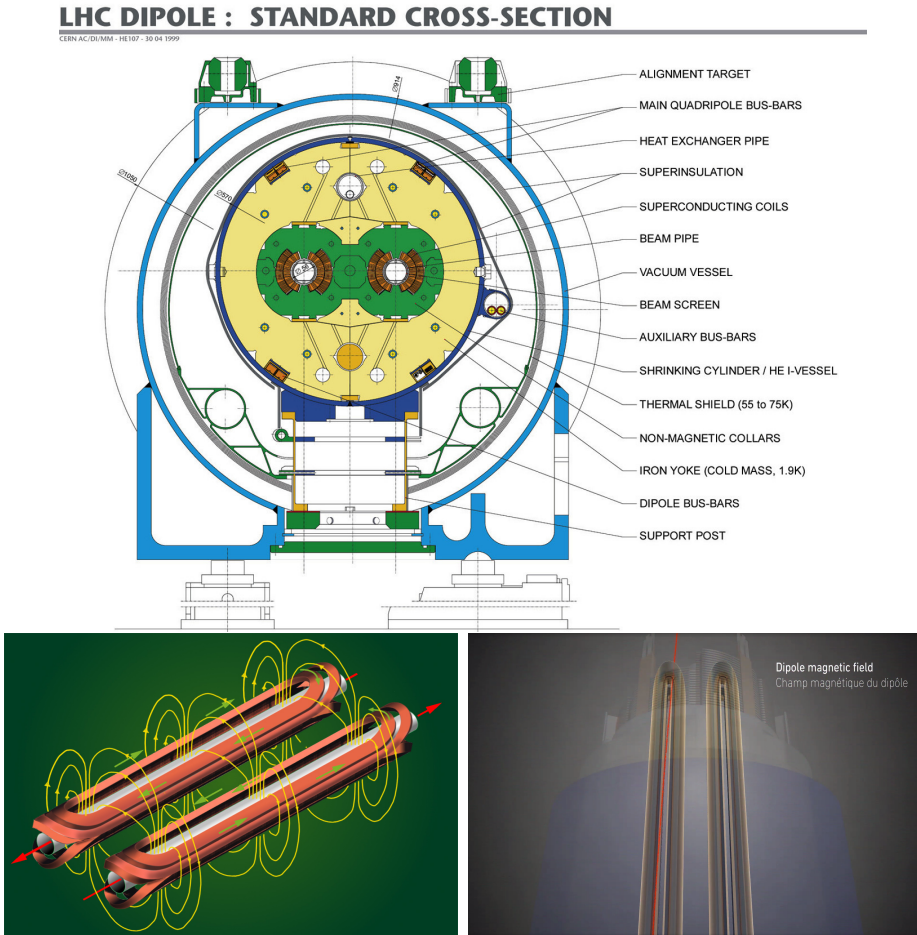


Figure 3.5: Top: LHC dipole magnet transversal view; cooling, shielding and mechanical support are indicated. Bottom left: Magnetic field generated by the dipole magnets; note that the direction of the field inside one beam pipe is opposite with respect to the other beam pipe which guarantee that both proton beams are curved in the same direction towards the center of the ring. The effect of the dipole magnetic field on the proton beam is represented on the bottom right side [58, 61, 62].

979 3.5. The bending effect of the magnetic field on the proton beam is shown on the
 980 bottom right side of figure 3.5. Note that the dipole magnets are not curved; the arc
 981 section of the LHC ring is composed of straight dipole magnets of about 15 m. In
 982 total there are 1232 dipole magnets along the LHC ring.

983

984 In addition to bending the beam trajectory, the beam has to be focused so it stays

985 inside the beam pipe. The focusing is performed by quadrupole magnets installed in
 986 a different straight section; in total 858 quadrupole magnets are installed along the
 987 LHC ring. Other effects like electromagnetic interaction among bunches, interaction
 988 with electron clouds from the beam pipe, the gravitational force on the protons, dif-
 989 ferences in energy among protons in the same bunch, among others, are corrected
 990 using sextupole and other magnetic multipoles.

991

992 The two proton beams inside the LHC ring are made of bunches with a cylindrical
 993 shape of about 7.5 cm long and about 1 mm in diameter; when bunches are close
 994 to the collision point (CP), the beam is focused up to a diameter of about 16 μm in
 995 order to maximize the number of collisions per unit area and per second, known as
 996 luminosity (L). Luminosity can be calculated using

$$L = fn \frac{N_1 N_2}{4\pi\sigma_x\sigma_y} \quad (3.2)$$

997 where f is the revolution frequency, n is the number of bunches per beam, N_1 and
 998 N_2 are the numbers of protons per bunch (1.5×10^{11}), σ_x and σ_y are the gaussian
 999 transverse sizes of the bunches. The expected luminosity about

$$f = \frac{v}{2\pi r_{LHC}} \approx \frac{3 \times 10^8 \text{ m/s}}{27 \text{ km}} \approx 11.1 \text{ kHz},$$

$$n = 2808$$

$$N_1 = N_2 = 1.5 \times 10^{11}$$

$$\sigma_x = \sigma_y = 16 \mu\text{m}$$

1000

$$L = 1.28 \times 10^{34} \text{ cm}^{-2} \text{ s}^{-1} = 1.28 \times 10^{-5} \text{ fb}^{-1} \text{ s}^{-1} \quad (3.3)$$

1001 Luminosity is a fundamental aspect of LHC given that the bigger luminosity the bigger
 1002 number of collisions, which means that for processes with a very small cross section
 1003 the number of expected occurrences is increased and so the chances of being detected.
 1004 The integrated luminosity, i.e. the total luminosity, collected by the CMS experiment
 1005 during 2016 is shown in figure 3.6; the data analyzed in this thesis corresponds to an
 1006 integrated luminosity of 35.9 fb^{-1} at a center of mass-energy $\sqrt{s} = 13 \text{ TeV}$.
 1007 A way to increase L is increasing the number of bunches in the beam. Currently, the
 1008 separation between two consecutive bunches in the beam is 7.5 m which corresponds
 1009 to a time separation of 25 ns. In the full LHC ring the allowed number of bunches is
 1010 $n = 27\text{km}/7.5\text{m} = 3600$; however, there are some gaps in the bunch pattern intended
 1011 for preparing the dumping and injection of the beam, thus, the proton beams are
 1012 composed of 2808 bunches.

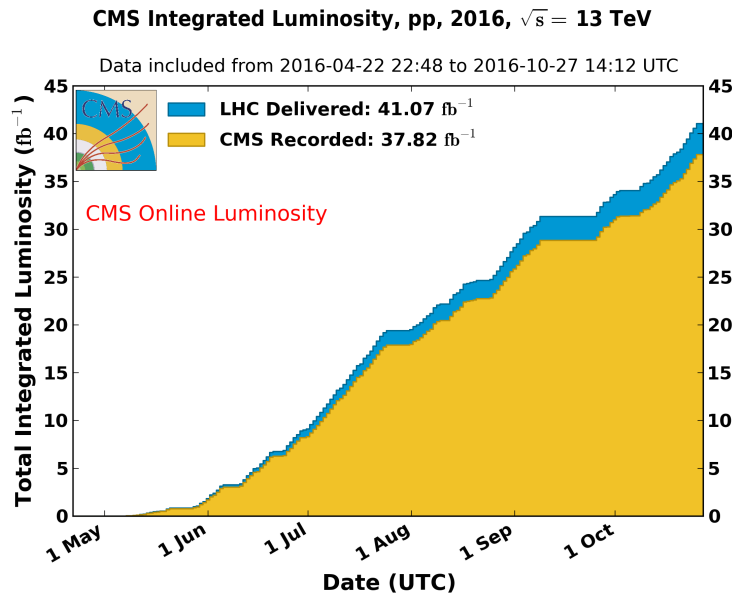


Figure 3.6: Integrated luminosity delivered by LHC and recorded by CMS during 2016. The difference between the delivered and the recorded luminosities is due to fails and issues occurred during the data taking in the CMS experiment [63].

1013 Once the proton beams reach the desired energy, they are brought to cross each other

1014 producing proton-proton collisions. The bunch crossing happens in precise places
 1015 where the four LHC experiments are located, as seen in figure 3.7 left. In 2008, the
 1016 first set of collisions involved protons with $\sqrt{s} = 7$ TeV; the energy was increased to
 1017 8 TeV in 2012 and to 13 TeV in 2015.

1018 CMS and ATLAS experiments, which are multi-purpose experiments, are enabled
 1019 to explore physics in any of the collision modes. LHCb experiment is optimized
 1020 to explore bottom quark physics, while ALICE is optimized for heavy ion collisions
 1021 searches; TOTEM and LHCf are dedicated to forward physics studies; MoEDAL (not
 1022 indicated in the figure) is intended for monopoles or massive pseudo stable particles
 1023 searches.

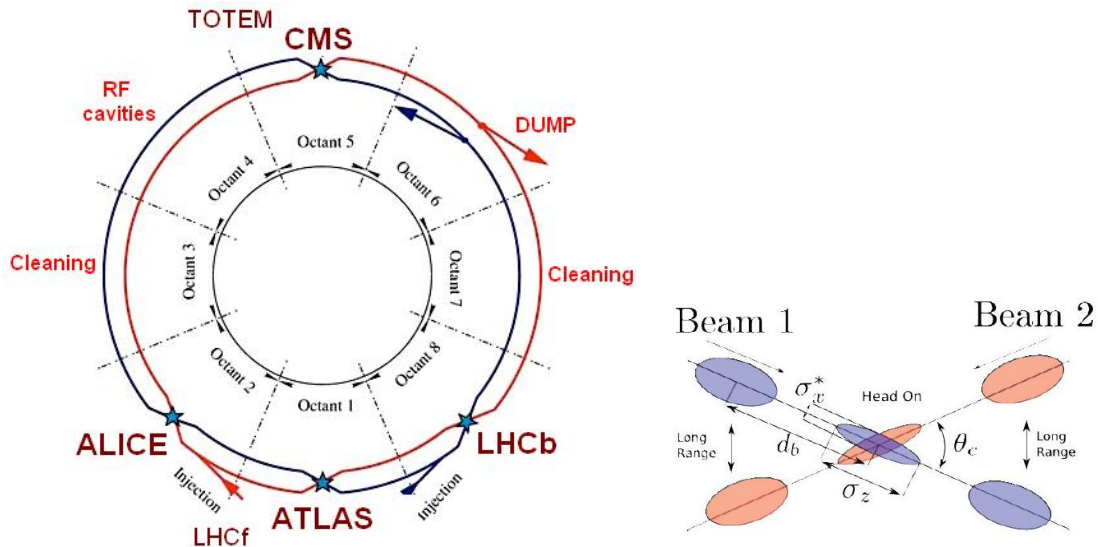


Figure 3.7: Left: LHC interaction points. Bunch crossing occurs where the LHC experiments are located [64]. Sections indicated as cleaning are dedicated to collimate the beam in order to protect the LHC ring from collisions with protons in very spreaded bunches. Right: bunch crossing scheme. Since the bunch crossing is not perfectly head-on, the luminosity is reduced in a factor of 17%.

1024 At the CP there are two interesting details that need to be addressed. The first
 1025 one is that the bunch crossing does not occur head-on but at a small crossing angle
 1026 ($280 \mu\text{rad}$ in CMS and ATLAS) as shown in the right side of figure 3.7, affecting the

1027 overlapping between bunches; the consequence is a reduction of about 17% in the
 1028 luminosity. The second one is the occurrence of multiple pp collisions in the same
 1029 bunch crossing; this effect is called pile-up (PU). A fairly simple estimation of the
 1030 PU follows from estimating the probability of collision between two protons, one from
 1031 each of the bunches in course of collision; it depends roughly on the ratio of proton
 1032 size and the cross section of the bunch in the interaction point, i.e.,

$$P(pp\text{-}collision) \sim \frac{d_{proton}^2}{\sigma_x \sigma_y} = \frac{(1\text{fm})^2}{(16\mu\text{m})^2} \sim 4 \times 10^{-21} \quad (3.4)$$

1033 however, there are $N = 1.15 \times 10^{11}$ protons in a bunch, thus the estimated number of
 1034 collisions in a bunch crossing is

$$PU = N^2 * P(pp\text{-}collision) \sim 50 \text{ pp-collision per bunch crossing}, \quad (3.5)$$

1035 about 20 of those pp collisions are inelastic. Each collision generates a vertex, but
 1036 only the most energetic is considered as a primary vertex; the rest are considered as
 1037 PU vertices. A multiple pp collision event in a bunch crossing at CMS is showed in
 1038 figure3.8. Unstable particles outgoing from the primary vertex will eventually decay;
 1039 this decay vertex is known as a secondary vertex.
 1040 Next section presents a description of the CMS detector which it is the detector used
 1041 to collect the data used in this thesis.

1042 3.3 The CMS experiment

1043 CMS is a general-purpose detector designed to conduct research in a wide range
 1044 of physics from the standard model to new physics like extra dimensions and dark

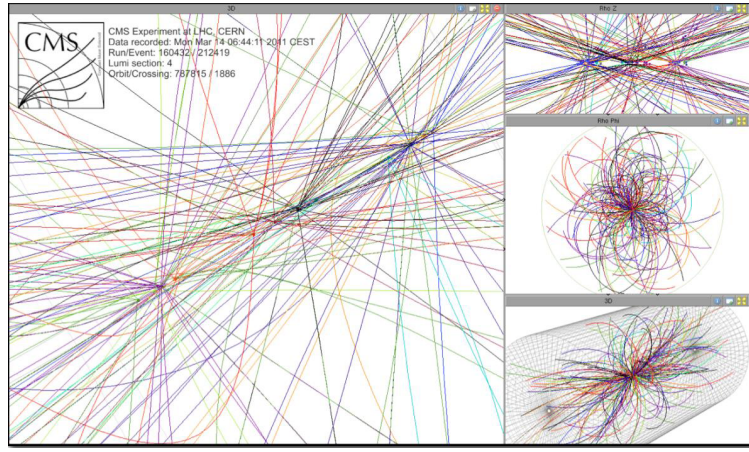


Figure 3.8: Multiple pp collision bunch crossing at CMS. Only the most energetic vertex is considered and the rets are cataloged as PU vertices [65].

matter. Located at the point 5 in the LHC layout as shown in figure 3.4, CMS is composed of several detection systems distributed in a cylindrical structure; in total, CMS weights about 12500 tons in a very compact 21.6 m long and 14.6 m diameter cylinder. It was built in 15 separate sections at the ground level and lowered to the cavern individually to be assembled. A complete and detailed description of the CMS detector and its components is given in reference [66] on which this section is based on.

1051

1052 Figure 3.9 shows the layout of the CMS detector. The design is driven by the requirements on the identification, momentum resolution and unambiguous charge determination of the muons; therefore, a large bending power is provided by the solenoid magnet made of superconducting cable capable to generate a 3.8 T magnetic field.

1055 The detection system is composed of (from the innermost to the outermost)

- 1057 ● Pixel detector.
- 1058 ● Silicon strip tracker.
- 1059 ● Preshower detector.

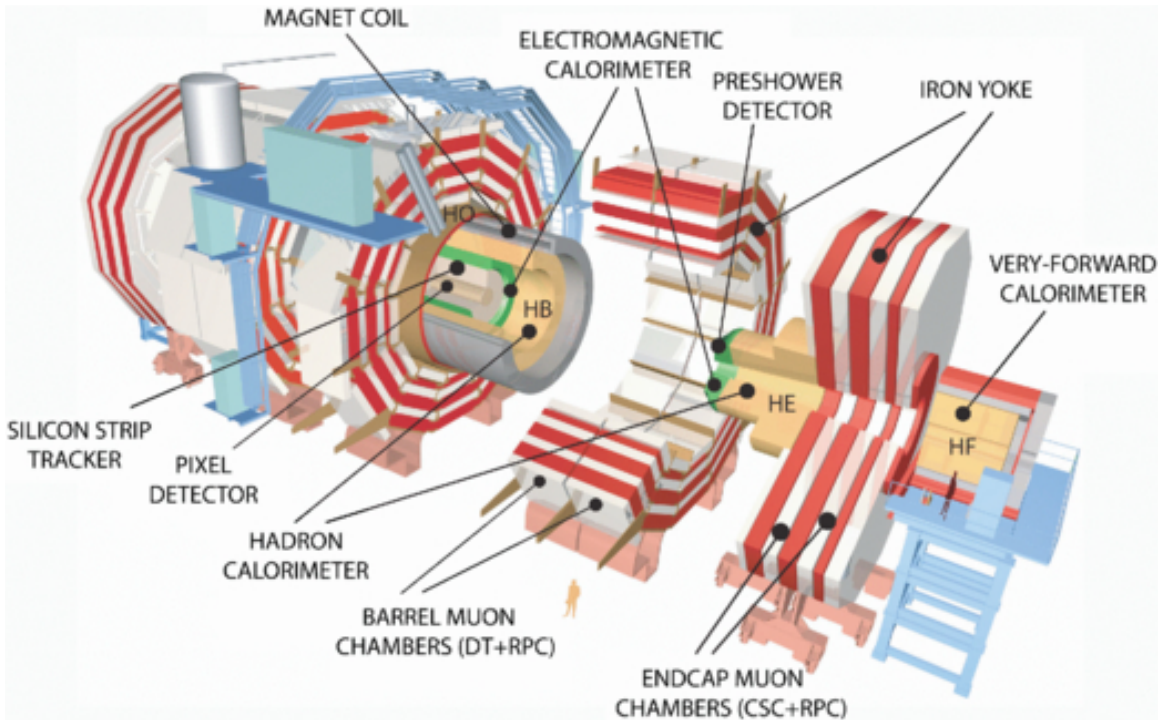


Figure 3.9: Layout of the CMS detector. The several subdetectors are indicated. The central region of the detector is referred as the Barrel section while the endcaps are referred as the forward sections. [67].

1060 • Electromagnetic calorimeter.

1061 • Hadronic calorimeter.

1062 • Muon chambers (Barrel and endcap)

1063 The central region of the detector is commonly referred as the barrel section while the
 1064 endcaps are referred as the forward sections of the detector; thus, each subdetector
 1065 is composed of a barrel section and a forward section.

1066 3.3.1 Coordinate system

1067 The coordinate system used by CMS is centered in the geometrical center of the
 1068 detector which is the same as the CP as shown in figure 3.10. The z -axis is parallel

1069 to the beam direction, while the Y -axis pointing vertically upward, and the X -axis
 1070 pointing radially inward toward the center of the LHC.

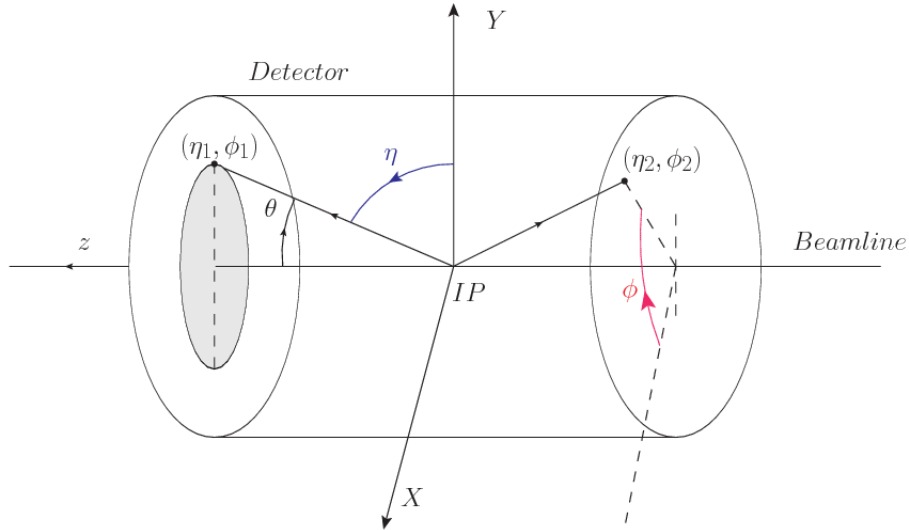


Figure 3.10: CMS detector coordinate system.

1071 In addition to the common cartesian and cylindrical coordinate systems, two coordi-
 1072 nates are of particular utility in particle physics: rapidity(y) and pseudorapidity(η),
 1073 defined in connection to the polar angle θ , energy and longitudinal momentum com-
 1074 ponent (momentum along the z -axis) according to

$$y = \frac{1}{2} \ln \frac{E + p_z}{E - p_z} \quad \eta = -\ln \left(\tan \frac{\theta}{2} \right) \quad (3.6)$$

1075 Rapidity is related to the angle between the XY -plane and the direction in which the
 1076 products of a collision are emitted; it has the nice property that the difference between
 1077 the rapidities of two particles is invariant with respect to Lorentz boosts along the z -
 1078 axis. Thus, data analysis becomes more simple when based on rapidity; however, it is
 1079 not simple to measure the rapidity of highly relativistic particles, as those produced
 1080 after pp collisions. Under the highly relativistic motion approximation, y can be
 1081 rewritten in terms of the polar angle, concluding that rapidity is approximately equal

1082 to the pseudorapidity defined above, i.e. $y \approx \eta$. Note that η is easier to measure than y
 1083 given the direct relationship between the former and the polar angle. Angular distance
 1084 between two objects in the detector (ΔR) is defined in terms of their coordinates
 1085 $(\eta_1, \phi_1), (\eta_2, \phi_2)$ as

$$\Delta R = \sqrt{(\Delta\eta)^2 - (\Delta\phi)^2} \quad (3.7)$$

1086 **3.3.2 Pixels detector**

1087 The CMS tracking system is designed to provide a precise measurement of the trajectory
 1088 followed by the charged particles created after the pp collisions; also, the precise
 1089 reconstruction of the primary and secondary vertices is expected in an environment
 1090 where, each 25 ns, the bunch crossing produce about 20 inelastic collisions and about
 1091 1000 particles. An increment in the luminosity is ongoing which implies that the PU
 1092 will increase accordingly.

1093

1094 The pixel detector was replaced during the 2016-2017 extended year-end technical
 1095 stop, due to the increasingly challenging operating conditions like the higher particle
 1096 flow and more radiation harsh environment, among others. The new one is responding
 1097 as expected, reinforcing its crucial role in the successful way to fulfill the new
 1098 LHC physics objectives after the discovery of the Higgs boson. The last chapter of
 1099 this thesis is dedicated to describe my contribution to the “Forward Pixel Phase 1
 1100 upgrade”.

1101

1102 The current pixel detector is composed of 1856 silicon pixel detector modules organized
 1103 in four-barrel layers in the central region and three disks in the forward region;
 1104 it is designed to record efficiently and with high precision, up to $10\mu\text{m}$ in the XY -

1105 plane and $20\mu\text{m}$ in the z -direction, the first four space-points near to the CP region
 1106 (see figure 3.11 left side) in the range $|\eta| \leq 2.5$. The first barrel layer is located at a
 1107 radius of 30 mm from the beamline, while the fourth layer is located at a radius of
 1108 160 mm closer to the strip tracker inner barrel layer (see section 3.3.3) in order to
 1109 reduce the rate of fake tracks. The high granularity of the detector is represented in
 1110 its about 123 Mpixels, each of size $100 \times 150\mu\text{m}^2$, which is almost twice the channels
 1111 of the old detector. The transverse momentum resolution of tracks can be measured
 1112 with a resolution of 1-2% for muons of $p_T = 100$ GeV.

1113

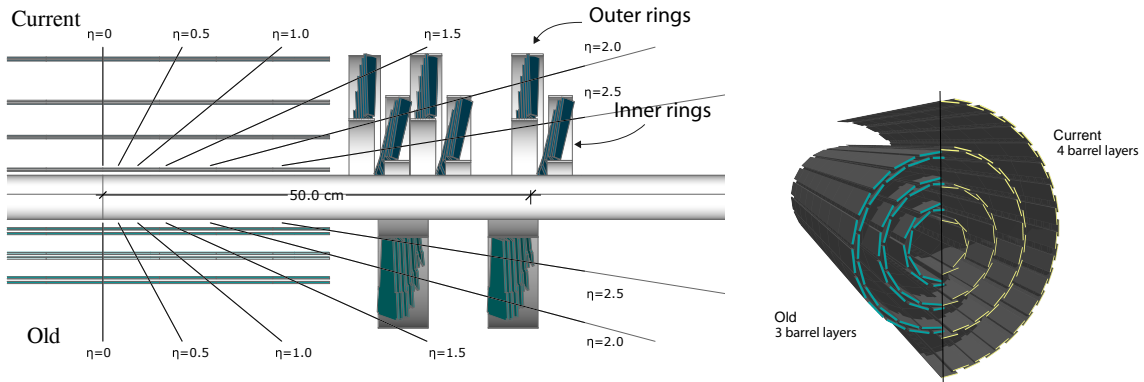


Figure 3.11: CMS pixel detector schematic view. Left: layout comparing the layers and disks in the old and current pixel detectors. Right: Transverse-oblique view comparing the pixel barrel layers in the two [69].

1114 Some of the improvements with respect to the previous pixel detector include a higher
 1115 average tracking efficiency and lower average fake rate as well as higher track impact
 1116 parameter resolution which is fundamental in order to increase the efficiency in the
 1117 identification of jets originating from b quarks (b-tagging). A significant source of
 1118 improvement comes from the overall reduction in the material budget of the detector
 1119 which results in fewer photon conversions and less multiple scattering from charged
 1120 particles.

1121 **3.3.3 Silicon strip tracker**

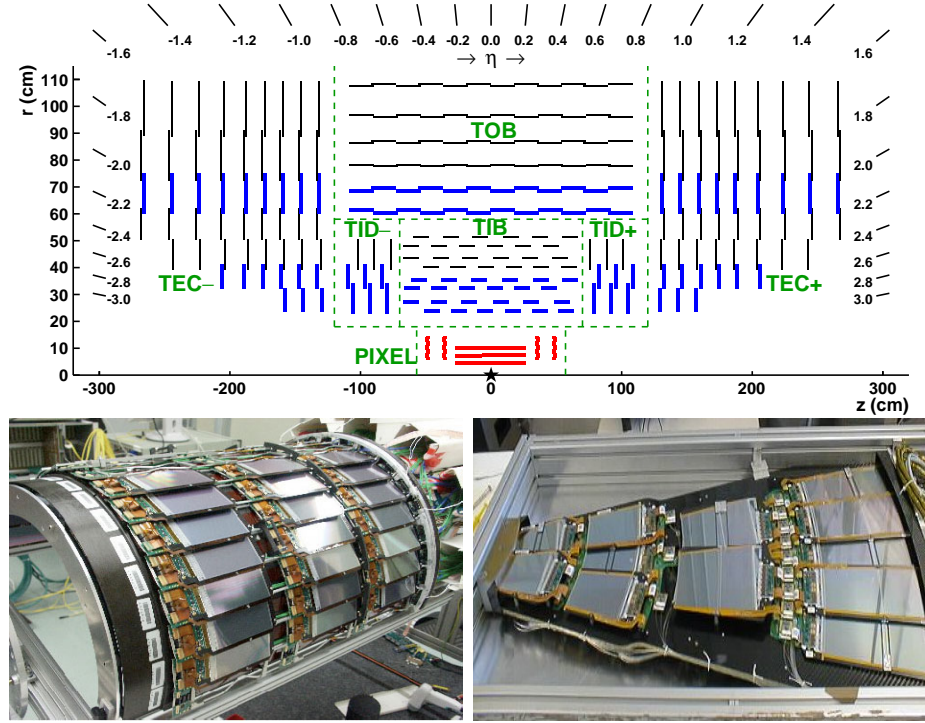


Figure 3.12: Top: CMS Silicon Strip Tracker (SST) schematic view. The SST is composed of the tracker inner barrel (TIB), the tracker inner disks (TID), the tracker outer barrel (TOB) and the tracker endcaps (TEC). Each part is made of silicon strip modules; the modules in blue represent two modules mounted back-to-back and rotated in the plane of the module by a stereo angle of 120 mrad in order to provide a 3-D reconstruction of the hit positions. Bottom: pictures of the TIB (left) and TEC (right) modules [70–72].

1122 The silicon strip tracker (SST) is the second stage in the CMS tracking system. The
 1123 top side of figure 3.12 shows a schematic of the SST. The inner tracker region is com-
 1124 posed of the tracker inner barrel (TIB) and the tracker inner disks (TID) covering the
 1125 region $r < 55$ cm and $|z| < 118$ cm. The TIB is composed of 4 layers while the TID
 1126 is composed of 3 disks at each end. The silicon sensors in the inner tracker are 320
 1127 μm thick, providing a resolution of about 13–38 μm in the $r\phi$ position measurement.
 1128

1129 The modules indicated in blue in the schematic view of figure 3.12 are two modules

1130 mounted back-to-back and rotated in the plane of the module by a “stereo” angle of
 1131 100 mrad; the hits from these two modules, known as “stereo hits”, are combined to
 1132 provide a measurement of the second coordinate (z in the barrel and r on the disks)
 1133 allowing the reconstruction of hit positions in 3-D.

1134

1135 The outer tracker region is composed of the tracker outer barrel (TOB) and the
 1136 tracker endcaps (TEC). The six layers of the TOB offer coverage in the region $r > 55$
 1137 cm and $|z| < 118$ cm, while the 9 disks of the TEC cover the region $124 < |z| < 282$
 1138 cm. The resolution offered by the outer tracker is about 13-38 μm in the $r\phi$ position
 1139 measurement. The inner four TEC disks use silicon sensors 320 μm thick; those in
 1140 the TOB and the outer three TEC disks use silicon sensors of 500 μm thickness. The
 1141 silicon strips run parallel to the z -axis and the distance between strips varies from 80
 1142 μm in the inner TIB layers to 183 μm in the inner TOB layers; in the endcaps the
 1143 wedge-shaped sensors with radial strips, whose pitch range between 81 μm at small
 1144 radii and 205 μm at large radii.

1145

1146 The whole SST has 15148 silicon modules, 9.3 million silicon strips and cover a total
 1147 active area of about 198 m^2 .

1148 3.3.4 Electromagnetic calorimeter

1149 The CMS electromagnetic calorimeter (ECAL) is designed to measure the energy of
 1150 electrons and photons. It is composed of 75848 lead tungstate crystals which have a
 1151 short radiation length (0.89 cm) and fast response, since 80% of the light is emitted
 1152 within 25 ns; however, they are combined with Avalanche photodiodes (APDs) as
 1153 photodetectors given that crystals themselves have a low light yield ($30\gamma/\text{MeV}$). A

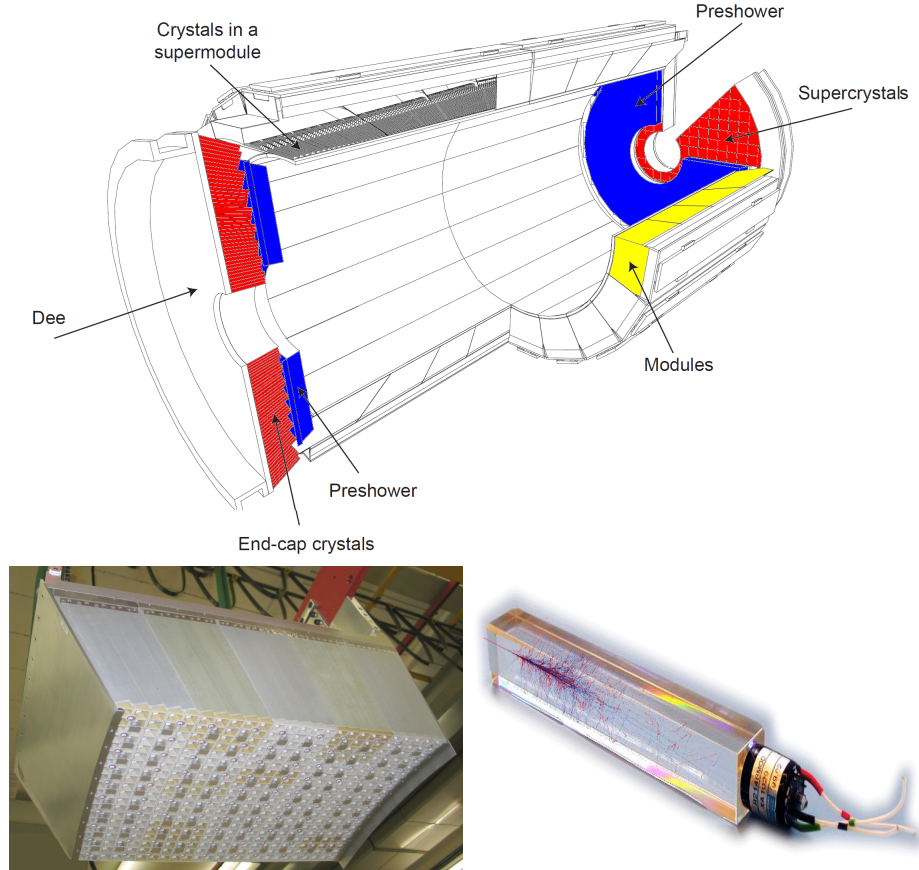


Figure 3.13: Top: CMS ECAL schematic view. Bottom: Module equipped with the crystals (left); ECAL crystal(right).

1154 schematic view of the ECAL is shown in figure 3.13.

1155

1156 Energy is measured by absorbing electrons and photons which generates an electro-
 1157 magnetic “shower”, as seen in bottom right picture of the figure3.13. The ECAL barrel
 1158 (EB) covers the region $|\eta| < 1.479$, using crystals of depth of 23 cm and $2.2 \times 2.2 \text{ cm}^2$
 1159 transverse section; the ECAL endcap (EE) covers the region $1.479 < |\eta| < 3.0$ using
 1160 crystals of depth 22 cm and transverse section of $2.86 \times 2.86 \text{ cm}^2$; the photodetectors
 1161 used are vacuum phototriodes (VPTs). Each EE is divided in two structures called
 1162 “Dees”.

1163

1164 In front of the EE, it is installed the preshower detector (ES) which covers the region
 1165 $1.653 < |\eta| < 2.6$. The ES provides a precise measurement of the position of electro-
 1166 magnetic showers, which allows to distinguish electrons and photons signals from π^0
 1167 decay signals. The ES is composed of a layer of lead absorber followed by a layer of
 1168 plastic scintillators

1169 **3.3.5 Hadronic calorimeter**

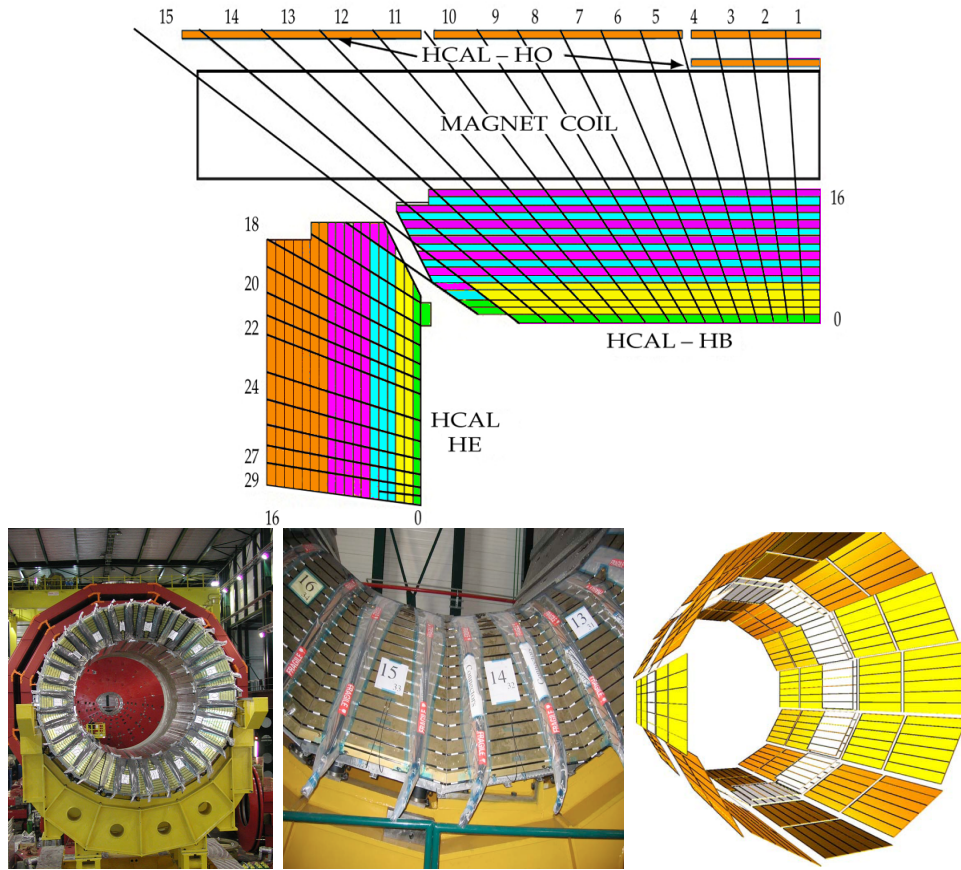


Figure 3.14: Top: CMS HCAL schematic view, the colors indicate the layers that are grouped into the same readout channels. Bottom: picture of a section of the HB; the absorber material is the golden region and scintillators are placed in between the absorber material (left and center). Schematic view of the HO (right). [73, 74]

1170 Hadrons are not absorbed by the ECAL but by the hadron calorimeter (HCAL),
 1171 which is made of a combination of alternating brass absorber layers and silicon photo-
 1172 multiplier(SiPM) layers; therefore, particles passing through the scintillator material
 1173 produce showers, as in the ECAL, as a result of the inelastic scattering of the hadrons
 1174 with the detector material. Since the particles are not absorbed in the scintillator,
 1175 their energy is sampled; therefore the total energy is not measured but estimated,
 1176 which reduce the resolution of the detector. Brass was chosen as the absorber mate-
 1177 rial due to its short interaction length ($\lambda_I = 16.42\text{cm}$) and its non-magnetivity. Figure
 1178 3.14 shows a schematic view of the CMS HCAL.

1179

1180 The HCAL is divided into four sections; the Hadron Barrel (HB), the Hadron Outer
 1181 (HO), the Hadron Endcap (HE) and the Hadron Forward (HF) sections. The HB
 1182 covers the region $0 < |\eta| < 1.4$, while the HE covers the region $1.3 < |\eta| < 3.0$. The HF,
 1183 made of quartz fiber scintillator and steel as absorption material, covers the forward
 1184 region $3.0 < |\eta| < 5.2$. Both the HB and HF are located inside the solenoid. The HO
 1185 is placed outside the magnet as an additional layer of scintillators with the purpose
 1186 of measure the energy tails of particles passing through the HB and the magnet (see
 1187 figure 3.14 top and bottom right). The upgrades made to the HCAL during the
 1188 technical stop 2016-2017 consisted in the replacement of the photo transducer, in
 1189 order to improve the efficiency.

1190 3.3.6 Superconducting solenoid magnet

1191 The superconducting magnet installed in the CMS detector is designed to provide
 1192 an intense and highly uniform magnetic field in the central part of the detector. In
 1193 fact, the tracking system takes advantage of the bending power of the magnetic field

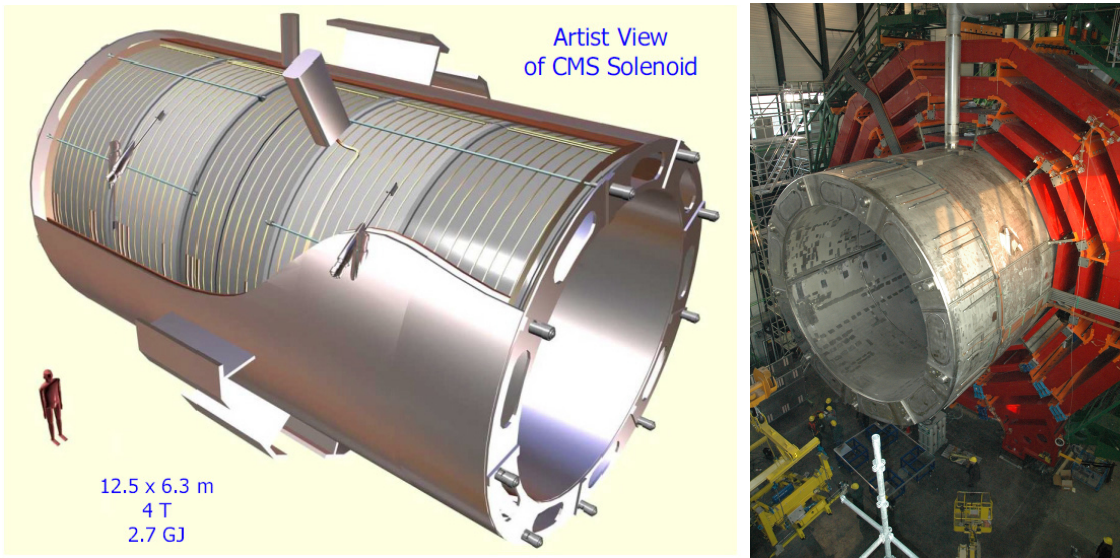


Figure 3.15: Artistic representation of the CMS solenoid magnet(left). The magnet is supported on an iron yoke (right) which also serves as the house of the muon detector and as mechanical support for the whole CMS detector [68].

1194 to measure with precision the momentum of the particles that traverse it; the unam-
 1195 biguous determination of the sign for high momentum muons was a driven principle
 1196 during the design of the magnet. The magnet has a diameter of 6.3 m, a length of 12.5
 1197 m and a cold mass of 220 t; the generated magnetic field reaches a strength of 3.8T.
 1198 Since it is made of Ni-Tb superconducting cable it has to operate at a temperature
 1199 of 4.7 K by using a helium cryogenic system; the current circulating in the cables
 1200 reaches 18800 A under normal running conditions. The left side of figure 3.15 shows
 1201 an artistic view of the CMS magnet, while the right side shows a transverse view of
 1202 the cold mass where the winding structure is visible.

1203
 1204 The yoke (see figure 3.15), composed of 5 barrel wheels and 6 endcap disks made
 1205 of iron, serves not only as the media for magnetic flux return but also provides the
 1206 house for the muon detector system and structural stability to the full detector.

1207 **3.3.7 Muon system**

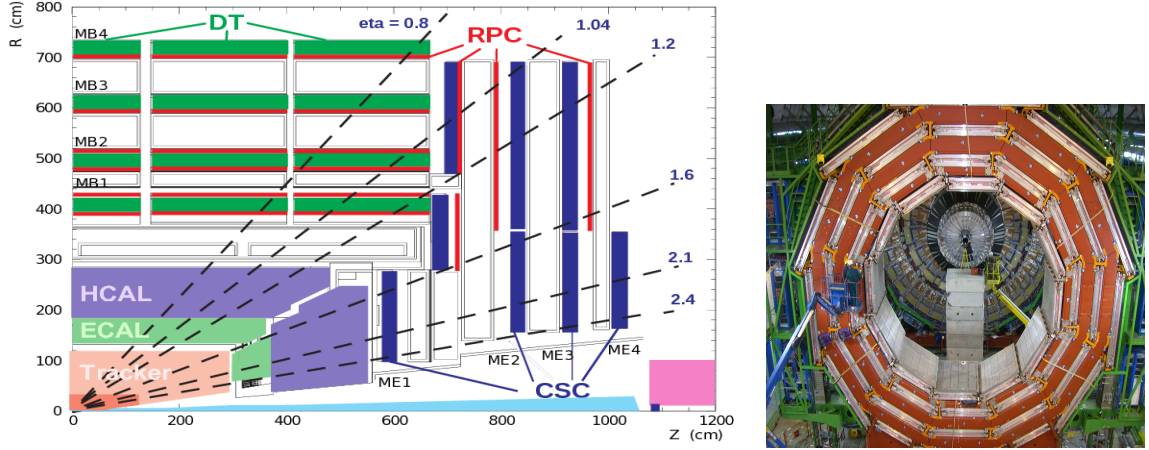


Figure 3.16: Left: CMS muon system schematic view; Right: one of the yoke rings with the muon DTs and RPCs installed; in the back it is possible to see the muon endcap [75].

1208 Muons are the only charged particles able to pass through all the CMS detector due
 1209 to their low ionization energy loss; thus, muons can be separated easily from the
 1210 high amount of particles produced in a pp collision. Also, muons are expected to be
 1211 produced in the decay of several new particles; therefore, a good detection of muons
 1212 was on the leading principles when designing the CMS detector.

1213

1214 The CMS muon detection system is embedded in the return yoke as seen in figure
 1215 3.16. It is composed of three different detector types, the drift tube chambers (DT),
 1216 Cathode strip chambers (CSC), and resistive plate chambers (RPC); DT are located
 1217 in the central region $\eta < 1.2$ arranged in four layers of drift chambers filled with an
 1218 Ar/CO₂ gas mixture.

1219

1220 The muon endcaps are made of CSCs covering the region $\eta < 2.4$ and filled with a
 1221 mixture of Ar/CO₂/CF₄. The reason behind using a different detector type lies on
 1222 the different conditions in the forward region like the high muon rate and high resid-

1223 ual magnetic field.

1224

1225 The third type of detector used in the muon system is a set of four disks of RPCs
 1226 working in avalanche mode. The RPCs provide good spatial and time resolutions.
 1227 The track of $high - p_T$ muon candidates is built combining information from the
 1228 tracking system and the signal from up to six RPCs and four DT chambers.

1229 **3.3.8 CMS trigger system**

1230 Under normal conditions, CMS expects pp collisions every 25 ns i.e. an interaction
 1231 rate of 40 MHz for which it is not possible to store the recorded data in full. In order
 1232 to handle this high event rate data, an online event selection, known as triggering, is
 1233 performed; triggering reduce the event rate to 100 Hz for storage and further offline
 1234 analysis.

1235

1236 The trigger system starts with a reduction of the event rate to 100 kHz in the so-called
 1237 “level 1 trigger (L1)”. L1 is based on dedicated programmable hardware like Field
 1238 Programmable Gate Arrays (FPGAs) and Application Specific Integrated Circuits
 1239 (ASICs), partly located in the detector itself; another portion is located in the CMS
 1240 under-ground cavern. Hit patterns information from the muon chambers and the en-
 1241 ergy deposits in the calorimeter are used to decide if an event is accepted or rejected,
 1242 according to selection requirements previously defined, which reflect the interesting
 1243 physics processes. Figure 3.17 shows the L1 trigger architecture

1244

1245 The second stage in the trigger system is called “ high-level trigger (HLT)”; events
 1246 accepted by L1 are passed to HLT in order to make an initial reconstruction of them.

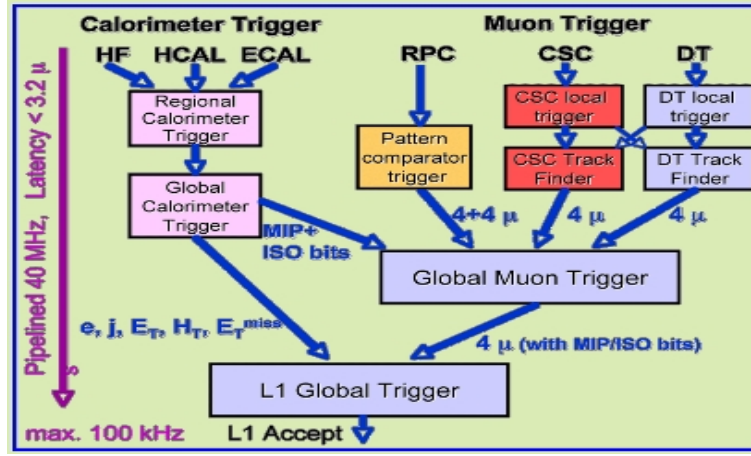


Figure 3.17: CMS Level-1 trigger architecture [76].

1247 HLT is software based and runs on a dedicated server farm, using selection algo-
 1248 rithms and high-level object definitions; the event rate at HLT is reduced to 100 Hz.

1249 The first HLT stage takes information from the muon detectors and the calorimeters
 1250 to make the initial object reconstruction; in the next HLT stage, information from
 1251 the pixel and strip detectors is used to do first fast-tracking and then full tracking
 1252 online. This initial object reconstruction is used in further steps of the trigger system.

1253

1254 Events and preliminary reconstructed physics objects from HLT are sent to be fully
 1255 reconstructed at the CERN computing center. Again, the pixel detector information
 1256 provides high-quality seeds for the track reconstruction algorithm offline, primary ver-
 1257 tex reconstruction, electron and photon identification, muon reconstruction, τ iden-
 1258 tification, and b-tagging. After full reconstruction, data sets are made available for
 1259 offline analyses.

1260

1261 During the 2016-2017 technical stop, the L1 system was updated in order to improve
 1262 the physics object identification by improving the algorithms and accounting for the
 1263 increasing pile-up scenario.

1264 3.3.9 CMS computing

1265 After the data, coming from the experiment, are processed at several levels, they have
 1266 to be stored and made available for further analysis; in order to cope all the tasks
 1267 implied in the offline data processing, like transfer, simulation, reconstruction and
 1268 reprocessing, among others, a big computing power is required. The CMS computing
 1269 system is based on the distributed architecture concept, where users of the system
 1270 and physical computer centers are distributed worldwide and interconnected by high-
 1271 speed networks.

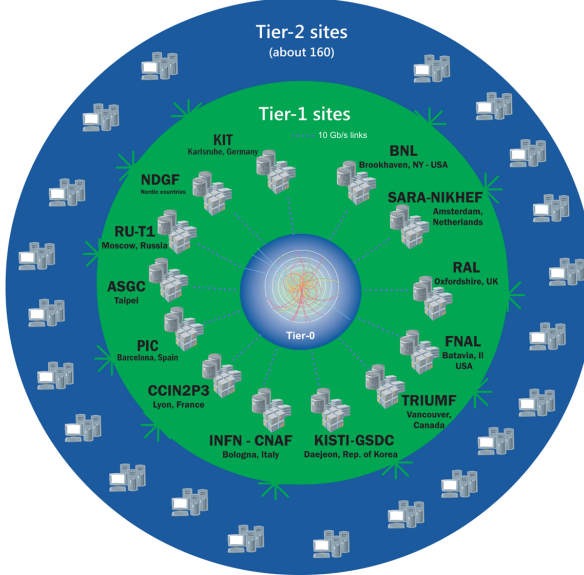


Figure 3.18: WLCG structure. The primary computer centers (Tier-0) are located at CERN (data center) and at the Wigner datacenter in Budapest. Tier-1 is composed of 13 centers and Tier-2 is composed of about 160 centers. [77].

1272 The worldwide LHC computing grid (WLCG) is the mechanism used to provide that
 1273 distributed environment. WLCG is a tiered structure connecting computing centers
 1274 around the world, which provides the necessary storage and computing facilities. The
 1275 primary computing centers of the WLCG are located at the CERN and the Wigner
 1276 datacenter in Budapest and are known as Tier-0 as shown in figure 3.18. The main

1277 responsibilities for each tier level are [77]

1278 • **Tier-0:** initial reconstruction of recorded events and storage of the resulting
1279 datasets, the distribution of raw data to the Tier-1 centers.

1280 • **Tier-1:** provide storage capacity, support for the Grid, safe-keeping of a pro-
1281 portional share of raw and reconstructed data, large-scale reprocessing and safe-
1282 keeping of corresponding output, generation of simulated events, distribution
1283 of data to Tier 2s, safe-keeping of a share of simulated data produced at these
1284 Tier 2s.

1285 • **Tier-2:** store sufficient data and provide adequate computing power for specific
1286 analysis tasks, provide analysis requirements and proportional share of simu-
1287 lated event production and reconstruction.

1288 Aside from the general computing strategy to manage the huge amount of data pro-
1289 duced by experiments, CMS uses a framework to perform a variety of processing,
1290 selection and analysis tasks. The central concept of the CMS data model is the
1291 “Event”; therefore, an event is the unit that contains the information from a single
1292 bunch crossing as well as any data derived from that information like the recon-
1293 structed objects, the details under which additional data are derived.

1294

1295 Events are passed as the input to the “physics modules” that obtain information from
1296 them and create new one; for instance, “event data producers” add new data into the
1297 events, “analyzers” produce an information summary from an event set, “filters” per-
1298 form selection and triggering.

1299

1300 CMS uses several event formats with different levels of detail and precision

- 1301 • **Raw format:** events in this format contain the full recorded information from
1302 the detector as well as trigger decision and other metadata. An extended version
1303 of raw data is used to store information from the CMS Monte Carlo simulation
1304 tools. Raw data are stored permanently, occupying about 2MB/event
- 1305 • **RECO format:** events in this format correspond to raw data that have been
1306 submitted to reconstruction algorithms like primary and secondary vertex re-
1307 construction, particle ID, track-finding. RECO events contain physical objects
1308 and all the information used to reconstruct them; average size is about 0.5
1309 MB/event.
- 1310 • **AOD format:** Analysis Object Data (AOD) is the data format used in the
1311 physics analyses given that it contains the parameters describing the high-level
1312 physics objects in addition to enough information to allow a kinematic refitting if
1313 needed. AOD events are filtered versions of the RECO events to which skimming
1314 or other kind processes have been applied. Requires about 100 kB/event.
- 1315 • **Non-event data** are data needed to interpret and reconstruct events. Some
1316 of the non-event data used by CMS contains information about the detector
1317 contraction and condition data like calibrations, alignment, and detector status.
- 1318 Figure 3.19 shows the data flow scheme between CMS detector and hardware tiers.

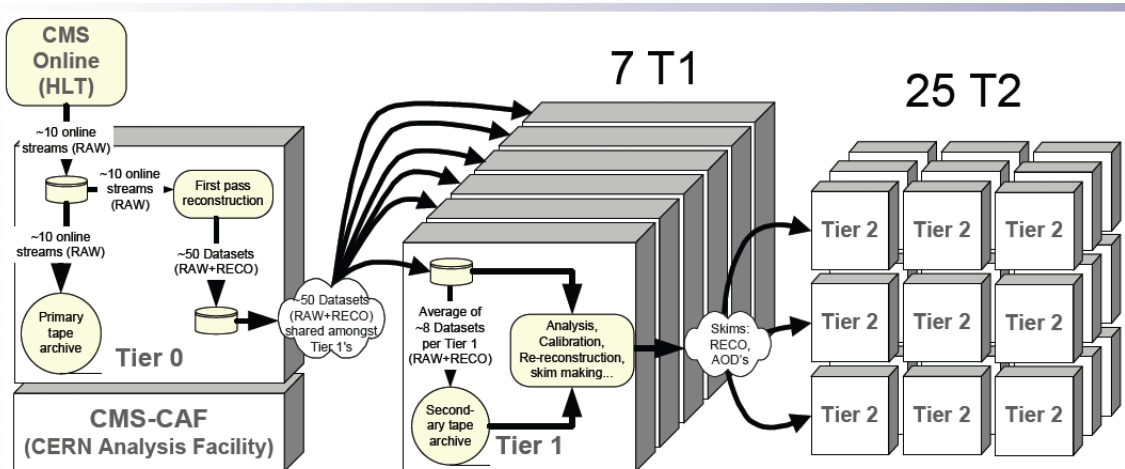


Figure 3.19: Data flow from CMS detector through hardware Tiers.

1319 **Chapter 4**

1320 **Event generation, simulation and**
1321 **reconstruction**

1322 The process of analizing the data recorded by the CMS experiment involves several
1323 stages where the data are processed in order to interpret the information provided by
1324 all the detection systems; in those stages the particles produced after the pp collision
1325 are identified by reconstructing their trajectories and measuring their features. In
1326 addition, the SM provides a set of predictions that have to be compared with the
1327 experimental results; however, in most of the cases, theoretical predictions are not
1328 directly comparable to experimental results due to the diverse source of uncertainties
1329 introduced by the experimental setup and theoretical approximations among others.

1330

1331 The strategy to face these conditions consist in using statistical methods implemented
1332 in computational algorithms to produce numerical results that can be contrasted with
1333 the experimental results. These computational algorithms are commonly known as
1334 Monte Carlo methods and, in the case of particle physics, they are designed to apply
1335 the SM rules and produce predictions about the physical observables measured in the

1336 experiments. Since particle physics is governed by quantum mechanics principles,
 1337 predictions are not allowed for single events; therefore, a high number of events are
 1338 “generated” and predictions are produced in the form of statistical distributions for
 1339 the observables. Effects of the detector presence are included in the predictions by
 1340 introducing simulations of the detector itself.

1341

1342 This chapter presents a description of the event generation strategy and the tools
 1343 used to perform the detector simulation and physics objects reconstruction. A com-
 1344 prehensive review on event generator for LHC physics can be found in reference [78].

1345 4.1 Event generation

1346 The event generation is intended to create events that mimic the behavior of actual
 1347 events produced in the collisions; they obey a sequence of steps from the particles col-
 1348 lision hard process to the decay process into the final state particles. Figure ?? shows
 1349 a schematic view of the event generation process.; the fact that the full process can
 1350 be treated as several independent steps is based on the QCD factorization theorem.

1351

1352 Generation starts by taking into account the PDFs of the incoming particles. Event
 1353 generators offer the option to choose from several PDF sets depending on the partic-
 1354 ular process under simulation¹. The *hard subprocess* describes the actual interaction
 1355 between partons from the incoming particles; it is represented by the matrix element
 1356 connecting the initial and final states of the interaction. Normally, the matrix el-
 1357 ement can be written as a sum over Feynman diagrams and consider interferences
 1358 between terms in the summation. During the generation of the hard subprocess, the

¹ Reference [79] allows to plot different PDF sets under customizable conditions.

1359 production cross section is calculated.

1360 The order to which the cross section is calculated depends on the order of the Feyn-
 1361 man diagrams involved in the calculation; therefore, radiative corrections are included
 1362 by considering a higher order Feynman diagrams where QCD radiation dominates.
 1363 Currently, cross sections calculated to LO do not offer a satisfactory description of the
 1364 processes, i.e., the results are only reliable for the shape of distributions; therefore,
 1365 NLO calculations have to be performed with the implication that the computing time
 1366 needed is highly increased.

1367

1368 The final parton content of the hard subprocess is subjected to the *parton shower*
 1369 which generates the gluon radiation. Parton shower evolves the partons; i.e., gluons
 1370 split into quark-antiquark pairs and quarks of enough energy radiates gluons giv-
 1371 ing rise to further parton multiplication, following the DGLAP (Dokshitzer-Gribov-
 1372 Lipatov-Altarelli-Parisi) equations. Showering continues until the energy scale is low
 1373 enough to reach the non-perturbative limit.

1374 In the simulation LHC processes that involve b quarks, like the single top quark or
 1375 higgs associated production, it is needed to consider that the b quark is heavier than
 1376 the proton; in this sense, the QCD interaction description is made in two different
 1377 schemes [80]

- 1378 • four-flavor (4F) scheme. b quarks appears only in the final state because they
 1379 are heavier than the proton and therefore they can be produced only from the
 1380 splitting of a gluon into pairs or singly in association with a t quark in high
 1381 energy-scale interactions. During the simulation, the b -PDFs are set to zero
 1382 because it cannot be part of the proton. Calculation in this scheme are more
 1383 complicated due to the presence of the second b quark but the full kinematics is

1384 considered already at LO and therefore the accuracy of the description is better.

1385 • five-flavor (5F) scheme. b quarks are considered massless, therefore they can
 1386 appear in both initial and final states since it can now be part of the proton; thus,
 1387 during the simulation b -PDFs are not set to zero. In this scheme, calculations are
 1388 simpler than in the 4F scheme and possible logarithmic divergences are absorbed
 1389 by the PDFs through the DGLAP evolution.

1390 The next step in the generation process is called “hadronization”. Since particles with
 1391 a net color charge are not allowed to exits isolated, they have recombine to form bound
 1392 states. This is precisely the process by which the partons resulting from the parton
 1393 shower arrange themselves as color singlet to form hadrons. At this step, the energy-
 1394 scale is too low, the strong coupling constant is large, therefore hadronization process
 1395 is non-perturbative. Most of the baryons and mesons produced in the hadronization
 1396 are unstable and hence they will decay in the detector. The decay of those unstable
 1397 particles is also simulated in the hadronization step, based on the known branching
 1398 ratios.

1399 In the general context of QCD studies, the term “hadronization” has been
 1400 used with somewhat different meanings. In the present context it refers to the specific
 1401 model used in an event generator for the transition from the partonic “final” state
 1402 to a complete representation of the actual hadronic final state. We should
 1403 emphasize that this is a transition for which we still have only models, albeit inspired
 1404 by QCD, because the only available rigorous approach to non-perturbative hadronic
 1405 phenomena, lattice QCD, is formulated in Euclidean space-time and therefore cannot
 1406 deal with inherently Minkowskian processes like the time-evolution of partons into
 1407 hadrons. Other “hadronization” meanings exist. When quantities that are
 1408 calculable within perturbative QCD, for example hadronic event shapes in $e + e \rightarrow$

1409 annihilation, are compared with experimental data, there are discrepancies that are
 1410 commonly ascribed to “hadronization corrections”. They are often estimated
 1411 and corrected for by comparing the hadron-level prediction of an event generator
 1412 with a parton-level result computed at the end of parton showering.¹³ However,
 1413 such a parton-level quantity is not really comparable to the result of a perturbative
 1414 calculation, certainly not at fixed order, nor even when resummed to all orders, as
 1415 the shower result depends on the scale and details of the cutoff that terminates it.
 1416 The origin of the discrepancies is instead generic non-perturbative contributions that
 1417 do not depend

1418 Finally, the underlying structure of the event is generated: beam remnants, inter-
 1419 actions from other partons in the hadrons, and collisions between other hadrons in
 1420 the colliding beams (called pile-up).

1421 **4.2 underlying events and pileup**

1422 **4.3 MC - MadEvent, MadGraph and** 1423 **madgraphNLO, powheg, pythia, tauola**

1424 **4.4 detector simulation**

1425 Monte Carlo Event samples will be generated to simulate the underlying physics
 1426 collision.

1427 The resulting particles will be tracked through the CMS detector and the elec-
 1428 tronics and trigger responses will be simulated.

1429 Both full and parametrized (fast) simulations will be required.

1430 We anticipate using the full simulation package, OSCAR [4, 5], for most of these
 1431 events.

1432 Fully simulated refers to detailed detector simulation based on GEANT4 [6], as
 1433 opposed to faster parametrized simulations. CMS has developed a fast simulation
 1434 package, FAMOS [7], that may be used where much larger statistics are required.

1435 Fully simulated Monte Carlo samples of approximately the same total size as the
 1436 raw data sample (1.5×10^9 events per year) must be generated, fully simulated,
 1437 reconstructed and passed through HLT selection code. The simulated pp event size
 1438 is approximately 2 MByte/event.

1439 We currently estimate that we will require the same order of magnitude of sim-
 1440 ulated events as actual data. If the Monte Carlo requirements greatly exceed this
 1441 rough real data-sample equality, then more recourse to FAMOS will be necessary.
 1442 Clearly there are very large uncertainties on the total amount of full and fast Monte
 1443 Carlo which is required, so ultimately the reality of available resources will constrain
 1444 the upper limit.

1445 **4.5 event reconstruction- particle flow algorithm,** 1446 **vertexing , muon reco, electron reco, photon** 1447 **and hadron reco, jets reco, anti-kt algoritm,** 1448 **jet energy corrections, btagging, MET**

1449 CMS requires an offline first-pass full reconstruction of express line and all online
 1450 streams in quasi-realtime, which produces new reconstructed objects called RECO
 1451 data.

1452 The Tier-0 offline reconstruction step processes all RAW events from the online
1453 system following an adjustable set of priorities (the express-line, by definition has
1454 very high priority). This step creates new higher-level physics objects such as tracks,
1455 vertices, and jets. These may improve or extend the set produced in the HLT pro-
1456 cessing step. It must run with minimal delay compared to the online in order to
1457 provide rapid feedback to the online operations, for example, identifying detector or
1458 trigger problems which can then be rectified dynamically during the same LHC fill.
1459 The offline reconstruction will normally perform the same reconstruction steps for
1460 each stream, with the possible exception of specialised calibration streams. In this
1461 way we ensure that they are all useful in principle for all analysis groups. We apply
1462 this same rule to later re-processings of the data, 2-3 times per year we expect to
1463 bring all datasets into consistent status as to applied calibrations and algorithms, as
1464 described below.

¹⁴⁶⁵ **4.6 MVA methods, NN, BDT, boosting,**

¹⁴⁶⁶ **overtraining, variable ranking**

¹⁴⁶⁷ **4.7 statistical inference, likelihood**

¹⁴⁶⁸ **parametrization**

¹⁴⁶⁹ **4.8 nuisance paraeters**

¹⁴⁷⁰ **4.9 exclusion limits**

¹⁴⁷¹ **4.10 asymptotic limits**

¹⁴⁷² References

- ¹⁴⁷³ [1] J. Schwinger. "Quantum Electrodynamics. I. A Covariant Formulation". Physical Review. 74 (10): 1439-61, (1948).
- ¹⁴⁷⁵ [2] R. P. Feynman. "Space-Time Approach to Quantum Electrodynamics". Physical Review. 76 (6): 769-89, (1949).
- ¹⁴⁷⁷ [3] S. Tomonaga. "On a Relativistically Invariant Formulation of the Quantum Theory of Wave Fields". Progress of Theoretical Physics. 1 (2): 27-42, (1946).
- ¹⁴⁷⁹ [4] D.J. Griffiths, "Introduction to electrodynamics". 4th ed. Pearson, (2013).
- ¹⁴⁸⁰ [5] F. Mandl, G. Shaw. "Quantum field theory." Chichester: Wiley (2009).
- ¹⁴⁸¹ [6] F. Halzen, and A.D. Martin, "Quarks and leptons: An introductory course in modern particle physics". New York: Wiley, (1984) .
- ¹⁴⁸³ [7] File: Standard_Model_of_Elementary_Particle_dark.svg. (2017, June 12) Wikimedia Commons, the free media repository. Retrieved November 27, 2017 from <https://www.collegiate-advanced-electricity.com/single-post/2017/04/10/The-Standard-Model-of-Particle-Physics>.
- ¹⁴⁸⁷ [8] E. Noether, "Invariante Variationsprobleme", Nachrichten von der Gesellschaft der Wissenschaften zu Göttingen, mathematisch-physikalische Klasse, vol. 1918, pp. 235-257, (1918).

- 1490 [9] C. Patrignani et al. (Particle Data Group), Chin. Phys. C, 40, 100001 (2016)
1491 and 2017 update.
- 1492 [10] M. Goldhaber, L. Grodzins, A.W. Sunyar “Helicity of Neutrinos”, Phys. Rev.
1493 109, 1015 (1958).
- 1494 [11] Palanque-Delabrouille N et al. “Neutrino masses and cosmology with Lyman-
1495 alpha forest power spectrum”, JCAP 11 011 (2015).
- 1496 [12] M. Gell-Mann. “A Schematic Model of Baryons and Mesons”. Physics Letters.
1497 8 (3): 214-215 (1964).
- 1498 [13] G. Zweig. “An SU(3) Model for Strong Interaction Symmetry and its Breaking”
1499 (PDF). CERN Report No.8182/TH.401 (1964).
- 1500 [14] G. Zweig. “An SU(3) Model for Strong Interaction Symmetry and its Breaking:
1501 II” (PDF). CERN Report No.8419/TH.412(1964).
- 1502 [15] M. Gell-Mann. “The Interpretation of the New Particles as Displaced Charged
1503 Multiplets”. Il Nuovo Cimento 4: 848. (1956).
- 1504 [16] T. Nakano, K, Nishijima. “Charge Independence for V-particles”. Progress of
1505 Theoretical Physics 10 (5): 581-582. (1953).
- 1506 [17] N. Cabibbo, “Unitary symmetry and leptonic decays” Physical Review Letters,
1507 vol. 10, no. 12, p. 531, (1963).
- 1508 [18] M.Kobayashi, T.Maskawa, “CP-violation in the renormalizable theory of weak
1509 interaction,” Progress of Theoretical Physics, vol. 49, no. 2, pp. 652-657, (1973).
- 1510 [19] File: Weak Decay (flipped).svg. (2017, June 12). Wikimedia Commons,
1511 the free media repository. Retrieved November 27, 2017 from

- 1512 https://commons.wikimedia.org/w/index.php?title=File:Weak_Decay_(flipped)
1513 .svg&oldid=247498592.
- 1514 [20] Georgia Tech University. Coupling Constants for the Fundamental
1515 Forces(2005). Retrieved January 10, 2018, from http://hyperphysics.phy-
1516 astr.gsu.edu/hbase/Forces/couple.html#c2
- 1517 [21] M. Strassler. (May 31, 2013).The Strengths of the Known Forces. Retrieved Jan-
1518 uary 10, 2018, from https://profmattstrassler.com/articles-and-posts/particle-
1519 physics-basics/the-known-forces-of-nature/the-strength-of-the-known-forces/
- 1520 [22] S.L. Glashow. “Partial symmetries of weak interactions”, Nucl. Phys. 22 579-
1521 588, (1961).
- 1522 [23] A. Salam, J.C. Ward. “Electromagnetic and weak interactions”, Physics Letters
1523 13 168-171, (1964).
- 1524 [24] S. Weinberg, “A model of leptons”, Physical Review Letters, vol. 19, no. 21, p.
1525 1264, (1967).
- 1526 [25] M. Peskin, D. Schroeder, “An introduction to quantum field theory”. Perseus
1527 Books Publishing L.L.C., (1995).
- 1528 [26] A. Pich. “The Standard Model of Electroweak Interactions”
1529 https://arxiv.org/abs/1201.0537
- 1530 [27] F.Bellaiche. (2012, 2 September). “What’s this Higgs boson anyway?”. Retrieved
1531 from: https://www.quantum-bits.org/?p=233
- 1532 [28] M. Endres et al. Nature 487, 454-458 (2012) doi:10.1038/nature11255

- 1533 [29] F. Englert, R. Brout. “Broken Symmetry and the Mass of Gauge
 1534 Vector Mesons”. Physical Review Letters. 13 (9): 321-23.(1964)
 1535 doi:10.1103/PhysRevLett.13.321
- 1536 [30] P.Higgs. “Broken Symmetries and the Masses of Gauge Bosons”. Physical Re-
 1537 view Letters. 13 (16): 508-509,(1964). doi:10.1103/PhysRevLett.13.508.
- 1538 [31] G.Guralnik, C.R. Hagen and T.W.B. Kibble. “Global Conservation Laws
 1539 and Massless Particles”. Physical Review Letters. 13 (20): 585-587, (1964).
 1540 doi:10.1103/PhysRevLett.13.585.
- 1541 [32] CMS collaboration. “Observation of a new boson at a mass of 125 GeV with
 1542 the CMS experiment at the LHC”. Physics Letters B. 716 (1): 30-61 (2012).
 1543 arXiv:1207.7235. doi:10.1016/j.physletb.2012.08.021
- 1544 [33] ATLAS collaboration. “Observation of a New Particle in the Search for the Stan-
 1545 dard Model Higgs Boson with the ATLAS Detector at the LHC”. Physics Letters
 1546 B. 716 (1): 1-29 (2012). arXiv:1207.7214. doi:10.1016/j.physletb.2012.08.020.
- 1547 [34] ATLAS collaboration; CMS collaboration (26 March 2015). “Combined Mea-
 1548 surement of the Higgs Boson Mass in pp Collisions at $\sqrt{s}=7$ and 8 TeV with
 1549 the ATLAS and CMS Experiments”. Physical Review Letters. 114 (19): 191803.
 1550 arXiv:1503.07589. doi:10.1103/PhysRevLett.114.191803.
- 1551 [35] LHC InternationalMasterclasses“When protons collide”. Retrieved from
 1552 http://atlas.physicsmasterclasses.org/en/zpath_protoncollisions.htm
- 1553 [36] CMS Collaboration, “SM Higgs Branching Ratios and To-
 1554 tal Decay Widths (up-date in CERN Report4 2016)”).

- 1555 https://twiki.cern.ch/twiki/bin/view/LHCPhysics/CERNYellowReportPageBR
 1556 , last accessed on 17.12.2017.
- 1557 [37] R.Grant V. “Determination of Higgs branching ratios in $H \rightarrow W^+W^- \rightarrow l\nu jj$ and $H \rightarrow ZZ \rightarrow l^+l^-jj$ channels”. Physics Department, University of Tennessee (Dated: October 31, 2012). Retrieved from http://aesop.phys.utk.edu/ph611/2012/projects/Riley.pdf
- 1561 [38] LHC Higgs Cross Section Working Group, Denner, A., Heinemeyer, S. et al.
 1562 “Standard model Higgs-boson branching ratios with uncertainties”. Eur. Phys.
 1563 J. C (2011) 71: 1753. <https://doi.org/10.1140/epjc/s10052-011-1753-8>
- 1564 [39] F. Maltoni, K. Paul, T. Stelzer, and S. Willenbrock, “Associated production
 1565 of Higgs and single top at hadron colliders”, Phys.Rev. D64 (2001) 094023,
 1566 [hep-ph/0106293].
- 1567 [40] S. Biswas, E. Gabrielli, F. Margaroli, and B. Mele, “Direct constraints on the
 1568 top-Higgs coupling from the 8 TeV LHC data,” Journal of High Energy Physics,
 1569 vol. 07, p. 073, (2013).
- 1570 [41] M. Farina, C. Grojean, F. Maltoni, E. Salvioni, and A. Thamm, “Lifting de-
 1571 generacies in Higgs couplings using single top production in association with a
 1572 Higgs boson,” Journal of High Energy Physics, vol. 05, p. 022, (2013).
- 1573 [42] T.M. Tait and C.-P. Yuan, “Single top quark production as a window to physics
 1574 beyond the standard model”, Phys. Rev. D 63 (2000) 014018 [hep-ph/0007298].
- 1575 [43] F. Demartin, F. Maltoni, K. Mawatari, and M. Zaro, “Higgs production in
 1576 association with a single top quark at the LHC,” European Physical Journal C,
 1577 vol. 75, p. 267, (2015).

- 1578 [44] CMS Collaboration, “Modelling of the single top-quark pro-
 1579 duction in association with the Higgs boson at 13 TeV.”
 1580 <https://twiki.cern.ch/twiki/bin/viewauth/CMS/SingleTopHiggsGeneration13TeV>,
 1581 last accessed on 16.01.2018.
- 1582 [45] CMS Collaboration, “SM Higgs production cross sections at $\sqrt{s} = 13$ TeV.”
 1583 <https://twiki.cern.ch/twiki/bin/view/LHCPhysics/CERNYellowReportPageAt13TeV>, last
 1584 accessed on 16.01.2018.
- 1585 [46] S. Dawson, The effective W approximation, Nucl. Phys. B 249 (1985) 42.
- 1586 [47] S. Biswas, E. Gabrielli and B. Mele, JHEP 1301 (2013) 088 [[arXiv:1211.0499](https://arxiv.org/abs/1211.0499)
 1587 [hep-ph]].
- 1588 [48] F. Demartin, B. Maier, F. Maltoni, K. Mawatari, and M. Zaro, “tWH associated
 1589 production at the LHC”, European Physical Journal C, vol. 77, p. 34, (2017).
 1590 [arXiv:1607.05862](https://arxiv.org/abs/1607.05862)
- 1591 [49] LHC Higgs Cross Section Working Group, “Handbook of LHC Higgs Cross
 1592 Sections: 4.Deciphering the Nature of the Higgs Sector”, [arXiv:1610.07922](https://arxiv.org/abs/1610.07922).
- 1593 [50] J. Ellis, D. S. Hwang, K. Sakurai, and M. Takeuchi.“Disentangling Higgs-Top
 1594 Couplings in Associated Production”, JHEP 1404 (2014) 004, [[arXiv:1312.5736](https://arxiv.org/abs/1312.5736)].
- 1595 [51] CMS Collaboration, V. Khachatryan et al., “Precise determination of the mass
 1596 of the Higgs boson and tests of compatibility of its couplings with the standard
 1597 model predictions using proton collisions at 7 and 8 TeV,” [arXiv:1412.8662](https://arxiv.org/abs/1412.8662).
- 1598 [52] ATLAS and CMS Collaborations, “Measurements of the Higgs boson produc-
 1599 tion and decay rates and constraints on its couplings from a combined ATLAS

- 1600 and CMS analysis of the LHC pp collision data at $sqrts = 7$ and 8 TeV,” (2016).
 1601 CERN-EP-2016-100, ATLAS-HIGG-2015-07, CMS-HIG-15-002.
- 1602 [53] File:Cern-accelerator-complex.svg. Wikimedia Commons,
 1603 the free media repository. Retrieved January, 2018 from
 1604 <https://commons.wikimedia.org/wiki/File:Cern-accelerator-complex.svg>
- 1605 [54] J.L. Caron , “Layout of the LEP tunnel including future LHC infrastructures.”,
 1606 (Nov, 1993). A C Collection. Legacy of AC. Pictures from 1992 to 2002. Re-
 1607 trieval from <https://cds.cern.ch/record/841542>
- 1608 [55] M. Vretenar, “The radio-frequency quadrupole”. CERN Yellow Report CERN-
 1609 2013-001, pp.207-223 DOI:10.5170/CERN-2013-001.207. arXiv:1303.6762
- 1610 [56] L.Evans. P. Bryant (editors). “LHC Machine”. JINST 3 S08001 (2008).
- 1611 [57] CERN Photographic Service.“Radio-frequency quadrupole, RFQ-1”, March
 1612 1983, CERN-AC-8303511. Retrieved from <https://cds.cern.ch/record/615852>.
- 1613 [58] CERN Photographic Service “Animation of CERN’s accelerator net-
 1614 work”, 14 October 2013. DOI: 10.17181/cds.1610170 Retrieved from
 1615 <https://videos.cern.ch/record/1610170>
- 1616 [59] C.Sutton. “Particle accelerator”.Encyclopedia Britannica. July 17, 2013. Re-
 1617 trieval from <https://www.britannica.com/technology/particle-accelerator>.
- 1618 [60] L.Guiraud. “Installation of LHC cavity in vacuum tank.”. July 27 2000. CERN-
 1619 AC-0007016. Retrieved from <https://cds.cern.ch/record/41567>.
- 1620 [61] J.L. Caron, “Magnetic field induced by the LHC dipole’s superconducting coils”.
 1621 March 1998. AC Collection. Legacy of AC. Pictures from 1992 to 2002. LHC-
 1622 PHO-1998-325. Retrieved from <https://cds.cern.ch/record/841511>

- 1623 [62] AC Team. “Diagram of an LHC dipole magnet”. June 1999. CERN-DI-9906025
1624 retrieved from <https://cds.cern.ch/record/40524>.
- 1625 [63] CMS Collaboration “Public CMS Luminosity Information”.
1626 <https://twiki.cern.ch/twiki/bin/view/CMSPublic/LumiPublicResults#2016>
1627 _proton_proton_13_TeV_collis, last accessed 24.01.2018
- 1628 [64] J.L Caron. “LHC Layout” AC Collection. Legacy of AC. Pictures
1629 from 1992 to 2002. September 1997, LHC-PHO-1997-060. Retrieved from
1630 <https://cds.cern.ch/record/841573>.
- 1631 [65] J.A. Coarasa. “The CMS Online Cluster: Setup, Operation and Maintenance
1632 of an Evolving Cluster”. ISGC 2012, 26 February - 2 March 2012, Academia
1633 Sinica, Taipei, Taiwan.
- 1634 [66] CMS Collaboration. “The CMS experiment at the CERN LHC” JINST 3 S08004
1635 (2008).
- 1636 [67] CMS Collaboration. “CMS detector drawings 2012” CMS-PHO-GEN-2012-002.
1637 Retrieved from <http://cds.cern.ch/record/1433717>.
- 1638 [68] R. Breedon. “View through the CMS detector during the cooldown of the
1639 solenoid on February 2006. CMS Collection”, February 2006, CMS-PHO-
1640 OREACH-2005-004, Retrieved from <https://cds.cern.ch/record/930094>.
- 1641 [69] A. Dominguez et. al. “CMS Technical Design Report for the Pixel Detector
1642 Upgrade”, CERN-LHCC-2012-016. CMS-TDR-11.
- 1643 [70] CMS Collaboration. “Description and performance of track and primary-vertex
1644 reconstruction with the CMS tracker,” Journal of Instrumentation, vol. 9, no.
1645 10, p. P10009,(2014).

- 1646 [71] CMS Collaboration and M. Brice. “Images of the CMS Tracker Inner
1647 Barrel”, November 2008, CMS-PHO-TRACKER-2008-002. Retrieved from
1648 <https://cds.cern.ch/record/1431467>.
- 1649 [72] M. Weber. “The CMS tracker”. 6th international conference on hyperons, charm
1650 and beauty hadrons Chicago, June 28-July 3 2004.
- 1651 [73] CMS Collaboration. “Projected Performance of an Upgraded CMS Detector at
1652 the LHC and HL-LHC: Contribution to the Snowmass Process”. Jul 26, 2013.
1653 arXiv:1307.7135
- 1654 [74] L. Veillet. “End assembly of HB with EB rails and rotation in-
1655 side SX ”,January 2002. CMS-PHO-HCAL-2002-002. Retrieved from
1656 <https://cds.cern.ch/record/42594>.
- 1657 [75] J. Puerta-Pelayo.“First DT+RPC chambers installation round in the
1658 UX5 cavern.”. January 2007, CMS-PHO-OREACH-2007-001. Retrieved from
1659 <https://cds.cern.ch/record/1019185>
- 1660 [76] X. Cid Vidal and R. Cid Manzano. “CMS Global Muon Trigger” web
1661 site: Taking a closer look at LHC. Retrieved from https://www.lhc-closer.es/taking_a_closer_look_at_lhc/0.lhc_trigger
- 1663 [77] WLCG Project Office, “Documents & Reference - Tiers - Structure,” (2014).
1664 <http://wlcg.web.cern.ch/documents-reference> , last accessed on 30.01.2018.
- 1665 [78] A. Buckleya, J. Butterworthb, S. Giesekec, et. al. “General-purpose event gen-
1666 erators for LHC physics”. arXiv:1101.2599v1 [hep-ph] 13 Jan 2011
- 1667 [79] DurhamHep Data Project, “The Durham HepData Project - PDF Plotter.”
1668 <http://hepdata.cedar.ac.uk/pdf/pdf3.html> , last accessed on 02.02.2018.

- 1669 [80] F. Maltoni, G. Ridolfi, and M. Ubiali, “b-initiated processes at the LHC: a
 1670 reappraisal,” Journal of High Energy Physics, vol. 07, p. 022, (2012).
- 1671 [81] CMS Collaboration, “Search for the associated production of a Higgs boson
 1672 with a single top quark in proton-proton collisions at $\sqrt{s} = 8$ TeV”, JHEP 06
 1673 (2016) 177,doi:10.1007/JHEP06(2016)177, arXiv:1509.08159.
- 1674 [82] B. Stieger, C. Jorda Lope et al., “Search for Associated Production of a Single
 1675 Top Quark and a Higgs Boson in Leptonic Channels”, CMS Analysis Note CMS
 1676 AN-14-140, 2014.
- 1677 [83] M. Peruzzi, C. Mueller, B. Stieger et al., “Search for ttH in multilepton final
 1678 states at $\sqrt{s} = 13$ TeV”, CMS Analysis Note CMS AN-16-211, 2016.
- 1679 [84] CMS Collaboration, “Search for H to bbar in association with a single top quark
 1680 as a test of Higgs boson couplings at $\sqrt{s} = 13$ TeV”, CMS Physics Analysis
 1681 Summary CMS-PAS-HIG-16-019, 2016.
- 1682 [85] B. Maier, “SingleTopHiggProduction13TeV”, February, 2016.
 1683 <https://twiki.cern.ch/twiki/bin/viewauth/CMS/SingleTopHiggsGeneration13TeV>.
- 1684 [86] M. Peruzzi, F. Romeo, B. Stieger et al., “Search for ttH in multilepton final1
 1685 states at $\sqrt{s} = 13$ TeV”, CMS Analysis Note CMS AN-17-029, 2017.
- 1686 [87] B. WG, “BtagRecommendation80XReReco”, February, 2017.
 1687 <https://twiki.cern.ch/twiki/bin/view/CMS/BtagRecommendation80XReReco>.